Strain path dependency in sheet metal

Experiments and models

Samenstelling van de promotiecommissie:

voorzitter en secretaris:	
Prof. dr. F. Eising	Universiteit Twente
promotor:	
Prof. dr. ir. J. Huétink	Universiteit Twente
assistent promotor:	
Dr. ir. A.H. van den Boogaard	Universiteit Twente
leden:	
Dr. S. Bouvier	LPMTM-CNRS, Université Paris 13
Dr. ir. W.A.M. Brekelmans	Technische Universiteit Eindhoven
Prof. dr. ir. H.J.H Brouwers	Universiteit Twente / Wuhan University China
Dr.ir. C.H.L.J. ten Horn	Corus Research, Development & Technology
Prof. S. Luding	Universiteit Twente
Prof. dr. rer. nat. B. Svendsen	Technische Universität Dortmund

ISBN 978-90-77172-50-6

1st Printing August 2009

Keywords: plasticity, material models, strain path

This thesis was prepared with LaTeX by the author and printed by Ipskamp Drukkers, Enschede, from an electronic document.

STRAIN PATH DEPENDENCY IN SHEET METAL
EXPERIMENTS AND MODELS

PROEFSCHRIFT

ter verkrijging van
de graad van doctor aan de Universiteit Twente,
op gezag van de rector magnificus,
prof. dr. H. Brinksma,
volgens besluit van het College voor Promoties
in het openbaar te verdedigen
op vrijdag 28 augustus 2009 om 16:45 uur

door

Maarten van Riel

geboren op 5 januari 1978
te Velp

Dit proefschrift is goedgekeurd door de promotor:

Prof. dr. ir. J. Huétink

en de assistent promotor:

Dr. ir. A.H. van den Boogaard

Contents

Summary

Sheet metal forming processes are used to create products that have a high stiffness combined with a small weight. To determine the settings of such a production process, fundamental knowledge of the mechanical behaviour of the metal and of the process itself is required. With the introduction of the finite element software a new opportunity for cost reduction was presented. The finite element method allows for optimisation of forming process with a computer, instead of with a costly trial and error process in the workshop. Amongst the various models that are used in this tool, a material model is used to describe the mechanical behaviour of the sheet. The accuracy of the prediction of the finite element software is determined by the accuracy of its components. In this thesis, the influence of the strain path on the mechanical behaviour is investigated. Experiments are used to improve the material models and to improve the overall predictions of the finite element method.

The mechanical behaviour was tested with the TWENTE BIAXIAL TESTER, a unique test equipment that loads a sheet metal specimen in two directions. Two different challenges occurred with this test equipment: the strain measurement and the stiffness of the test equipment itself. For an accurate determination of the strains in the sample, the measured clamp displacement is not sufficiently accurate. The optical strain measurement was optimised for an accurate strain measurement. The strain path changes, applied to investigate the mechanical behaviour of the sample, also deformed the frame-work of the TWENTE BIAXIAL TESTER. In turn, this affected the test procedure such, that some experiment were not feasible. An algorithm was implemented to control the deformation in the test rig during experiments.

In this research, four materials were investigated. They are: mild steel (DC06), high strength steel (H340LAD), aluminium (AA5182) and a dual phase steel (DP600). The different experiments showed that the conventional DC06 is most sensitive to strain path changes. It showed that upon a load reversal, the flow stress decreases significantly. A loading direction perpendicular to the initial direction introduces a higher flow stress. Additionally, continuously changing strain path changes were applied to mimic a true forming process. The mechanical behaviour observed in the experiments can be explained with the evolution of the dislocation structure. In the literature, mechanisms were observed on the micro-scale that are easily correlated with the mechanical behaviour on the macro-level. A causal effect though, seems hard to prove.

To simplify the implementation of material models, a generic material model was introduced. The scheme used in this model allows for simple implementation of alternative models. Isotropic and kinematic hardening models were initially implemented in this scheme. Furthermore, two strain path dependent models were implemented: the Teodosiu

& Hu model and the Levkovitch model. The latter describes the mechanical behaviour in a phenomenological way. The Teodosiu & Hu model describes the evolution of the dislocation structure from which the mechanical behaviour is deduced. Both models show accurate stress–strain curves, but require more computation time. Additionally, the strain path dependent models can deteriorate the global convergence of a finite element simulation, hereby increasing the calculation time even more. The models were validated by the simulation of a semi-academical deep drawing product.

Using the full strain path dependent material models requires an extensive set of mechanical experiments and experience with fitting procedures to determine the material constants. Hence, using a strain path dependent material model is only desired when the strain path changes experienced in the forming process induces mechanical behaviour that cannot be described with a classical model. To this end, a strain path change indicator was developed that quantifies strain path changes and allows its assessment.

Samenvatting

Plaatomvormingsprocessen worden gebruikt om producten te maken die een hoge stijfheid combineren met een laag gewicht. Om de instellingen van een dergelijke proces te bepalen is fundamentele kennis nodig van het mechanisch gedrag van zowel het plaatmateriaal als het proces zelf. Met de introductie van de eindige elementen software werd er een nieuwe mogelijkheid tot kostenbesparing gepresenteerd. De eindige elementen methode maakt het mogelijk het proces te optimaliseren met de computer in plaats van in de fabriek waar het proces handmatig geoptimaliseerd wordt. Onder de grote verscheidenheid aan modellen die toegepast worden in dit hulpmiddel, wordt het materiaalmodel gebruikt om het mechanisch gedrag van de plaat te beschrijven. De nauwkeurigheid van een voorspelling van de eindige elementen software wordt bepaald door de nauwkeurigheid van zijn componenten. In dit proefschrift wordt de invloed van het rekpad op het mechanisch gedrag bestudeerd. Experimenten zijn uitgevoerd om materiaalmodellen te verbeteren, en om de gehele voorspelling van de eindige elementen methode te verbeteren.

Het mechanisch gedrag is getest met de TWENTSE BIAXIALE BANK, een unieke testbank die een metalen testplaatje kan belasten in twee richtingen. Twee problemen kwamen aan het licht met deze testopstelling: de rekmeting en de stijfheid van de testopstelling zelf. Voor een nauwkeurige bepaling van de rek in het testplaatje is de gemeten klemverplaatsing niet goed genoeg. Hiertoe is de optische rekmeting geoptimaliseerd voor een nauwkeurige rekmeting. De rekpadveranderingen, die zijn toegepast om het mechanisch gedrag van het testplaatje te testen, vervormde ook het frame van de testopstelling. Als gevolg daarvan werd de test zodanig beïnvloed, dat sommige testen niet mogelijk bleken. Een algoritme is geïmplementeerd dat de vervorming van de testopstelling compenseert tijdens experimenten.

In dit onderzoek zijn er vier materialen onderzocht, te weten: vervormingsstaal (DC06), hoge sterkte staal (H340LAD), aluminium (AA182) en twee-fasen staal (DP600). De verschillende experimenten toonden aan dat het conventionele DC06 het meest gevoelig is voor rekpadveranderingen. Na een lastwisseling daalde de vloeispanning significant. Een verandering van het rekpad haaks op de initiële richting resulteerde juist in een hogere vloeispanning. Rekpadveranderingen waarin het rekpad geleidelijk werd veranderd zijn uitgevoerd om het gedrag in een werkelijk omvormproces te simuleren. Het mechanisch gedrag wat gemeten is in de experimenten kan uitgelegd worden met de ontwikkelingen op dislokatie-niveau. Mechanismen die optreden op het microniveau zijn beschreven in de literatuur, en worden gecorreleerd met het mechanisch gedrag op de macroschaal. Een oorzakelijk effect is evenwel moeilijk te bewijzen.

Om de implementatie van de materiaal modellen te vereenvoudigen, is er eerst een ge-

neriek materiaalmodel geïntroduceerd. Het gebruikte schema maakt het mogelijk om eenvoudig alternatieve modellen te implementeren. Isotrope en kinematische verstevigingsmodellen zijn in eerste instantie geïmplementeerd in dit schema. Daarnaast zijn er twee rekpadafhankelijke modellen geïmplementeerd: het Teodosiu & Hu model en het Levkovitch model. De laatst genoemde beschrijft het mechanische gedrag op een fenomenologische manier. Het Teodosiu & Hu model beschrijft de evolutie van de dislokatie-structuur, waaruit vervolgens het mechanisch gedrag afgeleid wordt. Beide modellen geven nauwkeurige spanning–rek-krommes, maar vragen ook meer rekentijd. Bovendien kunnen de rekpadafhankelijke modellen de globale convergentie van een eindige elementen simulaties verstoren, waardoor de rekentijd nog verder toeneemt. De modellen zijn gevalideerd met simulaties van een semi-academisch dieptrekprodukt.

Het gebruik van volledig rekpadafhankelijke materiaalmodellen vraagt om een uitgebreide set van mechanische experimenten, en om ervaring met fit-procedures om de materiaalconstanten te bepalen. Het gebruik van een rekpadafhankelijk materiaalmodel is dus alleen gewenst als er rekpadveranderingen optreden in het omvormproces die mechanisch gedrag veroorzaken wat niet beschreven kan worden met een conventioneel materiaalmodel. Daarom is er een rekpadveranderings-indicator ontwikkeld die de rekpadverandering kwantificeert en daarmee beoordeling mogelijk maakt.

Preface

The results of four years of research is presented in this thesis. It fits into a larger scope on materials research performed in the group of applied mechanics. Already in 1996 it was recognised that strain path changes in material models were not taken into account. The basic concepts of the TWENTE BIAXIAL TESTER were developed by Han Huétink, after which Joop Brinkman started with the actual design. In the following years, the tester was made and the first experiments were performed. Hermen Pijlman based his doctoral thesis on much of the experiments he performed with the TWENTE BIAXIAL TESTER, and at the same time he did a lot of development on the hard- and software. After that, a proposal for another PhD-assignment was prepared together with Corus, to further explore strain path sensitivity in sheet metal with the TWENTE BIAXIAL TESTER and improve the material models with the experimental results. The Netherlands Institute for Metals Research (the current M2i) accepted the proposal and the project was carried out under project number MC1.03158 in the framework of the Strategic Research Program of the Materials Innovation Institute (M2i) in the Netherlands (www.M2i.nl).

Acknowledgements

Although it is often thought that a PhD research is an individual activity, my experience tells me something different. A large number of people helped me, either with the project itself, or by motivating me to finish this project. I would like to acknowledge those people. First of all, I would like to thank Ton van den Boogaard for the opportunity to join the Applied Mechanics group. I enjoyed our discussions, and the way you could just open my eyes and show a solution to whatever problem I had.

The project was embedded in the M2i, former NIMR, and initiated by the researchers from Corus PAC and the University of Twente. I would like to thank all the members of the M2i head quarters for all their help, understanding and support on many organisation issues. The research was carried out at the University of Twente, section of Applied Mechanics. I would like to express my sincere gratitude to prof. Han Huétink for his guidance and enthusiastic support for these years. The meetings with the people from Corus PAC I enjoyed very much. I'm grateful to Carel ten Horn, Henk Vegter, Ruth van de Moesdijk, Eisso Atzema and others for bringing nice discussions and good fun in these meetings!

The work on the DIEKA-software would have been impossible for me if Nico wasn't there to help me with the UNIX machinery that I just couldn't understand. I owe many thanks to Harm Wisseling for his ever patient attitude when something in my code "just didn't work", and his enthusiasm for helping me out numerous times. I enjoyed the time

I spent with Herman van Corbach discussing pencils or computer stuff when working on experiments. Thanks to Debbie van Vrieze-Zimmerman van Woesik and Tanja Gerrits for all administrative issues. Special thanks to Tanja for the nice discussions about work and life in general. Bert Vos, Laura Vargas, Laurant Warnet and René ten Thije made the work in the laboratory a pleasure!

Daily life in our group was brightened by the atmosphere that was created by my colleagues. I enjoyed the breaks with Pawel Owcarek, Bert Koopman, Didem Akçay Perdahcıoğlu, Emre Dikmen, Ashraf Hadoush, Wouter Quak, Bert Geijselaers, Wissam Assaad, Timo Meinders, Srihari Kurikuri and Muhammad Niazi. A special place is reserved for Semih Perdahcıoğlu, with whom I had many discussions about material modelling, cars, bikes and the differences between cultures during our intermediate-sub-coffee breaks. Also the conferences that I joined is something that I won't forget easily; Scotland, Barcelona and Sweden still bring a smile to my face.

Part of the work presented in this thesis was done at the University of Dortmund in the group of prof. Svendsen. The work that I did in co-operation with Muhammad Noman, Clemens Barthel and Bob Svendsen proved to be very useful. Thank you for the nice discussions and good co-operation! It was also a pleasure to host Till Clausmeyer in our group. For helping me out with the million of experiments that I had to do, I want to thank Ranu van Ruth and Marco Razetto. Joop Brinkman is greatly acknowledged for his support on the technical side and the interesting technical discussions.

I would like to acknowledge Han Huétink, Ton van den Boogaard, Timo Meinders and Ashraf Hadoush for carefully reading the manuscript and helping me to improve its contents significantly. Additionally, I would like to thank Katrine Emmett for correcting my thesis with respect to my very personalised English language.

My parents also belong on this list of thank-you's. They supported me when I made the decision to go to the UT, which was at that time a rather drastic, abrupt and not so obvious choice. Thank you for the opportunity to live my life, and to let me be who I am.

The last person to thank is Krista, the most important person in my life. Thank you for supporting me, cheering me up and for making me laugh! You made me the happiest man ever by marrying me!

Maarten van Riel
Ede, August 2009

Nomenclature

Roman symbols

F, G, H, H	anisotropy parameters
R_θ	Lankford R-value, ratio between width and thickness strain
$\mathbf{E}$	elasticity matrix
$\mathbf{F}$	deformation gradient
$\mathbf{L}$	velocity gradient
$\mathbf{D}$	rate of deformation
$\mathbf{W}$	spin tensor
w	work
$\mathbf{K}$	tangential stiffness
$\mathbf{P}$	polarity matrix
$\mathbf{S}$	strength of the dislocation structure matrix
$\mathbf{S}_\mathrm{L}$	latent strength of the dislocation structure matrix
S_D	directional strength of the dislocation structure
h_P	variable in the Teodosiu & Hu model
h_α	variable in the Teodosiu & Hu model
$\mathbf{H}$	distortion matrix
$\mathbf{H}_\mathrm{L}$	latent distortion matrix
H_D	directional distortion
$\mathbf{N}$	normalised direction of plastic flow

$\mathbf{R}$	vector with residuals from the return mapping algorithm

Greek symbols

$\boldsymbol{\alpha}$	back stress vector
α_{s}	saturation value for the back stress
ξ	strain path change indicator
Δ	increment
$\boldsymbol{\varepsilon}$	strain vector
$\varepsilon_{\mathrm{eq}}$	equivalent plastic strain
$\boldsymbol{\zeta}$	effective stress vector
λ	plastic multiplier
μ	friction coefficient
$\boldsymbol{\sigma}$	stress vector
σ_{eq}	equivalent stress
ϕ, φ	yield function

General subscripts and superscripts

$(.)^{\mathrm{e}}$	elastic part
$(.)^{\mathrm{p}}$	plastic part
$(.)_{\mathrm{bi}}$	equi-biaxial
$(.)_{\mathrm{ps}}$	plane strain
$(.)_{\mathrm{sh}}$	shear
$(.)_{\mathrm{un}}$	uniaxial
$(.)_{1,2,3}$	principal values

Operators

$[.]$	components of a tensor in matrix form
$\dot{x}$	material time derivative of x

$\mathbf{a} \cdot \mathbf{b}$	single tensor contraction: $a_i b_i$
$\mathbf{a} \otimes \mathbf{b}$	dyadic product: $a_i b_j$
$\mathbf{A} : \mathbf{B}$	double tensor contraction: $A_{kl} B_{kl}$
$\vert . \vert$	absolute value
$\Vert . \Vert$	Euclidean norm
$(.)^{\mathrm{T}}$	transpose

Abbreviations

BHF	blank holder force
CBB	cell block boundary
LEDS	low energy dislocation sheet
RMA	return mapping algorithm
RD	rolling direction
TD	transverse direction
ND	normal direction

1. Introduction

1.1 Numerical predictions of deep drawing processes

Structures made of sheet metal can combine a high stiffness and a low mass. These properties are exploited in car panels, stiffeners, beer and beverage cans and many other applications. The production of these products from a sheet, by deformation only, is a challenging task. To this end, the process of deep drawing was developed in the last century. The principle is clarified in Figure 1.1. An initially flat piece of sheet metal (the *blank*) is clamped between the *die* and the *blankholder*. As the punch moves downwards, the geometry of the die and punch is transferred to the blank. The blankholder controls the amount of material flowing into the die cavity and hence the amount of strain in the blank. This process proved to be robust, and once in operation, a constant quality of the products is obtained. In general, a high production capacity can also be achieved.

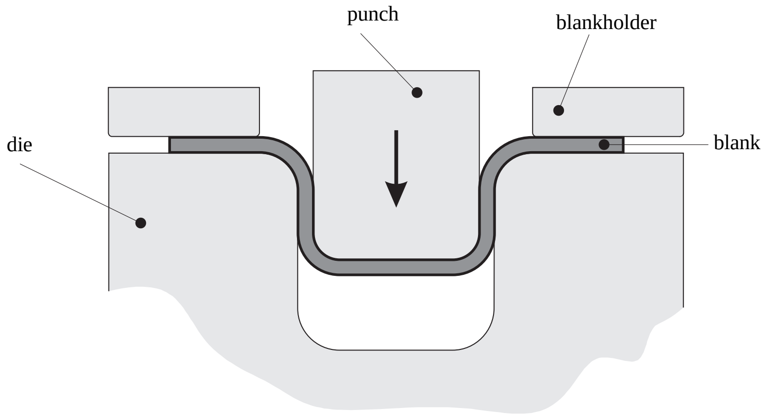

Figure 1.1: The deep drawing of a cup.

Although deep drawing is an efficient production process, it requires experience and knowledge to determine the optimal settings for the process. Wrinkling, springback, necking and complete failure can invalidate the final product. A costly trial and error procedure, in which the process settings are varied, is required to avoid these undesired effects. A significant cost reduction can be made by transferring the trial and error procedure from the workshop to the computer. Simulations of the deep drawing process are hence performed, to *predict* the process characteristics. Tool settings, blank dimensions and other process parameters can be determined without the need to manufacture test tools.

The *Finite Element*-method is used to simulate the deep drawing process and investigate its characteristics. These simulations allow the engineer to investigate the influence of various parameters on the deep drawing process, and also shows how the material deforms as the product is formed. The state variables in the simulation show the evolution of stress and strain, and indicate the features in the actual process that need adjustment. In a FE-code, the actual mechanical behaviour of the blank is described within the material model. Obviously, a material model that describes the mechanical behaviour accurately will lead to better overall predictions of the FE-simulation.

Conventional elastic–plastic material models comprise 2 separate models; the *yield criterion* and the *hardening model*. The yield criterion describes the stress at which the material behaviour changes from elastic to plastic behaviour. They are developed such that they describe the elastic–plastic transition dependent on the loading direction. The hardening models describe the material behaviour when the stress state is in the plastic regime. Here, the deformation is irreversible and in general the stress–strain curve is non-linear. In the elastic regime, it is assumed for metals that the stress–strain relation is linear and reversible. The parameters for the classical yield criteria and hardening models are normally determined using relatively simple tensile tests. However, simple experiments with changing strain paths have shown that the actual behaviour cannot be described sufficiently accurately with these models. The observed strain path sensitivity of sheet metal is the subject of this thesis.

1.2 Strain path sensitivity in metals

In the literature, strain path sensitivity of metals was investigated with 2 characteristic strain path changes: load reversals and orthogonal strain path changes. The influence of a load reversal on the mechanical behaviour of metals has been well investigated (Chaboche, 1991; Christodoulou *et al.*, 1986; Chun *et al.*, 2002; Hasegawa and Yakou, 1975). Most materials show the Bauschinger effect in this strain path change, *i.e.* the stress level in the new stress direction is lower than in the pre-strain phase. In orthogonal strain path changes, 2 monotonic loading paths with perpendicular loading directions are successively applied, (Thuillier and Rauch, 1994; Nesterova *et al.*, 2001). A characteristic sudden increase in stress in the new loading direction was observed in these experiments. It is believed that the non-proportional stress levels after strain path changes stem from the developments on the micro level. The organisation of atoms in the crystal lattice depend on the deformation and the direction of the applied deformation. Different classes of substructures are recognised, depending on the deformation direction. Research in this field is ongoing to deduce the mechanisms that cause the strain path dependent behaviour on the macro scale.

The experiments with an orthogonal strain path change that are presented in the literature show an intermediate elastic unloading prior to loading in the new direction. This is due to the experimental setup used. The obtained stress level in the new direction is higher than for proportional loading. A true deep drawing process, however, will not show a strain path change with unloading. For this reason it is important to investigate the mechanical behaviour for a continuous strain path. Note that this consideration led to a discussion in which it was speculated that a similar strain path without intermediate unloading would induce the same stress peak, (De Montleau, 2004; Wang *et al.*, 2008). The experiments performed in the current thesis add to the conclusion of that discussion.

1.3 Objective of this thesis

An accurate prediction of the stress–strain behaviour enhances the accuracy of the complete simulation of a deep drawing process. The goal of this thesis was to introduce material models that are able to describe the complex mechanical behaviour of sheet metal during strain path changes. Experiments were performed to determine the actual material behaviour, in both continuous and discontinuous strain paths. The material model was to be used in full deep drawing simulations, and hence was required to be sufficiently time efficient.

1.4 Outline

Chapter 2 of this thesis starts with an overview of the basic concepts that are used in material modelling. The commonly used monotonic and non-proportional experiments to investigate the mechanical behaviour are discussed here. It is shown that experiments with a changing, but continuous strain path, are a rarity in this field. Furthermore, different existing theories that describe the influence of the dislocation structure on the macro mechanical behaviour are presented. Concepts of these studies will be used on the macro scale to model the mechanical behaviour. However, it also indicates that continuous strain path changes have not yet been explored.

Chapter 3 concerns an investigation of mechanical behaviour by a biaxial testing device. The TWENTE BIAXIAL TESTER was used to deform a sample in simple shear and plane strain tension. To assess the homogeneity of the deformation area, the sample was investigated with an optical deformation measurement system. Next, the measured deformations were used to define the conditions for a FE-simulation of the experiment. The stress-state across the sample was investigated and the force resultant was compared with the experimentally observed values.

In Chapter 4 the results of the experiments performed on the TWENTE BIAXIAL TESTER are presented. The mechanical behaviour under reversed and orthogonal strain path changes is examined. The results are used for the characterisation of the materials and for the validation of the material models. The materials investigated in this thesis are DC06, AA5182, DP600 and H340. The results demonstrate the need for strain path sensitive models.

Several material models are discussed in Chapter 5. Firstly, a systematic procedure for the evaluation of the stress–strain relation is proposed. Additionally, a method is introduced that allows more elaborate use of yield criteria that are specifically developed for sheet metal forming processes. Full strain path dependent models by Teodosiu and Hu (1995) and Levkovitch and Svendsen (2007) are used to describe the mechanical behaviour observed in the experiments. DC06 is the most challenging material in terms of strain path sensitivity, hence this material is used as a test case. This chapter also contains the description of an indicator that describes how “severe” a strain path changes is. It can be used as a post processing tool to determine the accuracy of the simulation, and indicates whether the simulated process requires a full strain path dependent material model for satisfactory results.

In Chapter 6 the performance of the material models is studied by means of 2 sets of experiments. Tests on the TWENTE BIAXIAL TESTER with combined tension–cyclic shear deformation show the performance of the material models when describing a non-proportional strain path. Secondly, an academic deep drawing product represents an industrial application for the material models. The strain path change indicator is used to demonstrate the strain path changes that are experienced by the material. The material models are assessed for their performance in this setting.

Finally, Chapter 7 summarises the conclusions of this work and the recommendations for future research.

2. Plasticity in sheet metal

In this thesis the mechanical behaviour of sheet metal subjected to strain path changes is investigated. The current material models cannot describe the mechanical behaviour that occurs when a material experiences a strain path change. The aim of this work is to find material models that can accurately describe the effects observed in experiments with strain path changes, and that are sufficiently efficient to be applicable in simulations of true forming simulations. Within the very broad science of metal plasticity this research is only one of the topics. In this chapter the background of the mechanical behaviour and the basic concepts which describe it are presented. Also, different classes of material models are discussed.

The models in macro scale plasticity, Section 2.1, describe some phenomena that are observed with the TWENTE BIAXIAL TESTER in Chapter 3 and these are used in Chapter 4 to show that these classical material models cannot describe all the phenomena observed in experiments with strain path changes. In Section 2.2 dislocation migration and patterning is discussed, which explains in a qualitative way what happens during the strain path changes that are discussed in the literature. Although it does not supply models that can easily be used in engineering applications, it provides an understanding of the underlying mechanisms in experiments with strain path changes.

2.1 Sheet metal characterisation

In this section we discuss the basic concepts that are used in the modelling of plasticity. First the material models that are currently used are introduced. For a more comprehensive overview, the books by Simo and Hughes (2000); Belytschko *et al.* (2006); Zienkiewicz and Taylor (2005) are useful. After that, different experiments are discussed to validate and optimise these models. Finally, the current status from the literature to define and measure strain path dependency is demonstrated.

2.1.1 Elastic–plastic material models

To describe the elastic–plastic mechanical behaviour of metal, classical material models describe the stress–strain behaviour making use of a yield function φ:

$$\varphi = \sigma_{\mathrm{eq}}(\boldsymbol{\sigma}) - \sigma_{\mathrm{f}}(\varepsilon_{\mathrm{eq}}) \tag{2.1}$$

This material model consists of 2 models; the yield surface and the hardening model, σ_{eq} and σ_{f}, respectively. The flow stress σ_{f} describes the measured stress in terms of equivalent

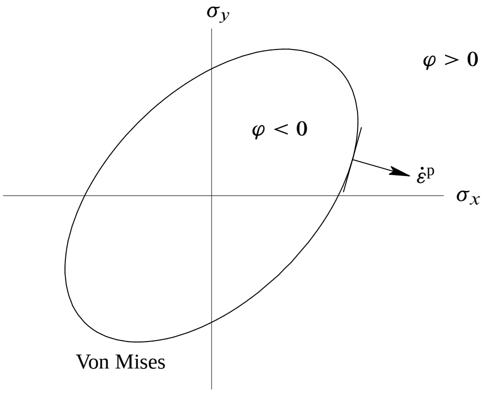

Figure 2.1: The yield criteria by Von Mises in plane stress space without shear.

plastic strain $\varepsilon_{\mathrm{eq}}$. The equivalent stress σ_{eq} determines the shape of the yield surface in stress space and is a function of the full 3-dimensional stress state $\boldsymbol{\sigma}$. Via the equivalent stress it is possible to compare a one-dimensional flow curve with a 3-dimensional stress state. The yield surface only defines the relation between the different stress states upon yielding, not the absolute size of the surface. The size of the yield surface is determined by the hardening model that defines the magnitude of the flow stress. Figure 2.1 illustrates the concept of a yield criterion. The ellipse represents the yield surface according to Von Mises and shows the stress states in plane stress at which yielding occurs. For the situation where $\varphi = 0$ in Equation (2.1), the flow stress σ_{f} and the equivalent stress σ_{eq} are equal. The stress state $\boldsymbol{\sigma}$ is on the yield surface and plastic deformation may occur. If $\varphi < 0$, the equivalent stress is smaller than the current flow stress and the material behaves elastically. Situations where $\varphi > 0$ are not possible in these models. The definition of the yield surface defines the ratio between the stress states at which yielding occurs, but does not state which stress state corresponds with the flow stress. In this work, the yield function is defined such that a uniaxial stress state is equal to the equivalent stress: $\sigma_x = \sigma_{\mathrm{eq}}(\sigma_x) = \sigma_{\mathrm{f}}$.

The equivalent plastic strain is defined according to the yield function. It is assumed that the equivalent plastic strain rate ($\dot{\varepsilon}_{\mathrm{eq}}$) and the equivalent stress are energetically conjugated. This is elaborated in terms of the rate of plastic work $\dot{w}^{\mathrm{p}}$:

$$\dot{w}^{\mathrm{p}} = \sigma_{\mathrm{eq}}\dot{\varepsilon}_{\mathrm{eq}} = \boldsymbol{\sigma} : \dot{\boldsymbol{\varepsilon}}^{\mathrm{p}} \tag{2.2}$$

in which $\dot{\boldsymbol{\varepsilon}}^{\mathrm{p}}$ represents the plastic strain rate. From this equation, the equivalent plastic strain rate is calculated:

$$\dot{\varepsilon}_{\mathrm{eq}} = \frac{\boldsymbol{\sigma} : \dot{\boldsymbol{\varepsilon}}^{\mathrm{p}}}{\sigma_{\mathrm{eq}}} \tag{2.3}$$

To describe the relation between the strain and the stress state, the model discriminates between elastic and plastic deformation. For the elastic deformation the generalised Hooke's law is used:

$$\dot{\boldsymbol{\sigma}} = \mathbf{E} : \dot{\boldsymbol{\varepsilon}}^{\mathrm{e}} \tag{2.4}$$

where $\boldsymbol{\varepsilon}^{\mathrm{e}}$ is the elastic strain tensor and $\mathbf{E}$ is a fourth order tensor with elastic properties. Plastic material behaviour is described by means of Drucker's postulate, which states that the rate of plastic strain is perpendicular to the yield surface:

$$\dot{\boldsymbol{\varepsilon}}^{\mathrm{p}} = \dot{\lambda}\frac{\partial \sigma_{\mathrm{eq}}}{\partial \boldsymbol{\sigma}} \tag{2.5}$$

where $\dot{\lambda}$ is the plastic multiplier.

The model in Equation (2.1) includes the isotropic hardening of the material, *i.e.* the shape of the yield surface is determined by the definition of the equivalent stress and the size of the yield surface is determined by the flow stress. This is shown in Figure 2.2 where the initial yield surface (a) evolves to yield surface (b). To describe the Bauschinger effect in a cyclic test, kinematic hardening is commonly used. This model describes hardening by the movement of the yield surface within stress space. The translation of the yield surface is indicated with the back stress tensor $\boldsymbol{\alpha}$. The definition of the yield criterion now reads:

$$\varphi = \sigma_{\mathrm{eq}}(\boldsymbol{\sigma} - \boldsymbol{\alpha}) - \sigma_{\mathrm{f}}(\varepsilon_{\mathrm{eq}}) \tag{2.6}$$

where the term $(\boldsymbol{\sigma} - \boldsymbol{\alpha})$ is equivalent to the effective stress $\boldsymbol{\zeta}$. The back stress evolves in the direction of the plastic strain rate (Prager) or in the direction of the stress (Ziegler). This model is indicated by yield surface (c). Distortional hardening (yield surface (d)) describes the change of the shape of the yield surface as a function of the plastic strain and the direction of plastic flow or the direction of the stress rate.

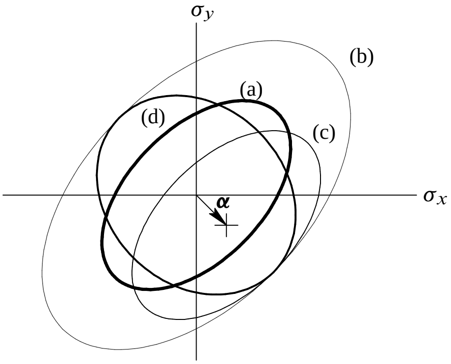

Figure 2.2: The different hardening models demonstrated by pure shear deformation.

2.1.2 Experiments

The traditional test to determine the material behaviour of sheet metals is the uniaxial tensile test. Figure 2.3 shows the sample and how it is oriented with respect to the original sheet. The sample coordinates are indicated with x, y and z. The Rolling Direction (RD), the Transverse Direction (TD) and the Normal Direction (ND) are used to indicate the

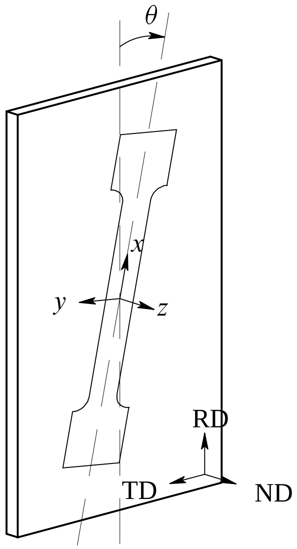

Figure 2.3: A sample used in uniaxial tests for sheet material.

directions used in the fabrication of the sheet. The angle of the sample orientation with respect to the rolling direction is indicated by the angle θ. Due to the rolling process a texture develops in the material. This texture is symmetric in the transverse, normal and rolling directions. The mechanical behaviour of most sheet metals is dependent on the loading direction with respect to the texture orientation. This is captured in the so called R_θ-value:

$$R_\theta = \frac{\varepsilon_y}{\varepsilon_z} \tag{2.7}$$

where ε_y and ε_y denote the transverse and thickness strain respectively. If $R_\theta = 1$ for all values of θ, the material behaves isotropically, but if $R > 1$ or $R < 1$ the material behaves anisotropically. If R is dependent on the angle θ, the material is planar anisotropic. For a material with $R > 1$, the material has a relatively high resistance to thinning.

Traditionally, the uniaxial tensile test is used to benchmark the hardening behaviour of a material. This experiment alone suffices to fit an elastic–plastic material model with the Von Mises yield surface. To describe the yielding behaviour more accurately, new yield surfaces were introduced. The Hill’48 yield surface requires the R-values in 3 different directions: $0°$, $45°$ and $90°$. With time, more experiments were introduced to describe the mechanical behaviour more accurately. Figure 2.4 shows different experiments on sheet metal to investigate the mechanical behaviour under different stress states. These experiments are discussed briefly as follows.

The *pure shear* point is defined as the stress state where the tensile and transverse stresses are equal in magnitude, but opposite in sign. Due to the complexity of such a test, the loading conditions are changed such that the same stress state exists, but the feasibility of the test increases; this is indicated in Figure 2.5. Effectively, the sample is rotated by

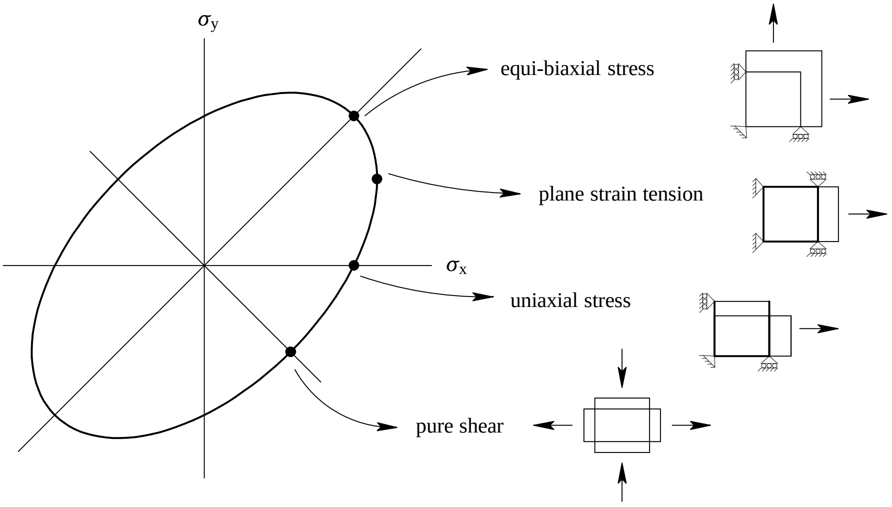

Figure 2.4: Different experiments to measure the stress–strain behaviour for various stress states.

45 ° and in stead of compressive and tensile stresses, *simple shear* deformation is applied. The plane strain tensile test is defined as a tensile test without transverse contraction. The stress state in this test is obtained by preparing a sample with a large width compared to its height. At the edges uniaxial tensile deformation will occur, but if the width to height ratio is large enough, the largest part of the sample will be in plane strain tension (An *et al.*, 2004). Finally, the equi-biaxial test stretches a square specimen in 2 perpendicular directions. This experiment is mostly performed with a cruciform specimen (Kuwabara *et al.*, 2002).

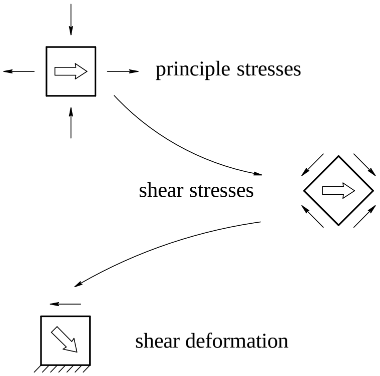

Figure 2.5: Pure shear converted to simple shear for isotropic behaviour.

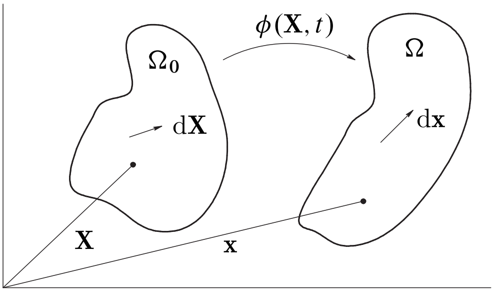

Figure 2.6: The deformation of a body.

Measuring deformation and stresses

In the uniaxial tensile test the strains and stresses are determined easily, but this aspect of material characterisation is more complex than in other experiments. To this end, some definitions of continuum mechanics are used to allow for the determination of strains and stresses.

To characterise the deformation of a body, we refer to Figure 2.6. The domain of the body in the initial state is indicated by Ω_0. Within that domain any arbitrary infinitesimal vector $\mathrm{d}\mathbf{x}$ can be defined. Upon loading of the body, it is deformed to its current domain Ω. The function ϕ maps the initial configuration to the current configuration:

$$\mathbf{x} = \phi(\mathbf{X}, t) \tag{2.8}$$

The *deformation gradient* is the derivative of the mapping with respect to the current material points:

$$\mathbf{F} = \frac{\partial \phi(\mathbf{X}, t)}{\partial \mathbf{X}} \tag{2.9}$$

An infinitesimal vector $\mathrm{d}\mathbf{X}$ in the initial domain is mapped to the current domain, to $\mathrm{d}\mathbf{x}$. The relation between the 2 segments is captured in the deformation gradient:

$$\mathrm{d}\mathbf{x} = \mathbf{F}\,\mathrm{d}\mathbf{X} \tag{2.10}$$

Next, the *velocity gradient* $\mathbf{L}$ indicates the relative velocity and rotation and is defined as:

$$\mathbf{L} = \dot{\mathbf{F}} \cdot \mathbf{F}^{-1} \tag{2.11}$$

The velocity gradient can be decomposed into a symmetric part $\mathbf{D}$ and a skew-symmetric part $\mathbf{W}$:

$$\mathbf{L} = \mathbf{D} + \mathbf{W} \tag{2.12}$$

In elastic–plastic analysis of metals, the rate of deformation is commonly decomposed into an elastic and plastic part:

$$\mathbf{D} = \mathbf{D}^{\mathrm{e}} + \mathbf{D}^{\mathrm{p}} \tag{2.13}$$

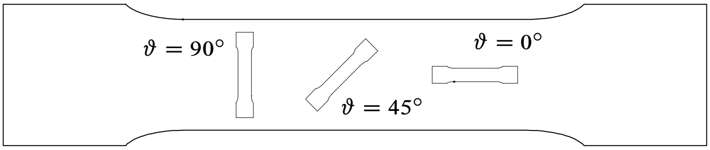

Figure 2.7: Different 2 stage strain path changes.

From the rate of deformation the logarithmic strain increment can be determined:

$$\mathbf{D}\Delta t \approx \boldsymbol{\varepsilon} \tag{2.14}$$

This holds for small time steps and for proportional loading. Furthermore, in metals plasticity it is assumed that a plastic volume change is not possible. Hence,

$$\mathrm{tr}(\mathbf{D}^{\mathrm{p}}) = 0 \tag{2.15}$$

Engineering stress is defined as the ratio of the tensile force over the initial cross section. It is common practice in metals plasticity to use *true stresses* or *Cauchy stresses*, *i.e.* the force divided by the current cross section.

2.1.3 Strain path changes

The experiments on strain path changes that have been reported so far in the literature mostly apply two-stage strain path changes (Fernandes *et al.*, 1993; Rauch and Schmitt, 1989; Gardey *et al.*, 2005; Tarigopula *et al.*, 2008). This is done by applying a deformation to a large sample, after which a smaller sample is removed, at an angle ϑ, see Figure 2.7. This smaller sample is now also tested. An indication for the strain path change between the first and the second loading stage is given by Schmitt *et al.* (1985) as follows:

$$\cos\theta = \frac{\boldsymbol{\varepsilon}_1 \cdot \boldsymbol{\varepsilon}_2}{\|\boldsymbol{\varepsilon}_1\| \, \|\boldsymbol{\varepsilon}_2\|} \tag{2.16}$$

The range of the indicator is $[-1, 1]$, with $\theta = -1$ indicating reverse loading, $\theta = 1$ monotonic loading and $\theta = 0$ orthogonal loading. It is observed that ϑ and θ are not necessarily equal. For example, if $\vartheta = 90°$, the strain path change $\theta = 138°$.

The material models and experiments so far do not fully describe strain path dependent material behaviour. Isotropic hardening describes the mechanical behaviour as a function of accumulated strain and not as a function of the direction of plastic flow. If a material is modelled with kinematic hardening, the Bauschinger effect is included, but the mechanical behaviour during orthogonal strain path changes cannot be described by these models. Gradual strain path changes as observed in a real deep drawing process are not applied and thus need to be explored for further improvement of material models and understanding.

2.2 Dislocation structure evolution

In this section the micro-mechanical behaviour and its influence on the flow stress is discussed. Firstly, the evolution of the dislocation structure under monotonic loading is intro-

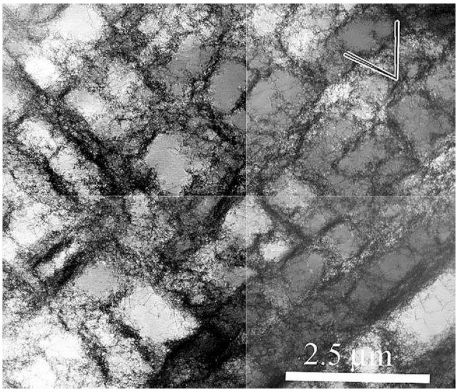

Figure 2.8: Cell block structure of a copper specimen having undergone 7.5 % rolling reduction. The rolling direction corresponds to the horizontal direction (McCabe *et al.*, 2004).

duced. After this a section is devoted to the mechanisms that cause the Bauschinger effect, which is followed by a section on the formation of microbands that typically evolve under orthogonal strain path changes. The phenomena observed at this level are the causes of the strain path sensitive behaviour.

The evolution of the dislocation structure in metals has been much investigated, which is reflected in the number of papers in this field. The materials investigated in the field of strain path dependency are steels, copper and aluminium. Because copper and mild steel show similar behaviour under strain path changes, references to these studies are also included. Finally, it is observed that the designation of phenomena can vary from author to author.

2.2.1 Monotonic loading

In an undeformed metal the dislocations are randomly distributed. During elastic deformation, the crystal lattice is stretched as a whole, and the dislocations move in random directions. Plastic deformation takes place when dislocations migrate simultaneously in a preferred direction.

The dislocations start interacting and form tangles, and so create regions with relatively high and low dislocation densities. Eventually, the highly densed areas link together to form a cellular structure in which volumes with a low dislocation density, the cells, are enclosed. The areas with a high dislocation density are the cell walls. An example of this cell forming for copper is depicted in Figure 2.8. Typically, these cells appear after 3 % strain and are completely developed after 10 % strain. This evolution was found by different authors and for different metals.

As deformation continues, the size of the dislocation cells decreases rapidly, but at a decreasing rate. Besides that, the dislocations vanish from the cell interiors, and migrate to the cell walls. In turn, the cell walls increase in thickness and collapse to cell boundaries. With higher strains ($\varepsilon > 1$) the cell size does not increase any further even though the ma-

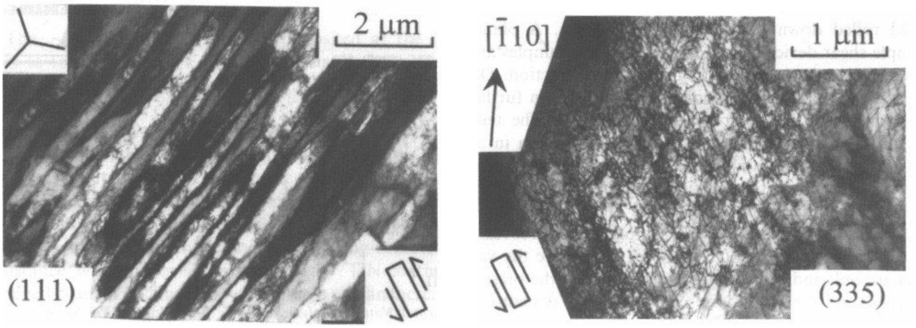

(a) Developed structure at room temperature.

(b) Developed structure at lowered temperature (125K).

Figure 2.9: The dislocation distribution in a mild steel after 35 % of shear deformation (Rauch, 1997).

terial is progressively deformed (Sevillano *et al.*, 1981). For lower strains it was observed that with decreasing cell size r, the flow stress increases. A much used empirical relation for this phenomenon is:

$$\sigma_{\mathrm{f}} = \frac{CGb}{\sqrt{r}} \tag{2.17}$$

where G is the shear modulus, b the Burgers vector and C a material constant. This equation is referred to as the Hall–Petch relation, and is also known as the principle of similitude. This equation describes in a phenomenological way the relation between the dislocation cell size and the flow stress. Although the Hall–Petch relation was confirmed, it is noted that a decreasing cell size is not necessarily the cause of the increased flow stress.

To investigate the influence of the dislocation structure on the flow stress, experiments were carried out by Johnson *et al.* (1990). Mild steel was investigated by tensile tests at cryogenic and room temperatures up to a strain of 10 %. The experiments performed at room temperature showed the cellular structure, whereas the experiments at cryogenic temperatures did not show any patterning. The experiments at lower temperature show a significant increase in flow stress; the yield stress for the experiment at room temperature was approximately 150 MPa and for the test at 201 K a yield stress of 280 MPa was measured. The hardening curves were comparable, but the hardening rate of the test at room temperature was slightly higher. Subsequently, the samples that were pre-strained at cryogenic temperatures were loaded further at room temperature. The resulting flow curve now almost coincided with the material pre-strained at room temperature. In the second loading phase, the yield stress of the samples pre-strained at room temperature and at 201 K have a yield stress of 315 MPa and the hardening curves are similar. Additionally, experiments were performed with a lower temperature in the second stage. It was found that the temperature in the first stage does not influence the resulting flow curves at lower temperatures. Similar results were found by Rauch (1997). Indeed, deformations at lower temperatures led to a homogeneous distribution of dislocations whereas the test at room temperature showed a clear cellular structure, see Figure 2.9. Both authors concluded that there is a

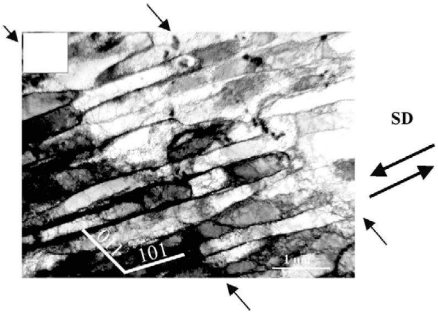

Figure 2.10: A cellular structure obtained by shearing a specimen of a low-carbon IF-steel. The arrows indicate cell block boundaries (Peeters *et al.*, 2001a).

minor effect of the dislocation structure on the flow stress. It was found that the dislocation density, not the structure, dictated the flow stress.

With increasing deformation, the cells of the cellular structure become smaller and the walls become relatively thicker. At some point aligned cell walls are connected to form a *Cell Block Boundary*, see Figure 2.10. They form in turn a larger structure than the initial cellular structure, and enclose multiple cells of this lower level cellular structure. The CBB's are characterised by a higher misorientation compared to the surrounding material; compared to the orientation of the external deformation, they are aligned with the highly stressed slip planes. Kuhlmann-Wilsdorf (1989) explains in a quantitative way how CBB's evolve with deformation. Due to their findings, the name of *Low Energy Dislocation Sheets* or *LEDS* was introduced[1].

Lewandowska (2003) investigated the aluminium alloys AA5182 in simple shear deformation and found that the evolution of this structure depended on the orientation of the individual grains. A homogeneous distribution of dislocations was observed with the grains having a $\langle 1\,0\,0 \rangle$ direction parallel to the normal direction of the sheet, see Figure 2.11(a). When the grains are oriented with the $\langle 1\;1\;2 \rangle$ direction normal to the sheet, a well defined structure with dislocation walls along the $\{1\;1\;1\}$ slip planes evolve, see Figure 2.11(b). In Figure 2.11(b) the orientation of the dislocation sheets is parallel and perpendicular to the shearing direction.

In Thuillier and Rauch (1994) the dislocation structure of mild steel under monotonic deformation is discussed. A similar structure exists as observed in copper (McCabe *et al.*, 2004), the cellular structure is roughly parallel with the shear direction. Also, cell block boundaries perpendicular to the shear direction are formed. In a tensile test, the same structure exists, but the dislocation sheets are formed inclined to the tensile direction ($45° \pm 15°$) and correspond to an active slip system. The shape of the structure however remains rectangular.

Although LEDS are considered to contribute to the work hardening, there is no decisive proof of that so far. The relation between the dislocation structure and the flow stress is

---

[1] In the literature, different terms have been used for the cellular structures including *cell boundaries*, *geometrically necessary dislocation boundaries* (GNBs) and *carpet structures*.

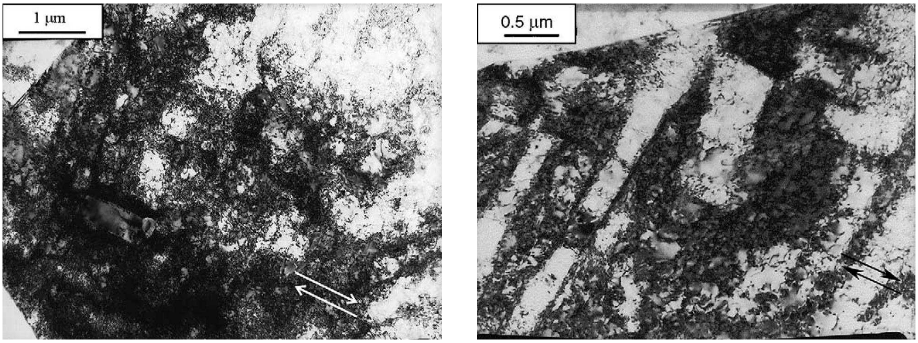

(a) A nearly uniform distribution of the dislocations.

(b) Two sets of dislocation walls formed during deformation.

Figure 2.11: The dislocation distribution of the dislocations in a AA5182 alloy after 30% of shear deformation (Lewandowska, 2003).

consistent, but it seems not to be causal.

2.2.2 Bauschinger effect

The Bauschinger effect describes the decreased flow stress after a load reversal. In this research such strain path changes are important to consider because they take place in bending–unbending of the sheet in deep drawing processes. To examine this behaviour, experiments with simple shear in forward and reverse directions are used to mimic the load reversal, but also tension–compression tests are performed to investigate the phenomena. Most metals show the Bauschinger effect. Different ideas on the cause of this phenomenon have been developed and are discussed here.

With deformation in the same direction, the dislocations migrate towards the cell walls, and pile-ups of dislocation evolve. These hamper further deformation and increase the work hardening rate. In general, it is assumed that a load reversal releases the stuck dislocations from their positions and because their displacement is reversed, they migrate towards the dislocation free cell interior. Only small stresses are required to translate the dislocations through this area, explaining the Bauschinger effect.

Mughrabi (1983) found that long-range internal stresses prevail in crystals with dislocation walls. So called “interface dislocations” occur between the highly stressed walls of the cellular structure and the low stressed internal region inside the cells. With increasing monotonic deformation, more interface dislocations appear, causing long-range internal stresses. Upon load reversal, the long-range internal stresses are released and contribute to the Bauschinger effect. In the same paper, (Mughrabi, 1983), a composite model was presented to describe the stresses in the cell walls and the inner regions of the cells. Good results have been achieved and some updated models have been developed to describe the macro mechanical behaviour in this way (Goerdeler and Gottstein, 2001).

The micro-structural developments observed in tension–compression tests consist mainly of disruption of the cell walls. From observations with TEM it was concluded that the dislocation wall thickness is not reduced, but the wall breaks apart. It is also mentioned that dislocations move to the cell interior, hereby decreasing the density of the dislocations in the wall (Hasegawa and Yakou, 1975) and hence creating the apparent disruption of cells. This phenomenon can be used to model cyclic behaviour (Christodoulou *et al.*, 1986; Viatkina, 2005).

Rauch (1997) investigated the influence of dislocation structure on the flow stress in reverse tests. Samples with a cellular structure were prepared by deformation at room temperature and samples with a homogeneous dislocation distribution were obtained by predeformation at 177 K. The material with the pre-straining at cryogenic temperature showed a flow stress that was 10 % lower than the material pre-strained at room temperature. From this it was concluded that it is the concentration of dislocations that drives the Bauschinger effect, and not the cellular structure.

2.2.3 Microbands

Upon orthogonal strain path changes microbands[2] are observed in the dislocation structure. Microbands consist of longitudinal cells with very sharp plate-like walls. The thickness of these cells is 0.2-0.4 μm and cross the initial cellular structure. The spacing between the microbands is 4 μm. They were found mostly in copper and mild steel (Ananthan *et al.*, 1991; Rauch and Thuillier, 1993; Thuillier and Rauch, 1994)

The microbands have a low dislocation density in the cells, enhancing the deformation within the microbands. This is illustrated in Figure 2.12. The TEM image in Figure 2.12(a) shows the dislocation structure in a sample that is uniaxially pre-strained, after which simple shear is applied perpendicular to the uniaxial direction. This graph shows clearly that the shear deformation is localised in the microbands. In Figure 2.12(b) the localised shear deformation is schematically illustrated. The initial structure is not deformed, only the microbands are sheared. About 80 % of the shear deformation is absorbed in the microbands.

The microbands are formed at the onset of the shear deformation and are clearly visible after 4 % shear deformation, Figure 2.13. This graph illustrates the dimensions of the microbands and besides shows that the microbands appear and disappear along their length. The microbands develop with respect to the macroscopic loading orientation.

Microbands have only been observed in aluminium by Lewandowska (2003) in AA6016. However, the observations made in this paper were made after 20 % of shear deformation and whereas mild steel shows clear kinks after such deformations (Figure 2.12), the microbands found in AA6016 do not seem to accommodate any localised shear.

It is assumed by many authors that the evolution and degradation of microbands are the key mechanisms that activate the cross-hardening effect in orthogonal tests. For the microbands to evolve a relatively high stress is required, but once in existence, a lower stress is required because of the relatively dislocation free area within their cells. This phenomenon is used by some authors as a basis for models that include strain path dependent behaviour (Peeters *et al.*, 2001b,a; Teodosiu and Hu, 1995).

---

[2] “Microband” is a name that is often used in the literature to indicate long and relatively narrow cells. Sevillano *et al.* (1981) observed them in monotonically deformed copper. This was confirmed by Ananthan *et al.* (1991), but they call the microbands observed after a strain path change second generation microbands (MB2).

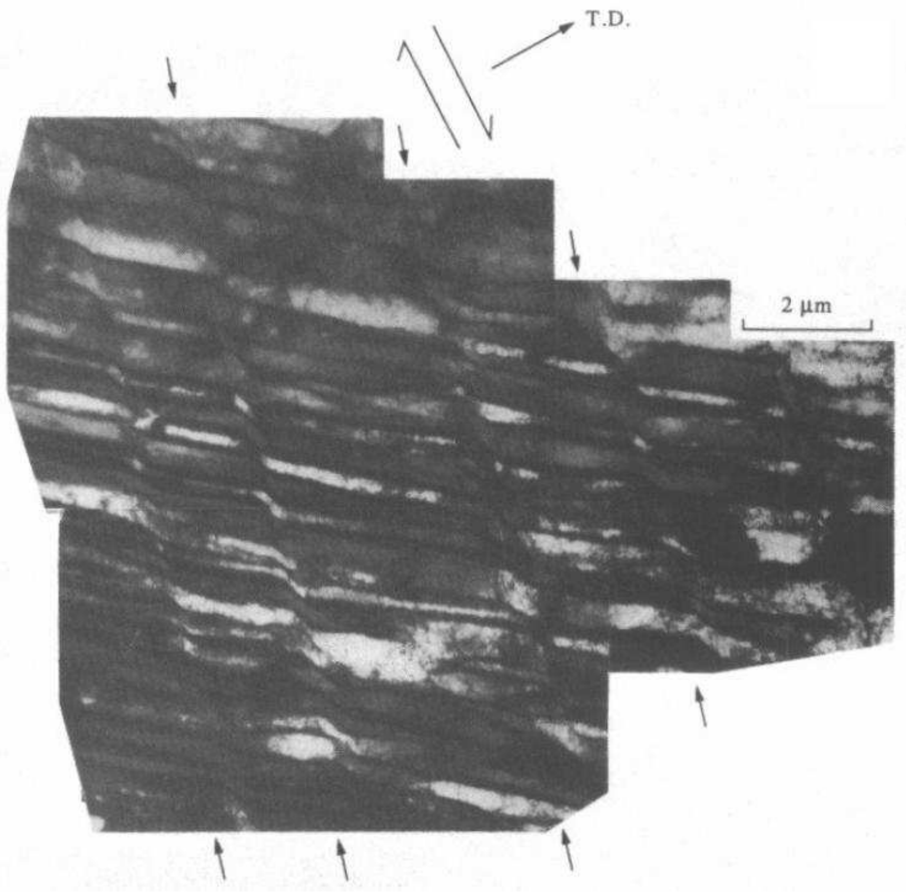

(a) Microbands (indicated by arrows) in mild steel (Thuillier and Rauch, 1994).

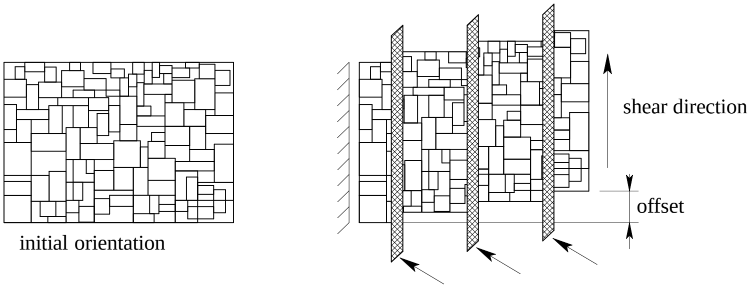

(b) A schematic representation of the offsets in the material induced by the microbands. The arrows indicate microbands.

Figure 2.12: Illustration of microbands in the dislocation structure after 20 % pre-strain in tensile direction (T.D.), followed by 12 % shear deformation.

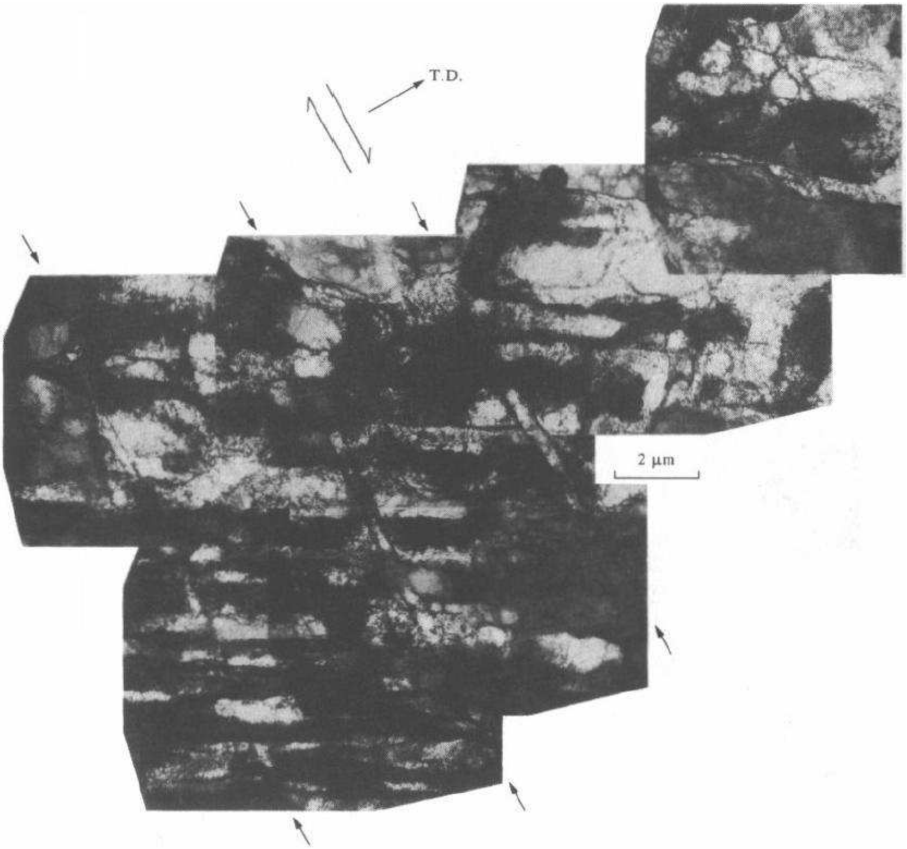

Figure 2.13: Microbands (indicated by arrows) in mild steel, 25 % pre-strain in the tensile direction (T.D.), followed by simple shear, $\gamma = 4$ % (Thuillier and Rauch, 1994).

2.3 Conclusion

This chapter illustrates some of the basic concepts in the modelling of plasticity. The “classical” material models describe the hardening behaviour independent of the strain path. To describe a load reversal, the concept of kinematic hardening is introduced. However, full strain path dependent material models are still “exotic”.

The dislocation structure that evolves during plastic deformation has been investigated to find the relation between the mechanical behaviour and the cellular structures that are present in the material. In the literature the relation between the mechanical behaviour and the structures that evolve on micro-scale are described, but there appears to be no decisive evidence that the dislocation structure is the driving force behind the mechanical behaviour. Experiments with two-stage orthogonal strain path changes have been investigated, but the experiments with a continuous strain path change have not been investigated so far. The continuous or fluent strain path changes, as they are applied in a deep drawing process, are not represented by the strain path dependent experiments in the literature. They are all sharp with elastic unloading between the deformation modes. To this end, the TWENTE BIAXIAL TESTER, which can prescribe such strain paths is introduced in Chapter 3. The experiments performed with this testing device are then considered in Chapter 4.

3. The Twente biaxial tester

The sensitivity of the mechanical behaviour of sheet metal with respect to strain path changes is investigated in this work with the TWENTE BIAXIAL TESTER. This testing device can load a specimen in both the tensile and shear directions. Both loading directions are individually controlled and are used in this work to apply strain path changes to the material.

In this chapter the TWENTE BIAXIAL TESTER is presented and the procedure to determine stress–strain curves is discussed. The strains are measured from the surface with a digital camera and the stresses are determined via the force-sensors. The homogeneity of the deformation area is assessed with advanced digital image correlation software that measures the deformations locally. The stresses are validated with a FE calculation of the deformation area. This chapter also shows that the deformation of the test equipment itself is important in the control of the strain path. A simple algorithm is presented that allows for the compensation of the elastic deformation of the test equipment.

3.1 Goal of the test equipment

Classically, uniaxial tensile tests are used to determine a hardening curve and fit the yield locus parameters. This is sufficient to simulate a sheet metal forming process. However, in sheet metal forming processes the stress state will be changing and will not always coincide with the uniaxial stress state. Furthermore, the strain paths that occur in a sheet metal forming process are not monotonic and mostly non-proportional, hence the uniaxial tensile test cannot fully represent the loading situations that occur in a true forming process.

To investigate the mechanical behaviour of sheet metal while undergoing strain path changes, a more advanced experiment than the uniaxial tensile test is required. At the University of Twente a biaxial testing device was developed that loads a specimen of sheet metal in tension and shear (Pijlman, 2001). The truly exceptional advantage of the TWENTE BIAXIAL TESTER is that continuous strain path changes can be applied while still measuring the stresses. This is a big leap forward compared to the traditional uniaxial tensile tester. Monotonic hardening curves in shear or tension can also still be measured. Finally, the mechanical behaviour under cyclic loading can be measured by the application of reversed simple shear to the sample. Hence, the TWENTE BIAXIAL TESTER supplies many different mechanical experiments in one machine. The goal of the tester is to measure the hardening behaviour of the material. The elastic properties and the accurate measurement of the elastic–plastic transition of sheet metal is not of crucial importance in the test equipment.

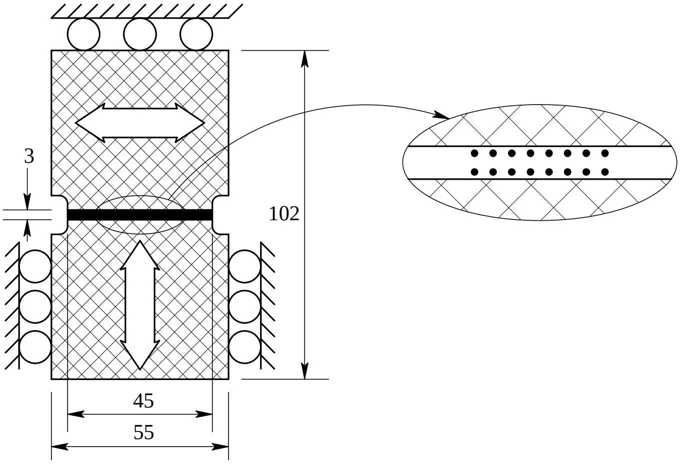

Figure 3.1: The shape and dimensions of the sample in mm. The black and cross-hatched area represent the deformation area and the clamped area, respectively. The zoom shows the dots that are used to measure the deformation.

The TWENTE BIAXIAL TESTER was developed to perform experiments with strain path changes to *i*) investigate the mechanical behaviour and understand mechanisms on a micro-structural level, and *ii*) to develop and fit material models to the measured stress–strain curves.

3.2 Working principles

The specimen dimensions used in the biaxial tester are depicted in Figure 3.1. The thickness of the samples is between 0.7 mm and 2.5 mm. The lower and upper parts of the sample are clamped in the machine, leaving a deformation region of 45×3 mm. The height of the deformation area is small with respect to the thickness in order to apply simple shear without the material buckling. Also, in order to have a large area of homogeneous deformation, the width of the deformation area is large. This imposes a plane strain condition in the transverse direction of the material in the central region of the deformation area. Towards the edges of the deformation area the deformation state will tend to the uniaxial stress state.

The biaxial tester is based on a traditional tensile tester, see Figure 3.2(a). Between the 2 cross bars an additional framework is mounted that accommodates the actuator for the shear deformation. By using a construction of bearings in both the horizontal and vertical directions it is possible to translate the clamps arbitrarily in the horizontal and vertical directions, hereby applying simple shear or tension, respectively. Both actuators are equipped with force sensors to determine the stresses. The deformation is determined from the positions of black dots that are applied to the surface of the specimen and which are in turn tracked by a digital camera.

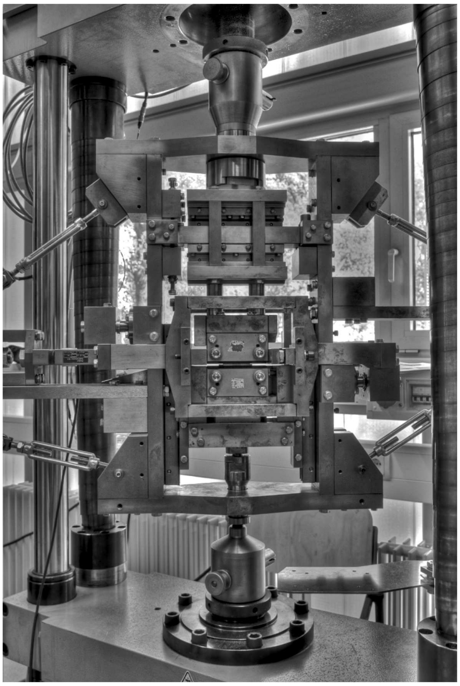

(a) Picture of the experimental setup.

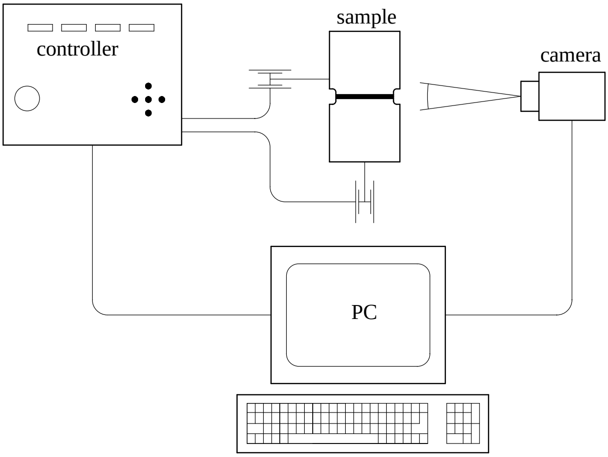

(b) Schematic of the biaxial test setup.

Figure 3.2: The biaxial test equipment.

3.2.1 Test procedure

The test procedure for an experiment starts with writing an input file for the controller, Figure 3.2(b). This file contains the description for the movement of the actuators. This can be done explicitly, but also functions can be programmed based on input from *e.g.* the force sensors. After the dots are applied to the sample, the specimen is mounted in the machine. Next, the camera is positioned and is focussed with the aid of a LABVIEW application installed on the PC. Via this application the test is started and all the data is logged: time, position of the dots, force-signals and the actuator displacement. Depending on the camera's view, up to 40 data sets per second can be stored. A typical experiment takes 50 minutes, where 30 min is spent on the mounting and disassembly of the sample; 8 min on sample preparation, and 12 min on camera positioning and performing the experiment. The actual experiment in which the deformation is applied takes 1 to 10 min.

3.3 Strain measurement

The deformation of the sample is reflected in the change of the coordinates of the dots as represented in Figure 3.3. To determine the strain, the **F**-tensor must be determined that maps the reference configuration Ω_0 to the current configuration Ω_t. Assuming a homogeneous deformation field, Equation (2.10) is evaluated with $\mathrm{d}\mathbf{x} \to \Delta\mathbf{x}$:

$$\Delta\mathbf{x} = \mathbf{F}\Delta\mathbf{X} \tag{3.1}$$

The vectors $\Delta\mathbf{x}$ and $\Delta\mathbf{X}$ represent the lines between the dots in the initial configuration and the configuration at time t. In the case of deformation in 2D, in the plane only, 3 dots are required to fully determine the strain field. From these dots only 2 vectors are needed to determine the components of **F**. In matrix-vector format this reads:

$$\begin{Bmatrix} \Delta x_1 \\ \Delta y_1 \\ \Delta x_2 \\ \Delta y_2 \end{Bmatrix} = \begin{bmatrix} F_{11} & F_{12} & 0 & 0 \\ F_{21} & F_{22} & 0 & 0 \\ 0 & 0 & F_{11} & F_{12} \\ 0 & 0 & F_{21} & F_{22} \end{bmatrix} \begin{Bmatrix} \Delta X_1 \\ \Delta Y_1 \\ \Delta X_2 \\ \Delta Y_2 \end{Bmatrix} \tag{3.2}$$

This system of equations is fully determined, and the application of more dots will result in an over-determined system. From a theoretical point of view, more dots do not contribute to a better description of **F**. In the experimental setup, however, noise is measured at the positions of the dots, and this affects the determination of **F**. To this end, more dots are

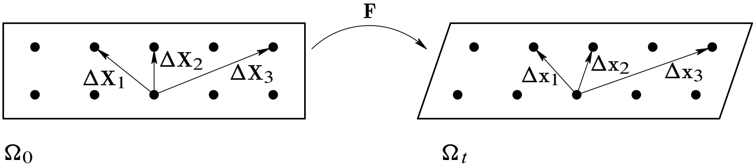

Figure 3.3: The displacement of the dots indicates the deformation.

applied, such that the effect of the noise in the measurement is reduced. In the absence of noise and for a homogeneous deformation field, more vectors can be used such that the following holds:

$$\left\{\begin{matrix}\Delta x_1\\ \Delta y_1\\ \Delta x_2\\ \Delta y_2\\ \vdots\\ \Delta x_k\\ \Delta y_k\end{matrix}\right\} = \begin{bmatrix} F_{11} & F_{12} & 0 & 0 & \dots & & \\ F_{21} & F_{22} & 0 & 0 & \dots & & \\ 0 & 0 & F_{11} & F_{12} & \dots & & \\ 0 & 0 & F_{21} & F_{22} & \dots & & \\ \vdots & \vdots & \vdots & \vdots & \ddots & & \\ & & & & & F_{11} & F_{12} \\ & & & & & F_{21} & F_{22} \end{bmatrix} \left\{\begin{matrix}\Delta X_1\\ \Delta Y_1\\ \Delta X_2\\ \Delta Y_2\\ \vdots\\ \Delta X_k\\ \Delta Y_k\end{matrix}\right\} \tag{3.3}$$

This equation is written such that the components of the $\mathbf{F}$-tensor are arranged in a vector $\mathbf{F}^{\mathrm{v}}$ and the initial vectors $\Delta\mathbf{X}_i$ are collected in the matrix $\mathbf{A}$:

$$\left\{\begin{matrix}\Delta x_1\\ \Delta y_1\\ \Delta x_2\\ \Delta y_2\\ \Delta x_1\\ \Delta y_3\\ \vdots\end{matrix}\right\} = \begin{bmatrix} \Delta X_1 & \Delta Y_1 & 0 & 0 \\ 0 & & \Delta X_1 & \Delta Y_1 \\ \Delta x_2 & \Delta Y_2 & 0 & 0 \\ 0 & 0 & \Delta X_2 & \Delta Y_2 \\ \Delta X_3 & \Delta Y_3 & 0 & 0 \\ 0 & 0 & \Delta X_3 & \Delta Y_3 \\ \vdots & \vdots & \vdots & \vdots \end{bmatrix} \left\{\begin{matrix}F_{11}\\ F_{12}\\ F_{21}\\ F_{22}\end{matrix}\right\} \qquad \Longleftrightarrow \qquad \Delta\mathbf{x} = \mathbf{A}\,\mathbf{F}^{\mathrm{v}} \tag{3.4}$$

For the displacement measurements of the dots however, this equation cannot be fulfilled due to the noise and thus:

$$\Delta\mathbf{x} \approx \mathbf{A}\,\mathbf{F}^{\mathrm{v}} \tag{3.5}$$

In this work, a least squares approximation was used to determine $\mathbf{F}^{\mathrm{v}}$ such that the error in Equation (3.4) is minimised. Formally, the following residual function has to be minimised to find $\mathbf{F}^{\mathrm{v}}$:

$$g(\mathbf{F}) = \sum_{i=1}^{n} (\Delta x_i - F_{11}\Delta X_i - F_{12}\Delta Y_i)^2 + (\Delta y_i - F_{21}\Delta X_i - F_{22}\Delta Y_i)^2 \tag{3.6}$$

To determine $\mathbf{F}^{\mathrm{v}}$ from this equation is a lengthy operation. To this end, Equation (3.4) is rewritten such that Equation (3.6) is minimised:

$$\begin{aligned} \Delta\mathbf{x}^1 &= \mathbf{A}\,\mathbf{F}^v && \Longleftrightarrow \\ \mathbf{A}^{\mathrm{T}}\Delta\mathbf{x}^1 &= \mathbf{A}^{\mathrm{T}}\mathbf{A}\,\mathbf{F}^v && \Longleftrightarrow \\ \mathbf{F}^v &= (\mathbf{A}^{\mathrm{T}}\mathbf{A})^{-1}\mathbf{A}^{\mathrm{T}}\Delta\mathbf{x}^1 \end{aligned} \tag{3.7}$$

The advantage of this procedure is that the matrix $\mathbf{A}$ needs to be determined only once at the beginning of an experiment. Especially in a setting where the deformation is calculated in real time this is beneficial for the processing speed. With $\mathbf{F}$ in hand, following Equation (2.11), the velocity gradient can be calculated:

$$\mathbf{L}\Delta t \approx \Delta\mathbf{F}\cdot\mathbf{F}^{-1} \tag{3.8}$$

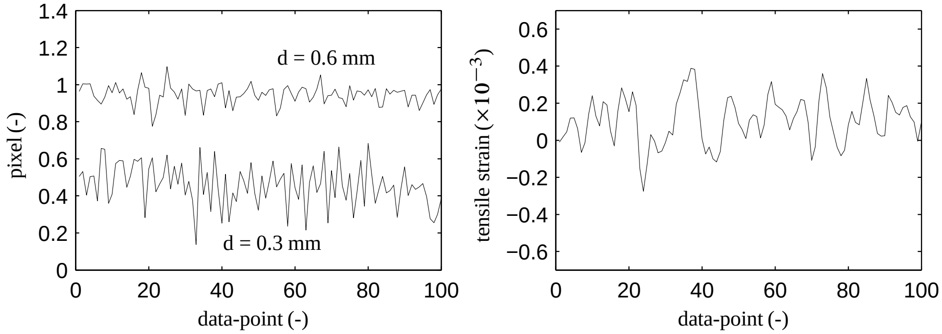

(a) The measured position of a dot with 0.3 mm and 0.6 mm diameters.

(b) The measured strain with dots of 0.6 mm diameter.

Figure 3.4: Properties of the deformation measurement in a stationary situation.

which is true if the time steps used are small. To present the results of the mechanical experiments of the samples tested on the TWENTE BIAXIAL TESTER, **L** is not decomposed in **D** and **W**, but the logarithmic strains are determined directly from **L**:

$$\Delta\boldsymbol{\varepsilon} = \mathbf{L} \tag{3.9}$$

This expression holds for small time steps and for proportional loading. For a non-proportional loading scenario that describes a deformation path with the final configuration equal to the final configuration, a non-zero strain may be obtained (Belytschko *et al.*, 2006). It is noted that the TWENTE BIAXIAL TESTER is also used for non-proportional strain paths, but for the presentation of results this is acceptable.

3.3.1 Accuracy of the strain determination

To measure the deformation of the material, 2 options were considered; strain gages and optical strain measurement. Strain gages are known for their high accuracy, but are not applicable to the small deformation area. The smallest strain gage that could measure tensile, transverse and shear strain was 3.5 mm high, which exceeds the 3.0 mm height of the deformation area. Also, strain gages and the smaller ones in particular are difficult to mount on the sample which would lead to a more lengthy procedure for the experiment. The optical strain measurement used here has the advantage of being accurate while it requires only limited amount of preparation time. In this section, the accuracy of the strain measurement with optical strain measurement is investigated.

The weighing function that determines the coordinate of the dot distinguishes between the edge of the dot and the centre of the dot. The “blackness” of the edge changes during a test because the sample moves with respect to the light source. This causes noise on the coordinate of the dot and hence also in the strain calculation. The influence of the dot size on the noise is illustrated in Figure 3.4(a) by means of 2 dots with different diameters; 0.3 mm and 0.6 mm. Smaller diameter dots than 0.3 mm cannot be made with the current tools. A dot with a diameter larger than 0.6 mm would contribute to an even higher accuracy of the measurement, especially if the deformation area is fully homogeneous. However, dots with a diameter larger than 0.6 mm do not seem to be realistic to represent a true “material point”. Hence, a diameter of 0.6 mm for the dots was chosen as a maximum. The dots are applied to the deformation surface by manually squeezing the silicon kit through a mask with the indicated diameters. It is recognised that this procedure does not allow for a perfect circular dot. Results of the stationary test show that the noise of the dot position of the large dot is ± 0.15 pixel and for the dot with diameter 0.3 mm the noise is approximately ± 0.30 pixel. Indeed, a larger dot gives better accuracy in the calculation of the its position.

Not only does the size of the dots matter, but also their relative position. For a good accuracy of both the tensile and shear deformations, the dots should be positioned on the corners of a virtual square. However, the deformation area of the sample measures $45 \times 3\,\mathrm{mm}^2$. When the complete deformation area needs to be captured with the camera with a square light cell, the relative resolution in the tensile direction will be lower than in the shear direction, because the shear direction can use the full view of the camera. To increase the relative accuracy of the tensile deformation measurement, the camera view was limited to a square of 12 mm of the total area of the deformation area. Due to the relative height of the deformation area, the dots are divided over 2 horizontal lines; an upper row and a lower row of dots (see Figure 3.1). To determine the tensile deformation, the accuracy is optimised by placing the 2 rows as close as possible to the lower and upper edge of the deformation area. In practise 1.7 mm distance between the 2 rows is used. The transverse and shear strains can be determined more accurately because the maximum distance between the dots on the left and on the right is 12 mm. Hence, the influence of the error in the horizontal dot position is spread over a large distance. Besides, vectors that connect 2 dots in the same row contain information only on the transverse deformation, which is assumed to be zero, due to the plane strain condition. In the calculation of the strain, only vectors connecting the upper with the lower row of dots are used, as the vectors in Figure 3.3. The distance between the 2 rows is approximately 150 pixels. The absolute error in the tensile strain, based on the mentioned data and for only one dot in the lower and upper row, is $2 \cdot 10^{-3}$ (-). This value is relatively poor, the elastic region of steel cannot be measured satisfactory with such an error.

Figure 3.4(b) shows the tensile strain in a stationary test in which 16 dots are used for the calculation of the strain. The size of the dots is 0.6 mm and 2 rows of 8 dots are applied. The strain is calculated according to Section 3.3. It shows that the error in this measurement is approximately $5 \cdot 10^{-4}$ (-). With this accuracy it is possible to observe the elastic domain in the tensile tests. Accurate measurements of the elastic behaviour is not the objective of the test equipment, but it can provide a useful indication of the elastic properties.

3.3.2 Validation

The strains in the biaxial test setup are measured by taking the average strain calculated from the positions of 16 dots on the surface of the deformation region. However, the stresses and strains are not uniform over the complete deformation area, due to boundary effects and slip between the clamps and the specimen. These phenomena lead to two effects that need to be investigated in greater detail:

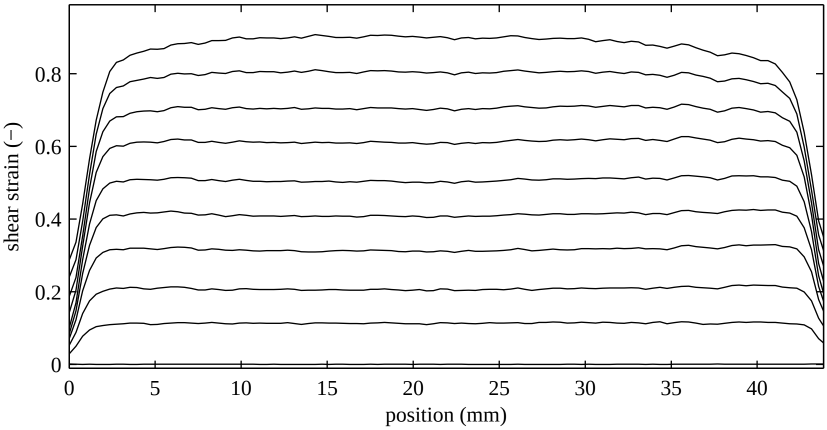

Figure 3.5: Results from ARAMIS in a simple shear test on DC06. The shear strain distribution on a cross section over the specimen is displayed for every 0.1 shear strain in the central region.

1. inhomogeneous deformation over the deformation area due to slip;
2. the transition from plane strain tension in the middle of the specimen to uniaxial tension at the free edge of the sample.

To assess the uniformity of the strain in the deformation area, the optical strain measurement system ARAMIS is used. With this digital image correlation software the local strains over the complete deformation area are measured. Results of the strain distribution for plane strain tension and simple shear are presented. The results are used to investigate the slip and the homogeneity of deformation.

The GOM ARAMIS 4M system, that is used in this work, consists of 2 cameras and software that calculates the deformation field. To interpret the surface of the deformation area, it is sprayed with a white background, after which a fine black speckle pattern is sprayed over it. The software recognises the surface of the deformation area, characterised by the black dots. The deformation area (45×3 mm) is "discretised" by ARAMIS in 165×11 recognised squares. All the squares define coordinates, which in turn are used to calculate the strains.

Figure 3.5 shows the results of the strain distribution in a simple shear test. A good strain distribution is obtained with the simple shear test, even at elevated strains. The edge effects are minor, at most 3 mm at each side of the specimen shows that the shear strain is zero at the very edge of the material. Approximately 95 % of the deformation area is in the same stress state.

Figure 3.6 shows the results of the tensile test with graphs of transverse strain, tensile strain and the R-value as a function of the horizontal coordinate through the middle plane of the specimen. Approximately 25 mm of the deformation area shows a transverse strain of approximately 0, indicating the plane strain condition. Towards the edges, material is

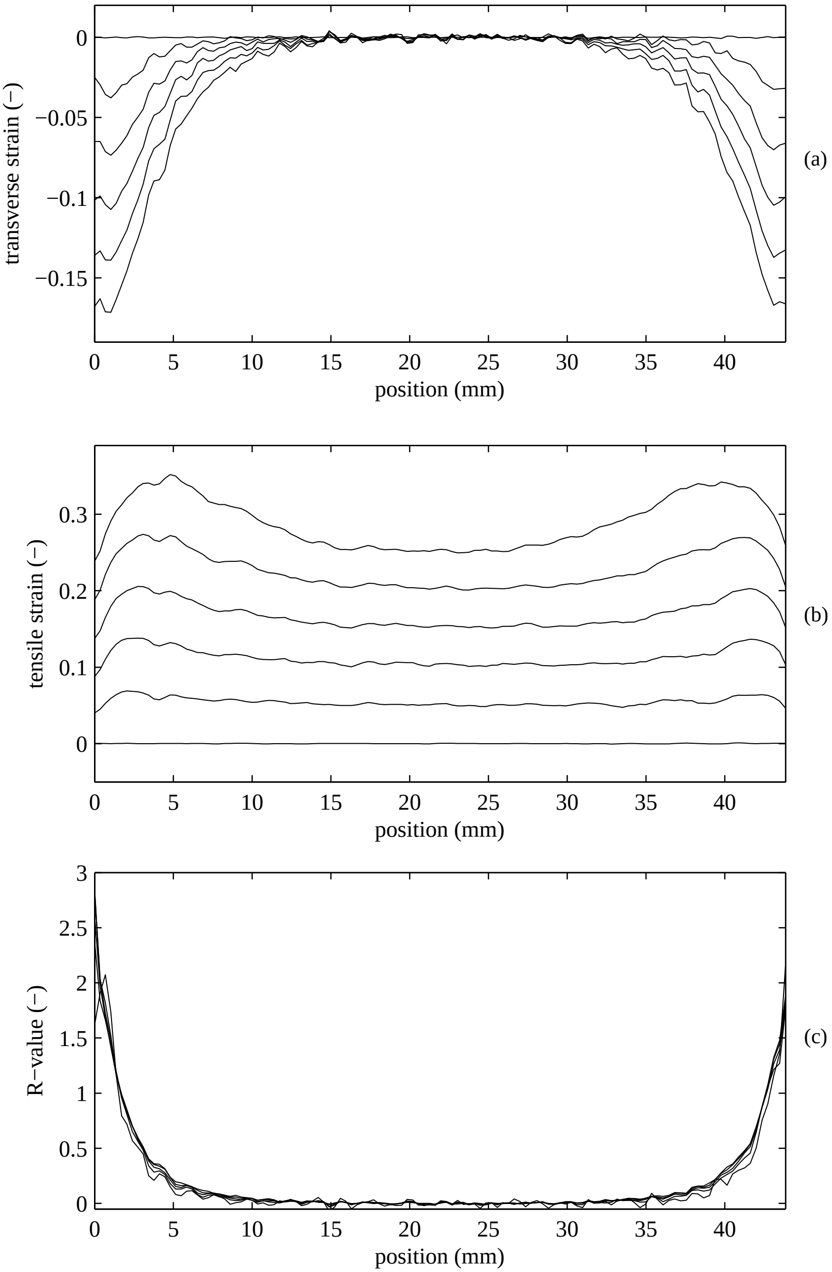

Figure 3.6: Results of a tensile test on DC06 captured with ARAMIS. Transverse strain(a), tensile strain(b) and the ratio of these (c) are plotted as a function of the horizontal position on the sample. The strains are measured along a line at half the height of the deformation area at intervals of 0.05 tensile strain in the central region.

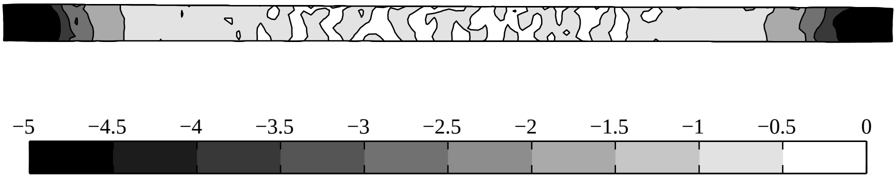

Figure 3.7: The distribution of the transverse strain over the sample at 15 % tensile strain.

pulled inwards, hence the plane strain condition gradually turns into the uniaxial stress state. The R-value is determined via Equation (2.7):

$$R = \frac{\varepsilon_y}{\varepsilon_z} = -\frac{\varepsilon_y}{\varepsilon_x + \varepsilon_y} \tag{3.10}$$

The R-value of DC06 equals 2.5, which is indeed observed at the left hand side of the specimen where the uniaxial stress state is present. On the right hand side of the specimen, this value is not clearly observed. The ARAMIS system cannot measure on the actual free edge of a material, and here the discretisation of the area is not close enough to the edge to capture the actual R-value. Furthermore, it is worth mentioning that from the distribution of R-values over the width of the specimen, it can be concluded that the ratio between the tensile and transverse strains is constant for all levels of tensile strain.

In Figure 3.6(b) it is shown that the tensile strain is not homogeneous over the width of the deformation area. Near the edges of the sample the tensile stain is larger than in the central region. Probably this is due to the clamping of the specimen. Four bolts are mounted at the sides of sample, near the edges of the deformation region. It is quite possible that the local forces from these bolts cause a non-uniform clamping force. It is expected that the edges would show the largest tensile strain, because that material is also closest to the bolts that provide the clamping. However, the peak of the tensile strain is not at the very edge of the sample but slightly shifted to the centre, depending on the amount of tensile strain. This may be due to the transverse stress that “draws” the material towards the centre of the specimen. In its turn, the transverse displacement of the material at the edges facilitates slip in the tensile direction. Due to the tensile slip, less strain is accumulated in the tensile direction. Figure 3.6(a) illustrates this reasoning. The transverse strain also does not show a peak at the edge, but closer to the centre of the specimen. Towards the edge, the transverse strain decreases. Furthermore, due to the different stress states of the edges and the central region, uniaxial tension and plane strain tension respectively, differences occur. For the plane strain deformation mode, the assumption of no plastic volume change can only be fulfilled if the thickness strain is of the same oder of magnitude as the tensile strain. At the edges, where the uniaxial stress state exists, the transverse and thickness strains together compensate the tensile strain. Hence, the material in the central region of the deformation area is more easily pulled away under the clamps due to a lower thickness.

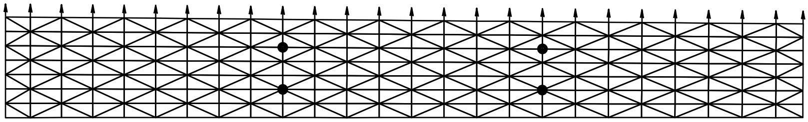

Figure 3.8: Undeformed mesh (not on true scale) of the deformation area, with the arrows showing the reaction forces and the circles indicating the 'dots' for the calculation of the global strain.

In this work, the material is considered to be in the plane strain condition if the tensile strain in the peaks is no more than 5 % higher than the strain in the central region. From Figure 3.6(b) it is observed that 15 % tensile strain in the central region is the boundary for which the deformation is still considered homogeneous. In actual experiments this is easy to control, because the central region is also used for the measurement of deformations.

Figure 3.7 shows the transverse strain distribution in the tensile test at approximately 15 % of tensile strain. This graph illustrates that the transverse strain does not have a gradient across the height of the specimen.

3.4 Stress measurement

In the former section, it was assumed and verified that the strain field is uniform. In this section it is assumed that the stress is homogeneous, at least within the strain domain at which the plane strain condition is fulfilled. The true stresses are determined from the force sensor and the current cross sectional area of the deformation zone. The current thickness is calculated with the thickness strain that is determined from the transverse and tensile strain and the assumption that the material does not show plastic volume changes:

$$\varepsilon_z^{\mathrm{p}} = -\left(\varepsilon_x^{\mathrm{p}} + \varepsilon_y^{\mathrm{p}}\right) \tag{3.11}$$

Which is used in the calculation of the tensile simple shear stress

$$\sigma_y = \frac{F_{yy}}{\text{width} \times \text{thickness} \times \exp \varepsilon_z^{\mathrm{p}}} \tag{3.12}$$

$$\sigma_{xy} = \frac{F_{xy}}{\text{width} \times \text{thickness} \times \exp \varepsilon_z^{\mathrm{p}}} \tag{3.13}$$

The validity of this calculation depends on the assumption of the homogeneous stress distribution across the deformation area. This is investigated in the next section.

3.4.1 Validation

This section describes FE simulations to assess the stress field over the deformation area. To this end the coordinates of the squares, derived by the ARAMIS system, are used to define an initial mesh. The displacements of the upper and lower boundary nodes of the deformation area are used to describe the displacement and deformation. In this way, the

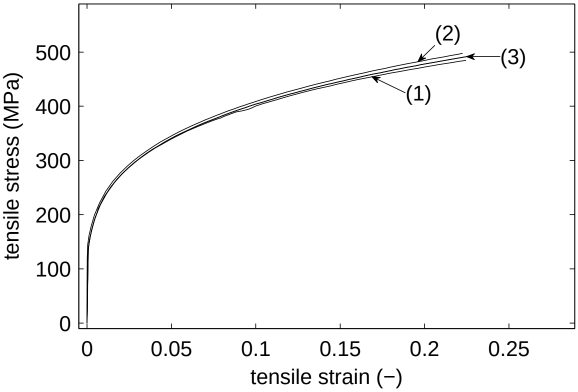

Figure 3.9: Stress–strain curves for the 3 simulations.

exact deformation experienced by the material is used in the FE-simulation. The Hill ’48 yield criterion and isotropic hardening according to Swift is used to model the material behaviour. Simulations are only performed for the plane strain tension test, since the homogeneity of the deformation area in the simple shear test is assumed to be sufficiently accurate.

Three simulations are performed to investigate the homogeneity of the stress state in plane strain tension. The first simulation uses the mesh and boundary conditions defined by the measurements from ARAMIS. The stress–strain curve is calculated in a similar way as the procedure in the experiments. The tensile force is determined by summarising the individual tensile forces on the upper boundary nodes (see arrows in Figure 3.8). The strains are determined by tracing 4 nodes in the mesh, representing the dots on the specimen (the circles in Figure 3.8) and calculating the strain from that. The second simulation is a one-element test to display the actual stress–strain curve of the material. This simulation represents the true mechanical behaviour. In the third simulation, the ideal experiment is imitated. A perfectly rectangular mesh is used for the representation of the deformation area. The upper and lower boundary nodes are constrained in the horizontal direction and the tensile test is simulated by moving the upper boundary nodes in the vertical direction. The stress and strain are calculated as in simulation 1. Hence, slip and non-uniform deformation due to slip is excluded in this simulation. It is expected that the stress–strain curves from simulation 2 and 3 coincide. Simulation 3 only shows the influence of the boundary effects near the free edges. Indeed, Figure 3.9 shows that the stress-strain curve of simulation 3 is only slightly lower than the actual material behaviour represented by simulation 2. Simulation 1 represents the actual test with the TWENTE BIAXIAL TESTER. Due to slip in the clamps, the sample is not uniformly stretched, resulting in a stress–strain curve that is 2 % lower at 22 % tensile strain.

Similar global stresses in the simulations do not necessarily indicate that the plane strain tension test is a good representative for the constitutive behaviour under plane strain conditions. To this end the tensile stresses are examined, see Figure 3.10. The shown stress

Figure 3.10: Calculated tensile stress distribution in the sample at 15 % of tensile strain.

distribution is at 15 % tensile strain, since this strain reflects the boundary for homogeneous tensile deformation. It is remarkable that despite the significant slip between the clamps and sample, the tensile stress appears to be very homogeneous over the specimen. Boundary effects are observed at the free edges, but 85 % of the tensile stress lies between 440 and 465 MPa. Towards the edges, the stress drops to 340 MPa. This can be partially attributed to the present uniaxial tensile stress state because of the free edge. On the other hand, as observed in Figure 3.6, slip is present in this area, leading to a lower tensile strain and thus a lower stress.

3.5 Strain path control

The biaxial test equipment was designed to test materials on non-proportional strain paths. However, the finite stiffness of the machine itself plays a crucial role here, which was already noted in a theoretical study by Kuroda and Tvergaard (1999). The clamp displacement needs to be controlled during non-proportional tests, but the controls act on the displacement of the actuators. The force is transmitted from the actuators to the clamps via solid steel bars, bolts and bearings. Due to the limited stiffness of these parts, the displacement is not accurately controlled. Naturally, this problem occurs also in regular tensile tests, but the mechanical equipment can be made stiffer because only tensile deformation is required.

A significant influence is observed when an orthogonal test is performed without unloading, see Figure 3.11. In the first part of the experiment tensile deformation is applied. Hereby the material stretches, the stress increases, but the test equipment itself is also stretched. During the shear deformation, the vertical distance between the lower and upper clamp should remain constant. However, because of the changing stress state in the material, the tensile stress drops. This in turn releases the force in the equipment and the stretching relaxes, moving the clamps from each other and hence increasing the tensile strain in the specimen. With decreasing tensile stress a new equilibrium is found, but at the cost of more tensile strain and hence higher tensile stresses. The outcome of such a test is shown in Figure 3.12. It shows that the tensile strain is increased by 6 % in the shear phase of the test. This clearly indicates that to perform experiments with continuous orthogo-

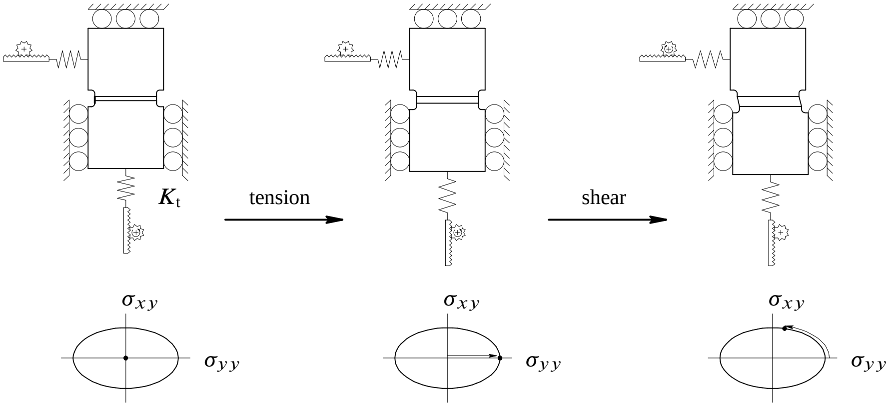

Figure 3.11: Scheme of the orthogonal test in the biaxial test equipment.

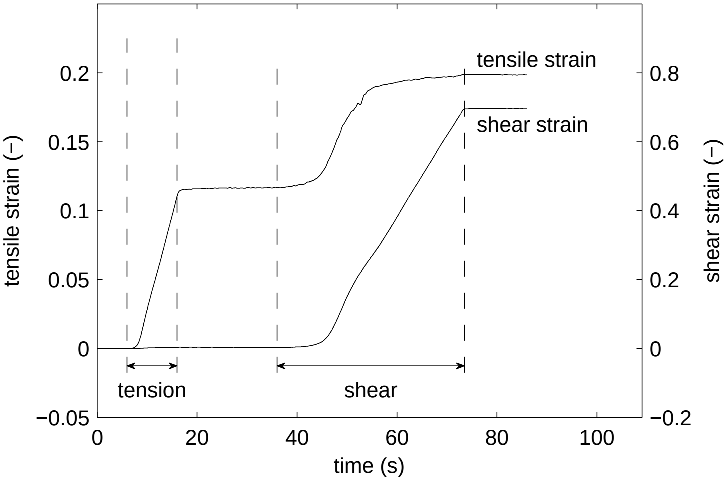

Figure 3.12: Tensile and shear strains during an orthogonal test as a function of time.

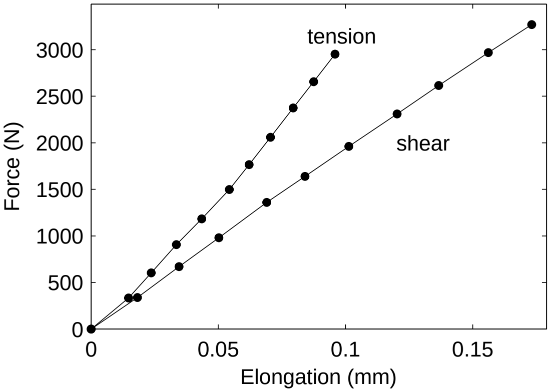

Figure 3.13: Force as a function of the actuator displacement. The dots indicate the measurements.

nal strain paths the flexibility in the frame must be compensated. This is explained in the following section.

Stiffness compensation

To determine an algorithm for compensation of the stiffness, it was first examined how the test equipment responds to forces. The stiffness of the machine is examined by making a force–displacement curve of the test equipment itself. An infinitely stiff sample is mimicked by placing a solid steel block between the clamps. As such, the measured displacement is purely a function of the test rig, not of the tested material. The displacement of the actuator was measured manually and the force was measured with the force sensor. The results of this test are plotted in Figure 3.13. A linear relation can be recognised for the simple shear direction; the stiffness was found to be $K_\mathrm{s} = 18 \cdot 10^3\,\mathrm{N/mm}$. In the tensile direction a nonlinearity is observed at the initiation of the force. The stiffness for the linear part ($F > 1500\,\mathrm{N}$) is: $K_\mathrm{t} = 35 \cdot 10^3\,\mathrm{N/mm}$. Because the nonlinearity is only observed at lower forces, a simple linear relation is exploited to compensate for the stiffness of the machine:

$$\mathrm{d}F = K_\mathrm{t}\,\mathrm{d}y \tag{3.14}$$

This equation is discretised such that it can be used in an open loop feedback system:

$$\Delta y = \frac{\Delta F}{K_\mathrm{t}} \tag{3.15}$$

The force increment ΔF is determined by two subsequent force measurements within a certain time interval. The incremental stretch of the test equipment (Δy) is the result of the force interval divided by the stiffness of the test equipment. The value of Δy is used as a prediction for the stretch during the next time interval and as such prescribed to the actuator. This program is implemented in the motion controller (Figure 3.2(b)) and successfully applied in Section 4.5.2.

To really prescribe the strain path in experiments, a feedback system based on the strain measurement is required. The algorithm described above provides a control loop for orthogonal strain path changes, but not for an arbitrary strain path. This proved to be challenging due to some technical issues, whereby this is not easily embedded in the software. The advantage of feedback on force, as presented in (3.15), is that the feedback loop is implemented in the controller, see Figure 3.2(b). The controller handles loops, including a force reading, at a maximum rate of $500\,\mathrm{s}^{-1}$. The strain measurement however, is done on the PC with LABVIEW, at a maximum rate of $35\,\mathrm{s}^{-1}$. Some tests were performed with feedback on strain, but due to the low rate of data acquisition, the strain could not accurately be controlled. For future work, it is worth investing this feedback, because the versatility of the test equipment could be increased significantly.

3.6 Conclusion

This chapter introduces the biaxial test equipment and its characteristics. It explains the procedures and the setup of the total experimental rig. To assess the uniformity of the deformation field in a tensile and shear test, the ARAMIS system was used to measure the strains in the complete deformation area. It shows that a uniform deformation field is obtained in simple shear deformation. In tensile deformation, the thickness is reduced, which facilitates slip of the sample from between the clamps. In experiments with a tensile strain higher than 15 % in the central region of the sample, the difference with tensile strain at the edge of the sample may exceed 5 % strain. Hence, to assure the plane strain condition in the sample, tensile strains should be considered up to 15 %.

The strain measurement in a regular experiment is captured by tracing 16 black silicon dots that are applied to the surface of the deformation area. It was shown that larger dots give a better accuracy of the dot position. Due to the large number of dots, the least squares optimisation of the strain provides a low level of noise on the strain measurement. The accuracy of the tensile test was at least $\varepsilon \pm 5 \cdot 10^{-4}$, which is sufficient to give an indication of the elastic properties. The shear strain can be determined more accurately, because the dots are further apart in the transverse direction. The stress distribution of the plane strain test was examined with FE-simulations, which show that the plane strain tension test presents the stress curve accurately to $\varepsilon = 15\%$ tensile strain. Hence the stress–strain curve in plane strain tension can be accurately measured up to $\varepsilon = 15\%$ tensile strain. For simple shear deformation, the strain is uniform over the sample, and thus the related stress is also uniform. The stress-strain curve for simple shear can therefore be used in the complete deformation domain of the TWENTE BIAXIAL TESTER.

For controlling experiments, and in particular non-proportional tests, it was shown that the limited stiffness of the test equipment can affect the prescribed strain path. A compensation algorithm was implemented based on the feedback of force and successfully applied in Chapter 4.

4. Experiments

Mechanical experiments serve to establish material properties that are required for engineering applications of these materials. The goal of this chapter is to investigate actual strain path sensitive behaviour. Based on the observed phenomena, material models will be elaborated in Chapter 5. The experiments show the mechanical behaviour during proportional and non-proportional deformation, and are used to determine the material parameters. Additional non-proportional experiments, in which cyclic shear and tension are combined, were performed to validate the material models. The mechanical behaviour was tested using the TWENTE BIAXIAL TESTER because different strain paths and different strain path changes can be applied to the materials. For that reason the uniaxial tensile test, which would be an obvious choice for materials research, is not used in this work. In this thesis only the mechanical behaviour is considered; texture and microstructure evolution are not investigated in the experiments.

Firstly, the test scheme is introduced. In Section 4.2, the anisotropic yielding behaviour of the materials is discussed. The influence of the strain rate on the stress–strain curves is investigated in Section 4.3. Cyclic tests are discussed in Section 4.4.1 and the orthogonal experiments and the characteristic material behaviour is discussed in Section 4.5.

4.1 Outline of experiments

For more advanced material models, experiments with monotonic, cyclic and orthogonal deformation paths need to be performed. Issues that are relevant for research are the strain rate dependency; the anisotropy in initial yielding; the Bauschinger effect and the cross-hardening effect. The following tests were performed to examine these phenomena:

Monotonic tests Monotonic tests were performed in the plane strain tension direction and in simple shear. Experiments with different strain rates were performed to determine the reference strain rate in the experiments. To examine the anisotropy, experiments with different loading directions with respect to the rolling direction were performed. DC06 was used to determine the reference strain rate and to explore the anisotropy.

Cyclic tests To investigate the Bauschinger effect, reverse shear tests were performed. The pre-strain was varied in these tests to observe the evolution of the phenomenon. Three strokes were applied, such that two loading reversals were applied. From the literature on similar experiments, the phenomena illustrated in Figure 4.1 were expected: *i*) the *Bauschinger effect* is the phenomenon whereby the flow stress after

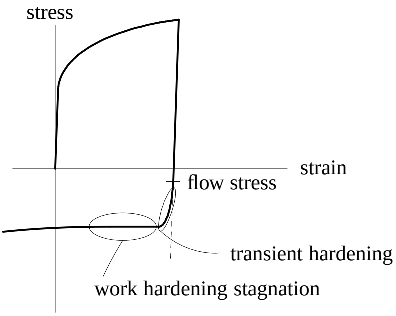

Figure 4.1: The different phenomenon in cyclic loading.

the load reversal is lower than before the load reversal. At the same time, the flow stress after the load reversal is often hard to determine because of the smooth transition from elastic to plastic deformation. For the definition of the Bauschinger effect, the flow stress after the load reversal is defined as the stress where the curve starts to deviate from the linear line. *ii*) *Transient hardening* is the term used to indicate the smooth transition from the elastic to the plastic regime. *iii*) When the material is again plastically loaded after the load reversal, some materials show *work hardening stagnation*, *i.e.* the stress does not increase during reverse loading. With increasing strain, hardening is resumed.

Orthogonal tests In the experiments with orthogonal strain path changes, 2 sequentially linear, but orthogonal, strain paths, are prescribed. The TWENTE BIAXIAL TESTER is used to change the strain path from plane strain tension to simple shear. The shear direction is perpendicular to the tensile direction. Strain path sensitive material shows the typical overshoot after the strain path change; the so-called cross-hardening. These tests were performed with elastic unloading after the applied tensile deformation. In true deep drawing processes, however, it is more likely that an orthogonal strain path change takes place without unloading. For that reason the orthogonal strain path change was also investigated for a continuous stress path, by omitting the intermediate elastic unloading. Additionally, the experiments without elastic unloading were used to obtain an indication of the local shape of the yield locus.

4.2 Anisotropy

Steel sheets are produced from solid blocks of steel by rolling, which introduces a texture in the material. Hence, the mechanical behaviour of the material is direction dependent. For the materials used here, the anisotropy is known and has been quantified by Corus. DC06 was used as a test case to verify that the data from the experiments performed on the TWENTE BIAXIAL TESTER could be used alongside the data from Corus. Plane strain

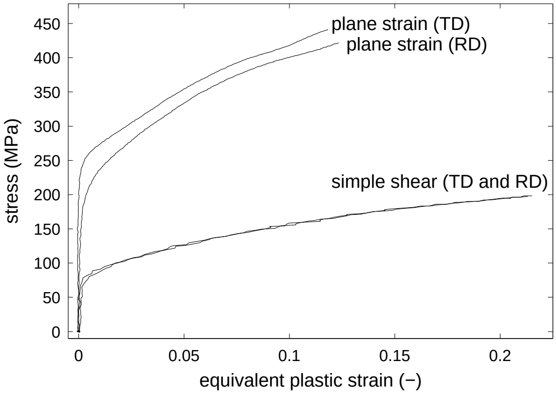

Figure 4.2: Experiments on DC06 for the transverse and rolling direction. The strain rate is constant for all tests: $\dot{\varepsilon} = 1 \cdot 10^{-2} s^{-1}$.

tension tests in RD and TD were performed, and a simple shear test with the shearing direction parallel to the TD was done. Because the simple shear test is actually a pure shear test at 45° (Figure 4.3), experiments were performed at 0°, 45° and 90° with RD. It is recognised that anisotropy is normally determined with uniaxial tensile tests, but in this work the relation between the external experimental work and the experiments on the TWENTE BIAXIAL TESTER needed to be confirmed.

The results of the experiments are presented in Figure 4.2. Two phenomena are observed in these tests; *i)* the initial flow stress in the transverse direction is clearly higher than the stress in the rolling direction and the stress–strain curve of the transverse test remains above the stress–strain curve from the tensile test in RD. *ii)* The elastic–plastic transition is more pronounced in the transverse test compared to the test in the rolling direction. The experimental values from Figure 4.2 were compared with the measurements from Corus and the agreement was satisfactory.

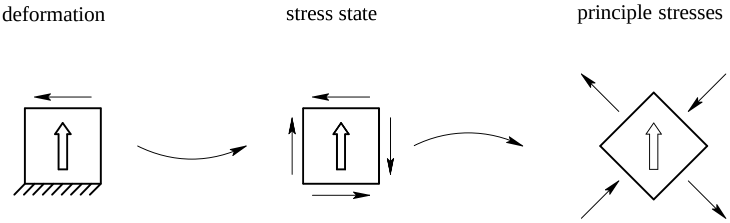

Figure 4.3: Simple shear in the transverse direction. The block arrows indicate the RD.

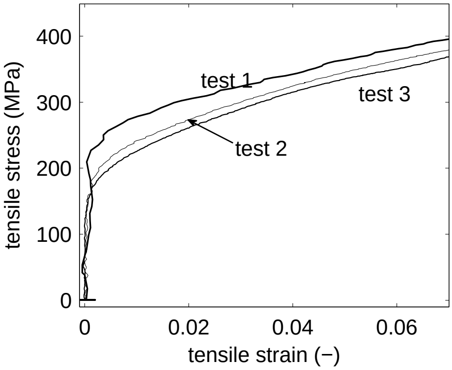

Figure 4.4: Plane strain tension tests on DC06 with different strain rates. The strain rates are: $0.065\,s^{-1}$, $0.011\,s^{-1}$ and $0.005\,s^{-1}$ for Tests 1, 2 and 3, respectively.

4.3 Strain rate effects

The goal of this section is to determine a reference strain rate for the experiments of the investigation of strain path sensitivity. The maximum strain rate in the experiments is constrained by the maximum rate at which the deformation can be logged. The camera captures the images and from experiments with different settings of illumination, dot size and the size of the area that is recorded, it was observed that the maximum frame rate is approximately $30\,s^{-1}$. The minimum strain rate is not constrained, but needs to be representative for forming process. Also, in the experiments performed on the TWENTE BIAXIAL TESTER large strains can be applied to the sample. From a practical point of view, it is desirable to keep the time required for the experiment as short as possible.

In Figure 4.4 three plane strain tensile experiments on DC06 with different strain rates are presented. In test 1 a strain rate of $0.065\,s^{-1}$ was measured. It is observed that the number of data points in this experiment was relatively small, leading to a rough stress–strain curve. Test 2 has a strain rate of $0.011\,s^{-1}$. In comparison with test 1, the stress–strain curve of test 2 has a smooth evolution, without the bumps observed in test 1. In test 3 a strain rate of $0.005\,s^{-1}$ was applied. As test 2, the stress–strain curve is smooth.

The mechanical behaviour of the DC06 under different strain rates is comparable. The curves show a similar trend, only test 1 shows an awkward “bump” at the start of the deformation. This may be due to the sudden application of the force to the test equipment, causing a vibration in the construction and leading to a jump in the force. Quantitatively, the measured flow stress increases with increasing strain rate.

To exclude the influence of strain rate in the experiments, the strain rate should be as low as possible. However, from a technical point of view this is not possible and hence a reference strain rate of $0.01\,s^{-1}$ in equivalent plastic strain was chosen for the remainder of the tests.

4.4 Cyclic deformation

In this section different experiments with cyclic shear on the TWENTE BIAXIAL TESTER are discussed. Firstly, the experiments with only cyclic shear are discussed. These experiments will be used in Chapter 5 to determine the parameters of the material models. Additionally, experiments with cyclic shear under continued plane strain tensile deformation were performed. These tests are used in Chapter 6 to validate the material models presented in Chapter 5. The strain rates for these tests are approximately $0.01\,s^{-1}$.

4.4.1 Cyclic shear

The experiments with cyclic shear are presented in this section. Different amounts of pre-strain were used in these experiments to determine the contribution of pre-strain. To apply the shear deformation to the sample, a prescribed amount of displacement was imposed on the actuator. Due to the limited stiffness of the test equipment, not all the displacement of the actuator was transferred to the sample (see also Chapter 3). Hence, a thicker specimen or a specimen with a higher flow curve is strained less than a specimen with a lower flow curve. This explains the different amounts of pre-strain between the different materials. In the reverse stroke, the actuator is moved to its maximum displacement. In the third stroke, the maximum displacement is again covered, but in the opposite direction.

DC06 In Figure 4.5 the results of 3 cyclic tests on DC06 are presented. A characteristic of mild steel is the pronounced Bauschinger effect, observed in all experiments for both reversals. This effect is relatively large, approximately 80 MPa. Transient hardening occurs after all reversals, but the effect seems to be independent of the amount of pre-strain. For all the experiments, for the first and second reversals, the transient hardening appears within approximately 2.5 % shear strain. The stagnation of work hardening was found to increase with pre-strain. As described in Chapter 2 this effect is caused by the piled up dislocations that are released from their position after the load reversal. The easy migration of the dislocations facilitates the deformation, which leads to a lower flow stress. After the first load reversal, the change from the work hardening stagnation to continued hardening can be clearly determined. After the second load reversal, the hardening rate is so low that the difference between regular hardening and the stagnation cannot be distinguished.

AA5182 From experimental results, depicted in Figure 4.6 it is observed that AA5182 shows the Bauschinger effect, but not as pronounced as DC06 does. In experiment 3 the Bauschinger effect is approximately 50 MPa. The transient hardening effect takes place within the first 2.5 % after the load reversal. Stagnation of work hardening does not occur, even if the pre-strain is relatively large. In these experiments, all the samples fail at the second load reversal. Despite the lower stiffness of AA5182, the strains at the end of the strokes are lower compared to the DC06 material. This is due to the larger thickness of AA5182 compared to DC06, 1.0 mm and 0.7 mm respectively. Hence, AA5182 requires more force, and because the displacement is prescribed at the actuator, more elongation is absorbed by the test equipment and does not contribute to the shear deformation in the specimen.

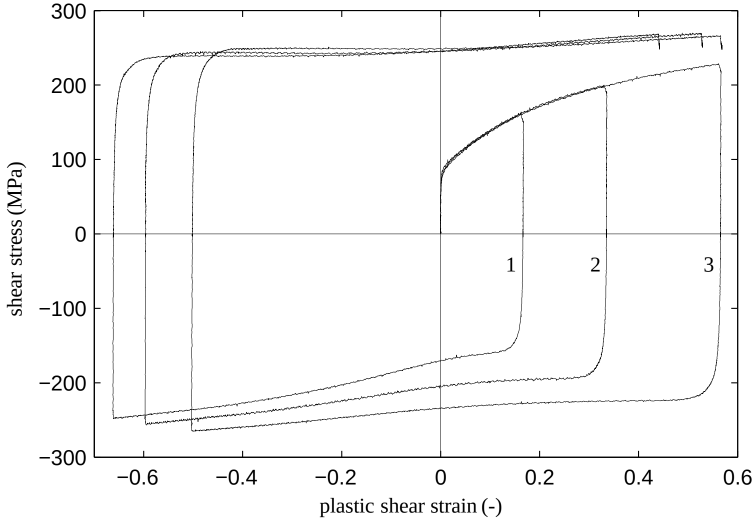

Figure 4.5: Cyclic tests in simple shear on DC06.

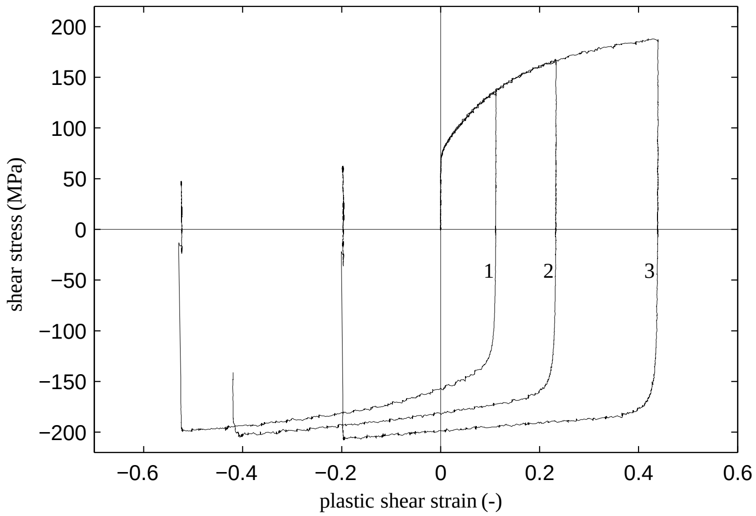

Figure 4.6: Cyclic tests in simple shear on AA5182.

H340LAD The results of the experiments with cyclic loading on high strength steel are presented in Figure 4.7. The largest Bauschinger effect was observed in experiment 3 and was approximately 120 MPa. The transient effect in this material was smeared out

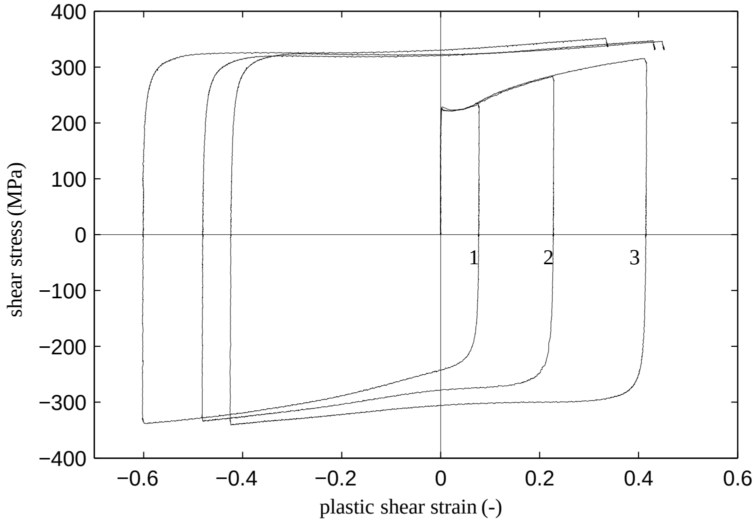

Figure 4.7: Cyclic tests in simple shear on H340LAD.

over more shear strain; in all the experiments 7.5 % was required, for the first and second load reversals. This material shows pronounced work hardening stagnation after the first load reversal and after the second reversal the flow stress even drops. Apparently, the deformation in the second stage of experiments 2 and 3 was so large that the work hardening stagnation changed to softening of the material. None of the H340LAD samples failed in the cyclic shear experiments.

DP600 This material differs from the other materials due to the large transient effect after the load reversal, see Figure 4.8. The transition in the reverse stroke from the elastic to the plastic regime requires approximately 12 % shear strain. The Bauschinger effect is observed and is approximately 100 MPa in the test 3 with the largest pre-strain. Stagnation of the work hardening was present in experiments 2 and 3, but was not observed in experiment 1, since the transient hardening effect dominates the local stress–strain relation.

4.4.2 Cyclic shear under tension.

In this section a special class of cyclic experiments are presented. The sample is loaded with cyclic shear, as in Section 4.4.1, and continued plane strain tension is applied during the cyclic shear. The mechanical properties in the TWENTE BIAXIAL TESTER required different settings in the controls of the actuators, depending on the tested material. This leads to different ratios between the tensile and shear loads in the following experiments for the 4 materials.

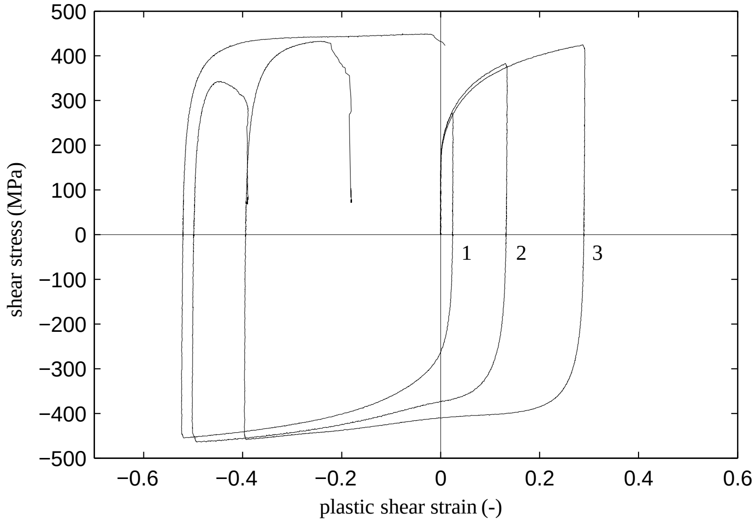

Figure 4.8: Cyclic tests in simple shear on DP600.

DC06 For DC06 three tests were performed where the ratio between tensile and shear deformation was changed, see Figure 4.9. In test 1 the contribution of the shear deformation was dominant. In the first stage of the experiment, both the tensile and shear components show an ordinary hardening curve. In stress space, Figure 4.9(c), the shear and tensile stresses do not increase proportionally. A small kink is observed, which is due to the different mechanical properties of the material in the elastic and plastic regime. The strain path change leads the stress state linearly through the elastic region, Figure 4.9(c). In Figure 4.9(b) this is shown as a drop to a negative shear. The tensile stress increases with a sudden jump of 120 MPa in stress Figure 4.9(a). Because the stress state translates through the elastic region, only a small increase in tensile and shear strain is observed during the strain path change. As the material becomes plastic again, the shear stress increases further (Figure 4.9(b)), but the tensile stress drops (Figure 4.9(a)). It was observed that the specimen did not show any sign of necking until this point. Experiment 3 has the largest contribution from the tensile deformation and shows a similar trend as experiment 1. However, in experiment 3 the tensile stress does not drop after the strain path change. Additionally, test 3 in Figure 4.9(b) shows that the elastic regime in the shear curve is relatively small. The stress path, Figure 4.9(c), shows that the supposed elastic behaviour is not linear during the strain path change. For this experiment the stress state could be called elastic or plastic. Figure 4.9(a) and 4.9(b) show that at the end of experiment 3, the regular stress curve is resumed and again dominated by the tensile deformation. Experiment 2 falls in-between tests 1 and 3 and has characteristics of both experiments.

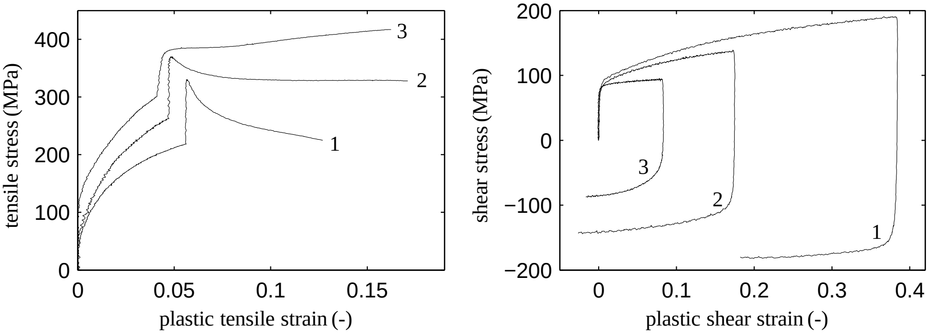

(a) The tensile stress–strain component.

(b) The shear stress–strain component.

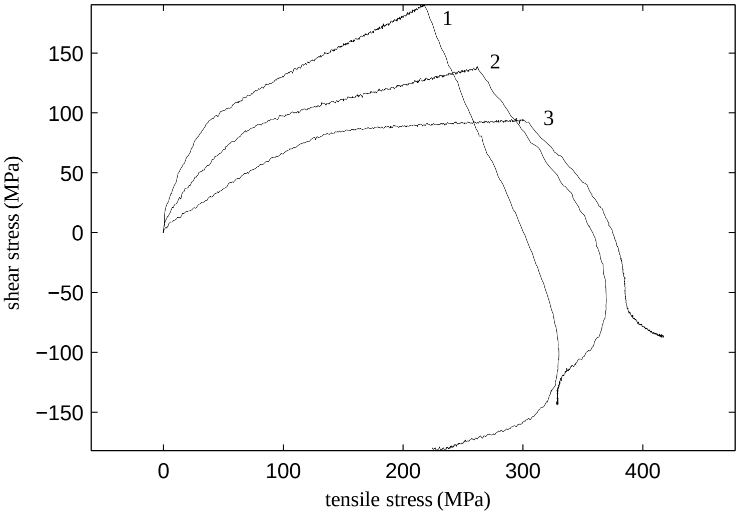

(c) The followed stress paths.

Figure 4.9: 3 different ratios of combined tension–simple shear experiments on DC06.

AA5182 For the aluminium two tests were performed, Figure 4.10. In general, the results of these experiments are similar to the results of DC06. It is striking that the material fails at the end of the load reversal in shear. The DC06 material still hardened after this point.

H340LAD Figure 4.11 shows the results for the high strength steel. Experiment 1 shows the largest contribution to the shear deformation. In the pre-strain phase, 2 kinks are observed in the stress path, Figure 4.11(c). The first kink is a nonlinearity in the shear stress evolution, see also Figure 4.12. The second kink is the transition from elastic to plastic deformation. This behaviour is not dependent on the test equipment because the experiments on the other materials do not show this behaviour. Experiment 2 in Figure 4.11(b) shows

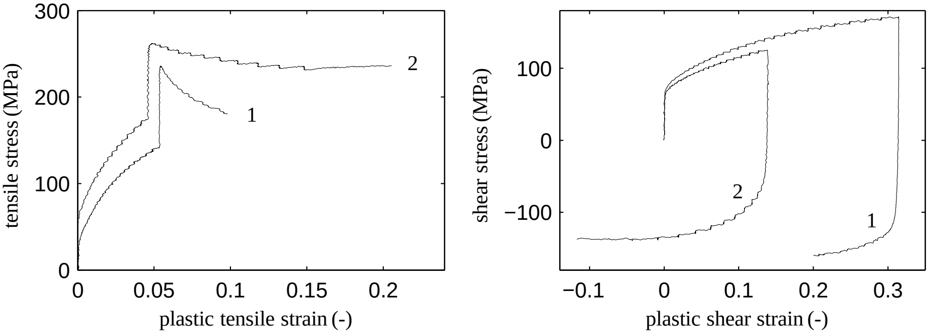

(a) The tensile stress–strain component.

(b) The shear stress–strain component.

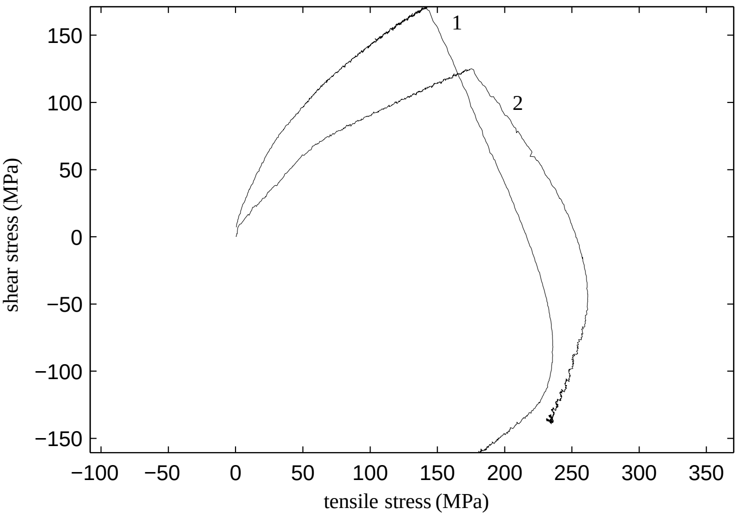

(c) The followed stress paths.

Figure 4.10: Combined tension–simple shear experiments for 2 different ratios on AA5182.

the same phenomenon, but at a higher stress and less pronounced. Experiment 3 does not show the kink in the curve. Experiment 1 again shows a kink in the elastic region right after the load reversal. The kink in the pre-strain phase occurs at $\sigma_{\text{sh}} \approx 120\,\text{MPa}$ and in the reverse stroke at $\sigma_{\text{sh}} \approx 150\,\text{MPa}$. In both situations the stress paths before and after the kink are linear. Because the elastic behaviour of the metals was not investigated in this research, this phenomenon is further left out of consideration. Experiments 2 and 3 do not show elastic behaviour after the load reversal. Both stress paths show a gradual trend to the negative shear stress. Experiment 1 does show some monotonic hardening at the end of the load reversal. Still, all the samples fail at the end of the load reversal.

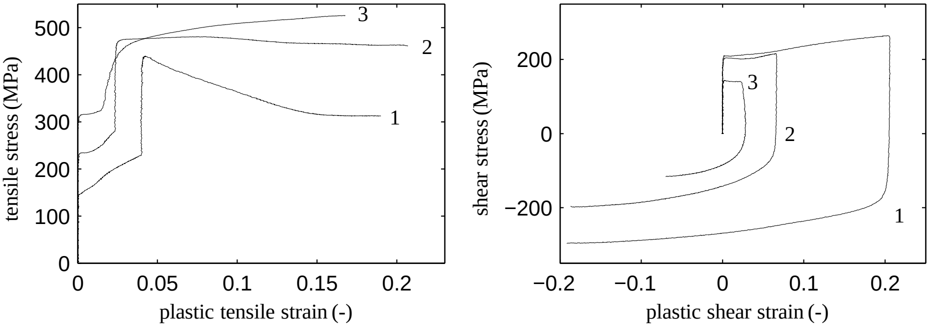

(a) The tensile stress–strain component.

(b) The shear stress–strain component.

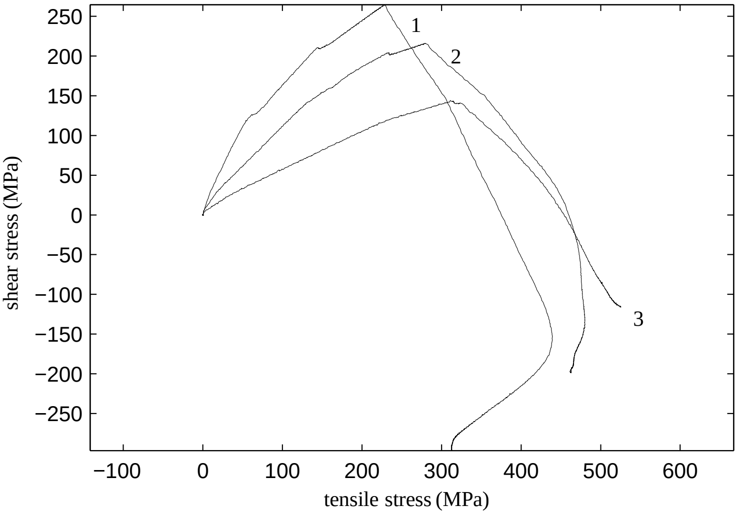

(c) The followed stress paths.

Figure 4.11: Combined tension–simple shear experiments for 2 different ratios on H340LAD.

4.4.3 Conclusion

The experiments with cyclic loading show the Bauschinger effect and the transient hardening effect for all the materials. Especially, H340LAD shows a strong sensitivity to load reversals. Experiments with combined reversed shear under tensile loading show the mechanical behaviour when a strain path is prescribed that in general is not used for the fitting procedure of material models. It is a good option to validate the material models with these tests. The TWENTE BIAXIAL TESTER is especially suited for this research since it allows for the accurate measurement of mechanical behaviour under cyclic loading.

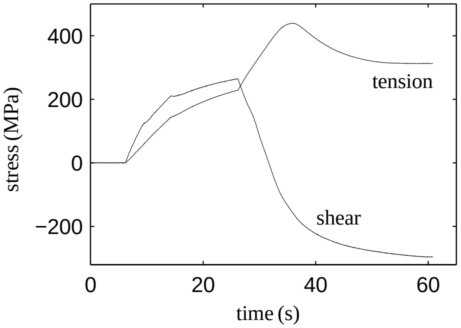

Figure 4.12: Stresses as a function of time in experiment 1 from Figure 4.11.

4.5 Orthogonal tests

In this section, experiments are presented in which the loading direction in strain space is changed perpendicular to the initial loading direction. The TWENTE BIAXIAL TESTER can load a specimen in simple shear and in plane strain tension, and these loading directions were used to investigate the mechanical behaviour. As discussed in Chapter 1, the effect of intermediate elastic unloading between 2 orthogonal deformation paths was a debated issue in the literature. Experiments with elastic unloading are presented in Section 4.5.1. Section 4.5.2 shows the results of similar orthogonal tests but without intermediate elastic unloading. The comparison of the results allows for a conclusion on this debate. Furthermore, Section 4.5.2 shows the results of experiments with gradual strain path changes. An impression of the yield surface in stress space was obtained from these experiments.

4.5.1 Cross-hardening effect

Figure 4.13 shows the results of the orthogonal test on DC06 where the material is elastically unloaded after the tensile deformation. This happens at an equivalent plastic strain of 12 %. At the peak of the tensile curve, the actuator displacement is terminated. After that, a small time interval is implemented, after which the tensile stress is decreased to zero by the actuator displacement. During the time interval, the hardening due to the strain rate disappears, hence the yield stress drops. This makes that the machine releases some of its elastic deformation, and the tensile strain in the specimen increases, see also Section 3.3. This effect causes an additional plastic strain of 1.5 % and a stress drop in this interval of approximately 40 MPa. After that the tensile stress is completely released, and the shear deformation is applied. Clearly visible is the overshoot with respect to the monotonic simple shear curve, at its highest point of 35 MPa. As the deformation continues the shear stress remains constant until it equals the stress (at $\varepsilon_{\mathrm{eq}} \approx 0.26$) in the monotonic test. From there on the regular hardening path is followed.

Additionally, an experiment with a strain rate change and an orthogonal strain path change was performed on DC06. This experiment was performed to show the correlation between a strain path change and a strain rate change. In this experiment, the plane strain

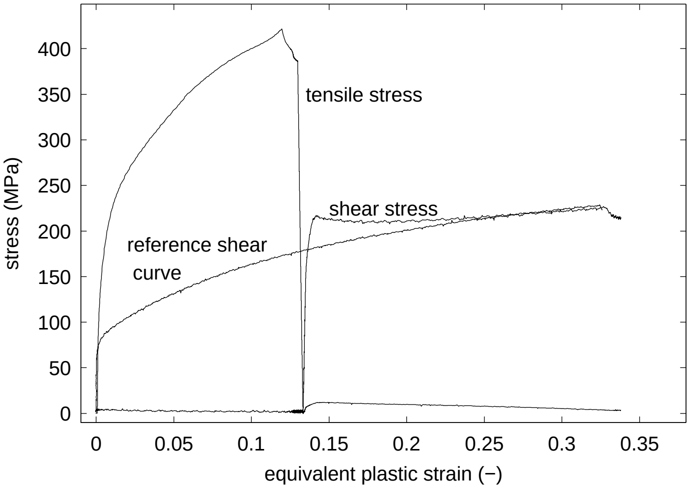

Figure 4.13: Orthogonal test with elastic unloading after the tensile deformation.

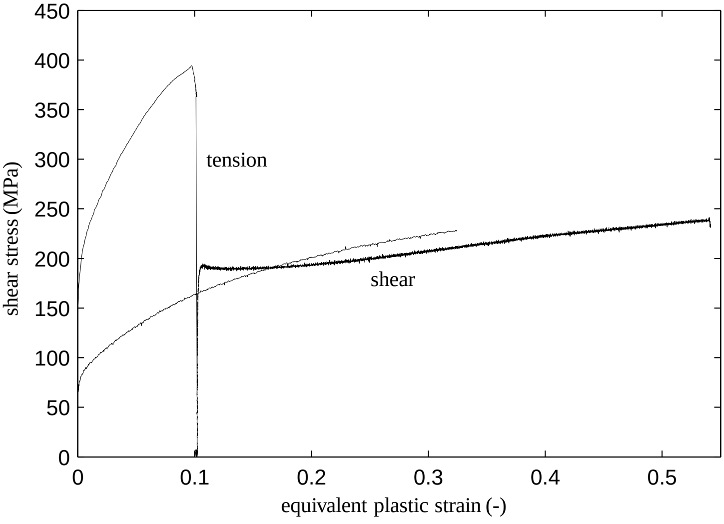

Figure 4.14: Orthogonal test with elastic unloading after the tensile deformation. The shear deformation is applied at a lower rate.

deformation was applied at $\dot{\varepsilon}_{\text{eq}} = 1 \cdot 10^{-2}\,s^{-1}$ and the shear deformation was applied at $\dot{\varepsilon}_{\text{eq}} = 5 \cdot 10^{-4}\,s^{-1}$. The result of this test is depicted in Figure 4.14. Although the amount of pre-strain is smaller in this experiment, a similar overshoot as in Figure 4.13 is observed.

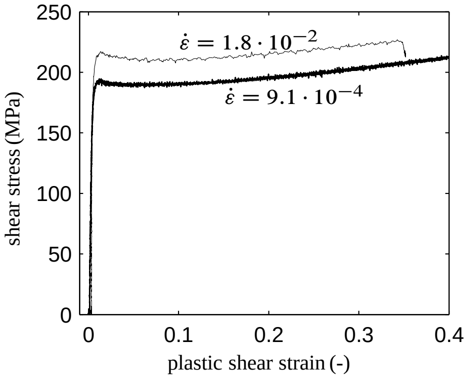

Figure 4.15: The shear curves in the orthogonal experiments with intermediate elastic unloading. Different strain rates are applied to investigate the qualitative difference.

The shear curve in this graph is measured at $\dot{\varepsilon}_{\text{eq}} = 1 \cdot 10^{-2} s^{-1}$. Because the strain rate in the experiment is lower, the shear stress is lower compared to the presented reference curve. Qualitatively, however, the curves do correspond. From this experiment it is concluded that a change in strain rate does not effect the strain path change sensitivity in DC06.

For modelling purposes it is interesting to know at what stress level the material enters the plastic regime. When the evolution of the shear stress in Figures 4.13 and 4.14 are observed, it seems as if the stress state is directly in the plastic regime. However, due to the definition of the equivalent plastic strain, Section 3.3, there is an accumulation of noise and the strain increases. A better representation for the assessment of the elastic–plastic transition is given in Figure 4.15 where the shear stress is plotted as a function of the shear strain. This figure shows that the actual elastic–plastic transition is close to the maximum of the overshoot. This is independent of the strain rate used for the shear deformation.

In Figure 4.16 the results of the orthogonal test on aluminium are depicted. In contrast with the mild steel it does not show the cross-hardening effect. In simple shear deformation, the stress state slowly converges towards the monotonic shear curve.

The experiments with orthogonal strain path changes on H340LAD are depicted in Figure 4.17. The overshoot in shear stress after the strain path change is 20 MPa compared to the reference shear curve. It is noticed that the overshoot may also be related to the abrupt elastic–plastic transition, which is clearly shown in the reference hardening curve. The monotonic shear curve shows a peak after which it drops to a plateau and only then starts to harden. Furthermore, the shear stress does not exactly converge to the reference shear curve, which is emphasised by the different hardening rates that are observed for the reference curve and for the shear stress in the experiment with an orthogonal strain path change.

The results of the experiments with an orthogonal strain path change on DP600 are depicted in Figure 4.18. The characteristic overshoot in shear stress is not observed in this experiment. The shear stress converges gradually to the monotonic shear curve. It is noticed that the pre-strain in the tensile direction is relatively small in this experiment

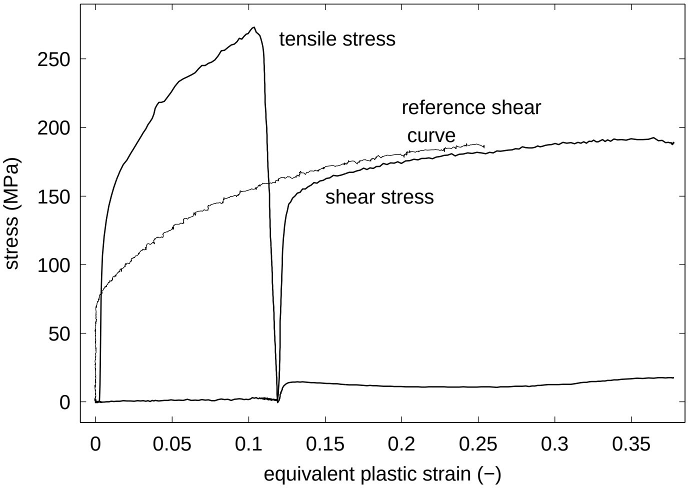

Figure 4.16: Orthogonal test on aluminium.

(7 %). The transition from the elastic to the plastic region requires approximately 2.5 % equivalent plastic strain. When compared to the cyclic experiments, the elastic–plastic transition is “sharper” in an orthogonal strain path change than in a reversed strain path change. The dislocations piled up at the LEDS are released as the deformation is reversed, but in an orthogonal strain path change, newly activated slip planes carry the deformation. This explains that the elastic–plastic transition is more abrupt in the orthogonal strain path change than in reverse loading.

4.5.2 Tracing the yield surface

The goal of this section is to investigate whether it is possible to determine the shape of the yield surface by applying a sharp strain path change from the plane strain tension deformation to the simple shear deformation. As the stress state moves from tension to shear, and the materials remains plastically loaded, the stress state has to follow the —potentially evolving— yield surface. Plastic deformation during the transition means that plastic strain is accumulated and that in turn implies hardening of the material. This effect would cause the stress state to drift away from the initial yield surface shape just before the strain path change. Experiments were performed with orthogonal strain path changes in which the strain path change is varied from a very sharp change to a gradual strain path change. The accumulated strain in the strain path change would be reflected in the changing stress paths. The algorithm to control the stiffness of the machine, see Section 3.5, was used to prescribe the strain paths. Different settings of the parameters are employed in this algorithm for the compensation of the stiffness of the machine to describe strain paths with different degrees of sharpness. DC06 and AA5182 were used to investigate the concept and the material behaviour.

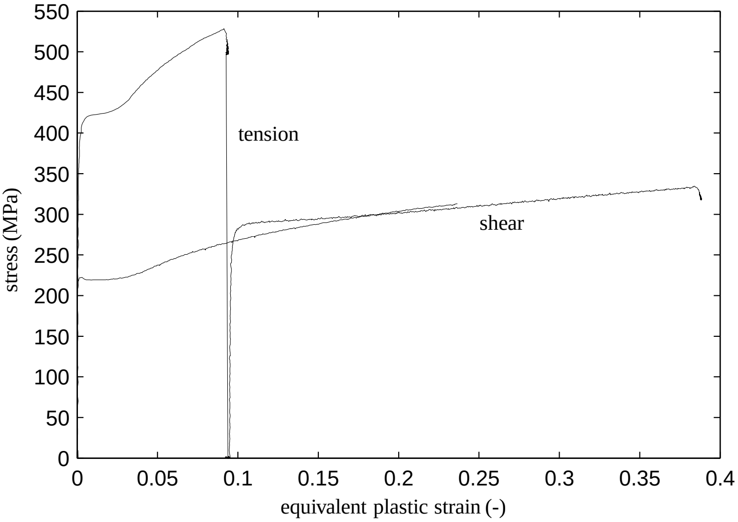

Figure 4.17: Experiment with an orthogonal strain path change on H340LAD.

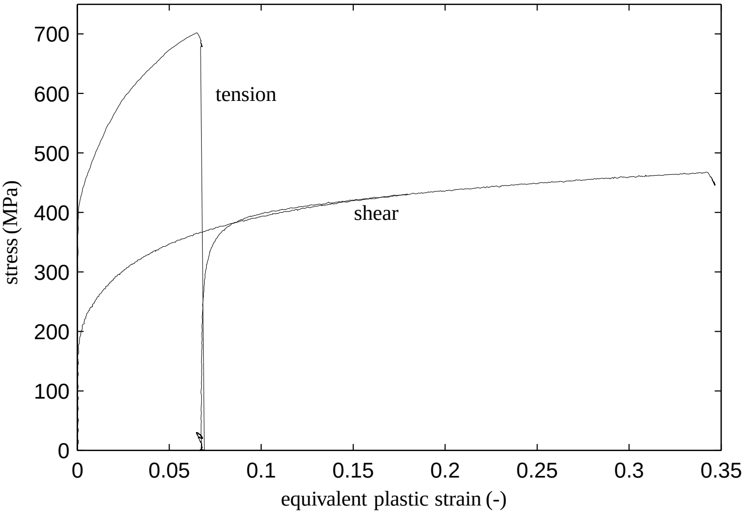

Figure 4.18: Experiment with an orthogonal strain path change on DP600.

DC06 Figure 4.19 shows the results for mild steel[1]. After the tensile deformation the actuator movement is stopped and a small decrease in tensile stress is observed. This

---

[1] The results for DC06 in this work are based on van Riel and van den Boogaard (2007)

happens within a time interval of 20 s. For test 1 to 5 the active control of the stiffness is used to steer the strain path, test 6 is done without any compensation. The smoothness of the change of the strain path is adapted, by allowing more tensile strain to develop during the shear phase, see Figure 4.19(a). For DC06 6 different experiments have been performed with different transitions from the tensile to the shear deformation. Test 1 shows the strongest strain path change and test 6 shows the most gradual strain path change. The tests 2-5 have intermediate transition modes. It is noted that the depicted strains are not plastic strains, but total strains. Here, the behaviour of the machine is clearly reflected in the experimental results. The strain paths are varied by the amount of extra tensile strain from the onset of shear deformation, from 0.5 % to 6.5 % tensile strain in the smoothest path.

The stresses observed in these experiments are depicted in Figure 4.19(b) and 4.19(c). The vertical axes show the stresses as a function of the equivalent plastic strain. For a sharp strain path change the shear stress clearly shows an overshoot during the strain path change with respect to the monotonic simple shear test. The stress response is similar to a strain path change with elastic unloading, as presented in Section 4.5.1. A slight difference is observed at the onset of shear deformation. In the experiment with intermediate elastic unloading (Figure 4.13), the stress increases with an elastic rate to the maximum shear stress, whereas in the experiment with a continuous strain path change, the stress increases more gradually. This is due to the strain that is accumulated in the shear and tensile deformation and partially because the noise accumulation appears in the experiments with continuous strain path changes.

For the test where the strain path change gradually evolves from tensile to shear, the shear stress slowly converges to the monotonic simple shear test. The intermediate curves (experiments 2-5) show responses in between these two extremes. The same holds for the stresses in the tensile direction. The test with the gradual strain path change shows a slowly decreasing tensile stress. The tests with more sharp strain path changes show a rapid decrease in tensile stress. After an additional 0.15 shear strain (Figure 4.19(c)) the effect of the strain path change is no longer observed. For a smooth transition, the tensile stress converges to a zero stress level, but this requires more strain. Figure 4.20 shows the stress curves of the 6 orthogonal tests in stress space. The 20 s delay after the tensile test manifests itself here by the peak to the right in the tensile direction, after which shear deformation continues. Test 6 is the one curve that deviates clearly from the other five experiments; during the transition from tensile to simple shear a little hardening can be observed in this test. The other five tests show almost coinciding stress paths. The inset shows a zoom of the upper left corner of the stress space. Tests 1-3 are depicted here. This shows that the tests 1 and 2 have a small decrease in shear stress which corresponds with the softening after the overshoot in Figure 4.19(c).

It is remarkable to see that despite the significant increase in plastic strain, the stress paths in stress space show similar results for tests 1-5 (Figure 4.20). Figure 4.21 shows the results of the evolution of tensile strains and the tensile stress for tests 1 and 6. Test 1 shows an increase of tensile strain during the strain path change of approximately 1 %, but test 5 increases by 5 %. It is noticed that this strain is accumulated only during the transition from tensile to simple shear deformation. The coinciding stress paths can be explained by the low hardening rate at the used pre-strains. For similar experiments with lower pre-strains

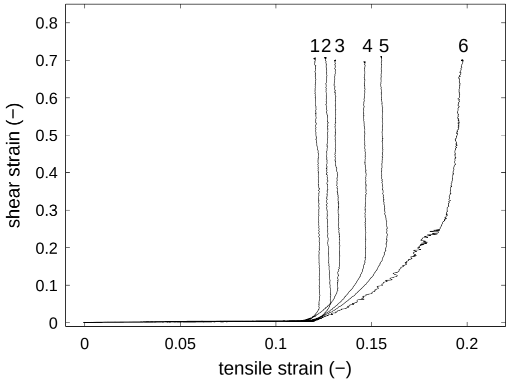

(a) Strain paths in tension–simple shear strain space.

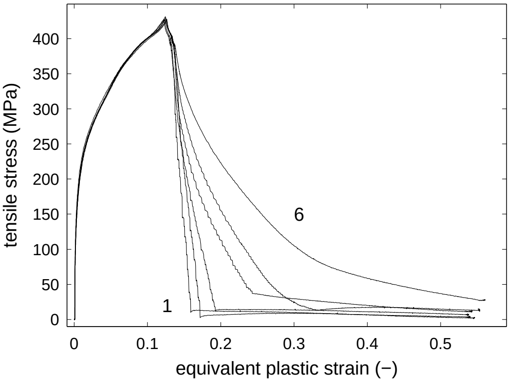

(b) The tensile stress components.

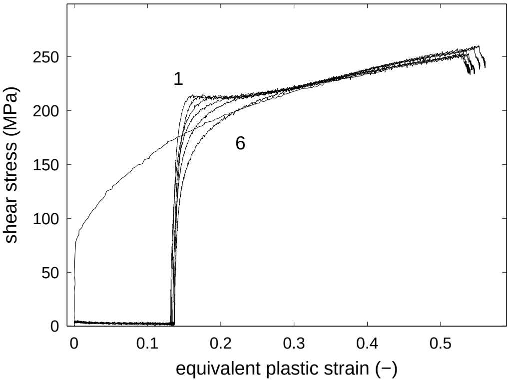

(c) The shear stress components with the monotonic shear curve.

Figure 4.19: The experiments on DC06 with continuous orthogonal strain path changes.

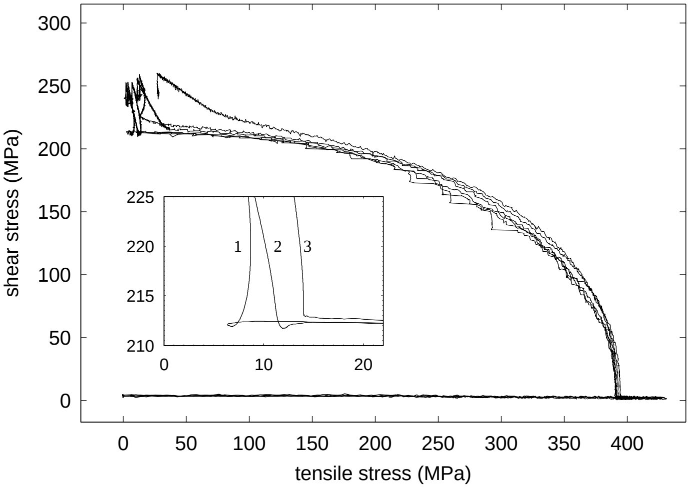

Figure 4.20: Stress paths for the DC06 material. The inset shows a zoom of the stress path indicating the place the overshoot in shear stress occurs.

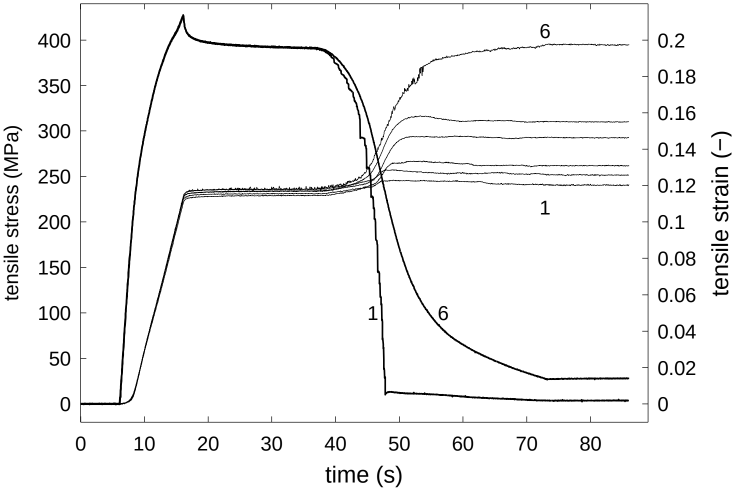

Figure 4.21: The evolution of stress and strain responses in the orthogonal tests. The thick lines represent the tensile stresses for tests 1 and 6. The thin lines represent the tensile strains, from tests 1 to 6.

it is expected that the stress paths would show more spread. Hence, an impression of the shape of the yield locus can be obtained, while some plastic strain is still permissible.

Aluminium For AA5182 similar experiments were performed, see Figure 4.22. Still, the strain paths change from very strict (test 1) to gradual (test 4). Figure 4.22(a) shows that in tests 1-3 with increasing shear deformation, the tensile strain decreases. This happens only after the strain path change and at higher shear strains. Also, the tensile stresses in these tests increase to a level of approximately $\sigma_{yy} = 20\,\mathrm{MPa}$. This is due to the shear deformation that induces a contraction of the material in the tensile direction which in turn leads to a tensile stress. The decreasing tensile strain during shear is known as the pointing effect.

The stress–strain curves show that the sharper the change of deformation direction, the more shear stress is required for the transition. Like DC06, for AA5182 it is concluded that the change of strain path is independent of elastic unloading. This is proven by test 1 and the comparison with the test with intermediate unloading in Figure 4.16.

The stress paths of these experiments are shown in Figure 4.25. Tests 1 and 2 have a good correspondence, but tests 3 and 4 show a trend away from the initial stress path. This could be due to the higher hardening rate of aluminium at the strain level of the strain path change. Only a small increase of accumulated plastic strain would result in a higher shear stress. For tracing the yield surface of this material, tests 3 and 4 cannot be used. For further experiments where the shape of the yield locus is examined, the strain path change should "use" as little accumulated plastic strain as possible and hence be as sharp as possible.

The influence of pre-strain

In this section it is experimentally investigated whether the amount of pre-strain in the plane strain tension phase of the experiment influences the stress path during the loading transition. For all the materials this was done for 3 or 4 levels of pre-strain. In the former section it was argued that the transition from plane strain tension to simple shear does not necessarily have to be sharp to reveal the shape of the yield surface. Therefore, the settings for the strain transition as used in test 2 for DC06 were applied.

The set of orthogonal experiments on DC06 is expanded with experiments with a test with a higher pre-strain, Figure 4.20. The shape of the stress path does not seem to change, only the stresses are higher. This is also true for the test with a lower pre-strain. However, at the end of the strain path change it can be seen that the stress path bends towards shear while there is still a tensile stress present. This is more evident at the experiment where the pre-strain is small, the stress state does not seem to follow the yield surface but translates towards the shear state in a linear fashion. At lower pre-strains the hardening rate is still relatively high, explaining the deviation from the yield surface. Hence, tests with a low pre-strain give an indeterminate view of the yield surface. At higher pre-strains the shape of the stress paths are similar and hence give a better impression of the yield surface.

For aluminium it was observed that the orthogonal strain path changes with intermediate unloading (Figure 4.25) are dependent on the amount of pre-strain. The hardening rate at elevated pre-strains drops, which is also reflected in the results. The experiments with higher pre-strains show a trend that is equal to the initial experiments. Furthermore, the experiments with a lower pre-strain show a deviating trend. Here, the more pronounced increase in shear stress shows the influence of the higher hardening rate.

The experiments on H340LAD, Figure 4.26, and on DP600, Figure 4.27, show similar

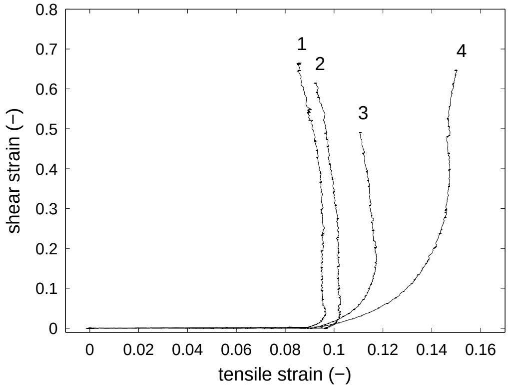

(a) Strain paths in tension–simple shear strain space.

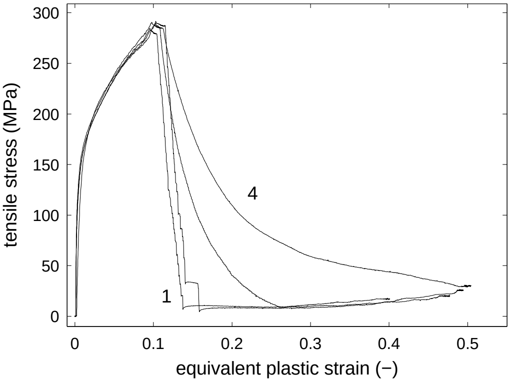

(b) The tensile stress components.

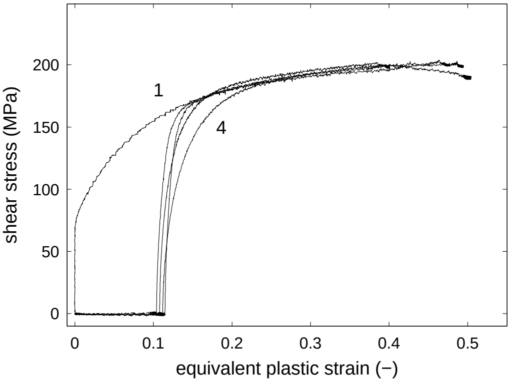

(c) The shear stress components with the monotonic shear curve.

Figure 4.22: The orthogonal test without elastic unloading for AA5182.

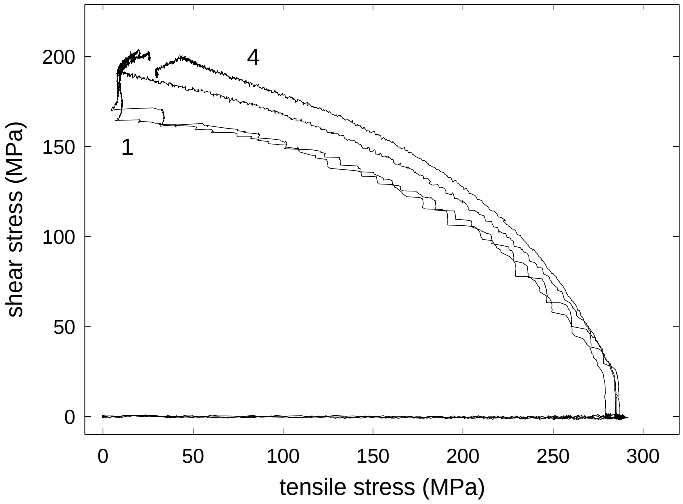

Figure 4.23: Stress paths for AA5182.

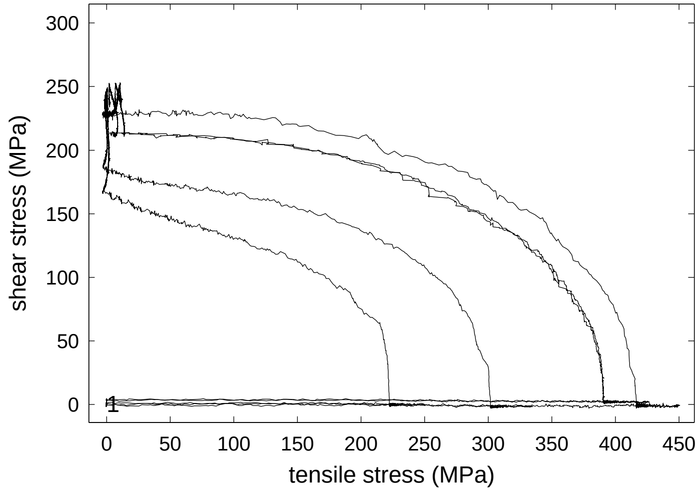

Figure 4.24: Stress paths for DC06.

trends as in AA5182. Increasing or decreasing the pre-strain does not influence the shape of the stress paths, only the size of it.

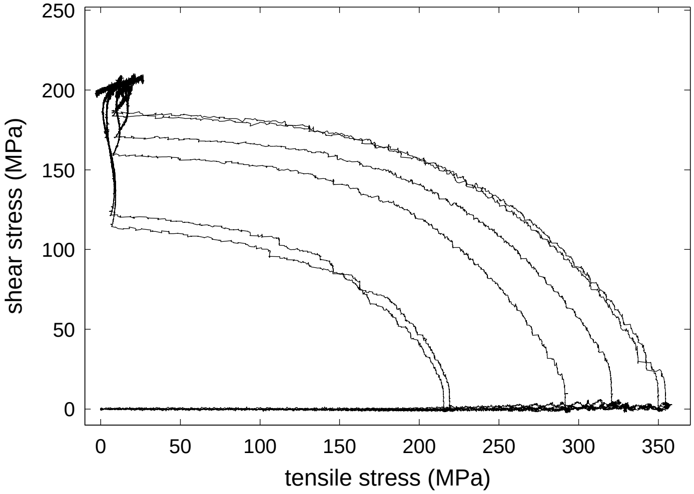

Figure 4.25: Stress paths for AA5182.

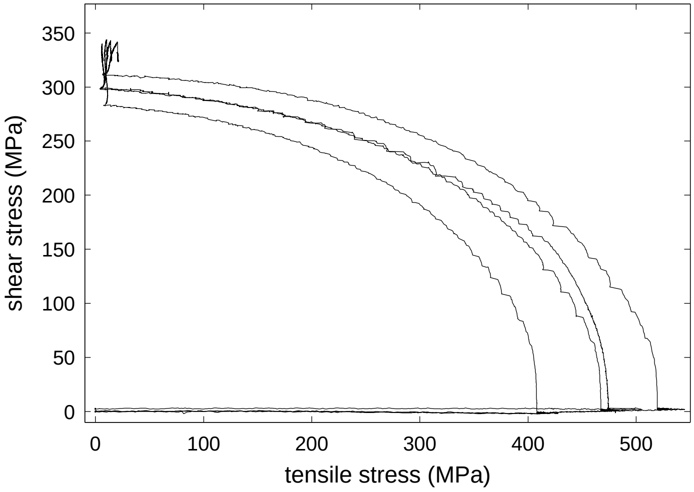

Figure 4.26: Stress paths for H340LAD.

Yield surface shape

The presented experiments in this section show a cross section of the yield surface through the plane strain tension–simple shear plane. To compare the yield surfaces from the different materials with each other, the stress paths are normalised with respect to the tensile

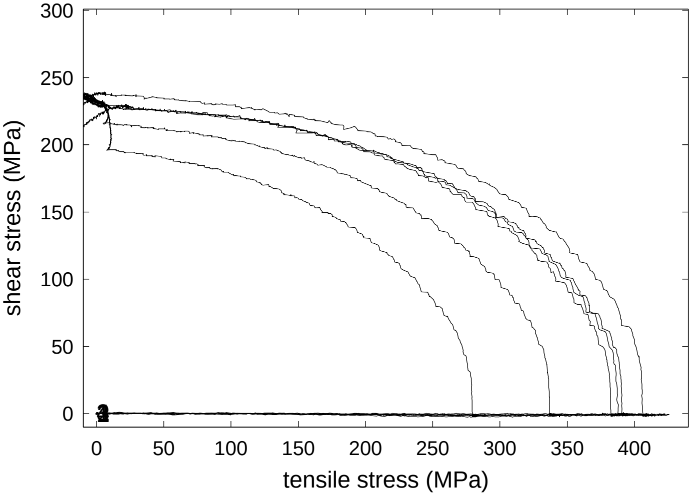

Figure 4.27: Stress paths for DP600.

stresses at the start of the strain path change. The experiments that have the largest amount of pre-strain were selected to exclude hardening during the strain path change. Figure 4.28 shows the results of the normalised stress paths for the 4 materials. There is a clear distinction between the aluminium and the other metals, especially at the onset of shearing. It is noticed that aluminium shows a small kink at the start of the strain path change, which is reproducible (see Figure 4.25), but the stress path would be more in line with the other metals if that kink was not present. The ratio of shear stress over plane strain tension is smallest for aluminium (0.53) and highest for the H340LAD (0.60). DP600 and DC06 initially follow the same stress path as H340LAD, but separate halfway. For the Von Mises yield criterion this ratio equals 0.50. All of these materials show a higher value than the Von Mises ratio, indicating that a classical isotropic hardening model based on Von Mises would not be accurate to simulate these experiments.

4.6 Conclusion

With the experiments presented in this chapter it is successfully shown that the TWENTE BIAXIAL TESTER can be used for measuring the mechanical behaviour of sheet metal during strain path changes. The possibility of the TWENTE BIAXIAL TESTER to control 2 axis of deformation, plane strain tension and simple shear, made it possible to measure the stress and strain path in experiments with changing strain paths. The influences of anisotropy and strain rate can be measured with this equipment. To make accurate comparisons between different experiments based on equivalent plastic strain, it is recommended to improve its calculation, since now noise in the measurement is accumulated in the definition of equivalent plastic strain.

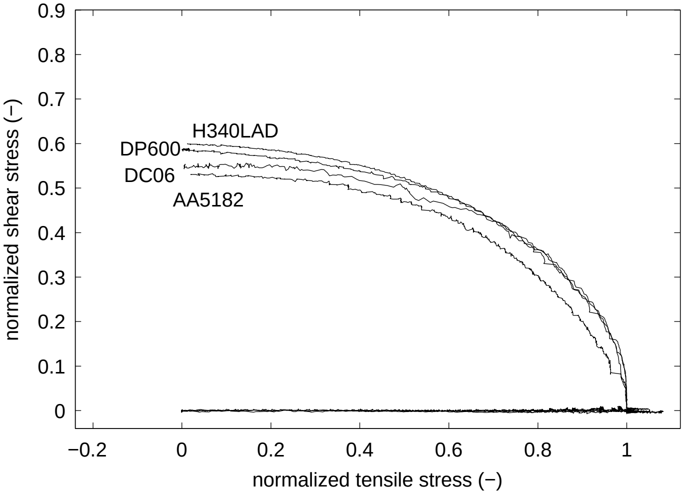

Figure 4.28: Normalized stress paths in stress space.

The measurements on DC06 showed that this material is strongly sensitive to strain path changes. Experiments on this material with orthogonal strain path changes, with and without intermediate elastic unloading, showed that the cross-hardening effect is independent of the application of intermediate unloading. However, the overshoot in stress in the experiment without unloading has more accumulated strain in the strain path change and hence, the stress peak is shifted slightly on the strain axes. It was observed that the elastic–plastic transition in the experiment with intermediate elastic unloading is higher than the reference monotonic curve for the measured amount of plastic strain. The enlarged elastic domain contributes more to the overshoot than the hardening that is observed subsequently.

The continuous orthogonal experiments on mild steel and aluminium show that if the strain path change is sufficiently sharp, the yield surface can be observed in the stress path of the experiments. The build-up of accumulated plastic strain needs to be small enough and the hardening rate should be small in order not to deviate from the yield surface. Finally, the yield surfaces that were detected show a trend away from the Von Mises yield locus, indicating that the classical isotropic hardening material model with a Von Mises yield surface cannot be applied for these experiments.

The mechanical behaviour presented in this chapter provides a good basis to fit the (strain path dependent) material models. In Chapter 6 it is shown whether the material models fitted to these experiments indeed give a better prediction of full simulation process. The next chapter discusses the material models and the results of the fitting procedure.

5. Material models for non-proportional loading

In the previous chapter, the influence of the strain path on the mechanical behaviour was examined. It showed that both the amount and the direction of deformation determine the stress–strain relation.

This chapter discusses the material models that are used to describe non-proportional deformation. These models make extensive use of differential equations to describe the state variables that determine the external stress–strain behaviour. To this end, a framework is presented that is used to solve the equations concurrently. Classical isotropic and kinematic hardening is used to show the concept. The concept is applied to two material models that are able to describe strain path dependent material behaviour. The Teodosiu & Hu model is a physically based model that describes the evolution of the micro-structure of the material, and extracts the stress–strain behaviour from it. The second model is the Levkovitch model, that describes the different aspects of strain path dependency via different superimposed models. A characteristic feature in this model is the changing shape of the yield surface during deformation. The performance of the different models is assessed by the results of the fitting procedure on DC06. This material is selected as a test case material, since it shows the most distinct strain path sensitive behaviour.

The experiments on DC06 have shown that some orthogonal strain path changes can be accurately described by classical material models. To discriminate between the strain paths that induce typical strain path sensitive behaviour and those that do not, a strain path change indicator is proposed. Implemented in a FE-code it supplies the engineer with a tool to assess the strain path changes in the material.

5.1 Classical phenomenological material models

This section describes material models that are frequently used in sheet metal forming simulations. A distinction is made between 2D and 3D material models. In the 3D-case, a full 3 -dimensional state is described; $\boldsymbol{\sigma} = \left[\sigma_x, \sigma_y, \sigma_z, \sigma_{xy}, \sigma_{yz}, \sigma_{xz}\right]^{\mathrm{T}}$. In the plane stress models it is assumed that $\sigma_z = 0$, and all components in the z-direction are eliminated: $\boldsymbol{\sigma} = \left[\sigma_x, \sigma_y, \sigma_{xy}\right]^{\mathrm{T}}$. Firstly, the anisotropic Hill'48 and Vegter yield criteria are discussed. The Hill'48 model can be seen as an extension of the Von Mises model and describes the full 3 dimensional stress state. Three mechanical experiments are required to determine the material parameters. The Vegter criterion on the other hand was developed especially for simulations of sheet metal and describes the plane stress state. It requires 10 mechanical tests, but offers greater flexibility than the Hill'48 criterion. In the following subsection it is explained how a plane stress yield criterion can be incorporated in a material model that describes the full 3 -dimensional stress state. This enhances the application of plane stress yield criteria. Next, the description for isotropic and kinematic hardening is presented. Kinematic hardening describes the shift of the yield surface through stress space, based on the direction of plastic flow. For efficiency, the material model is generally reduced to the plane stress situations. This allows a reduction of 3 directions in the calculations. It is explained that in the case of kinematic hardening, an inconsistency with the 3D situation exists. An algorithm is presented such that the consistency is preserved.

5.1.1 Yield criteria

The yield criterion describes the stress state in which a material changes from reversible, elastic mechanical behaviour to irreversible, plastic behaviour. In this work the focus is on the Hill‘48 and Vegter yield criteria. Both models assume that anisotropy is symmetric around the rolling, transverse and thickness directions. The Hill'48 is used because it is widely applied and it has a simple mathematical description. The Vegter model is more complex, but offers more freedom for accurate description of the initial yielding behaviour.

Hill yield criterion The Hill'48 criterion is given in the format of (2.1):

$$\varphi = F(\sigma_y-\sigma_z)^2+G(\sigma_z-\sigma_x)^2+H(\sigma_x-\sigma_y)^2+2L\sigma_{yz}^2+2M\sigma_{zx}^2+2N\sigma_{xy}^2-x^2 \quad (5.1)$$

The values of F, G, H, L, M and N describe the anisotropy of the material. The value of x can be scaled with the anisotropy parameters. In this work $x = \sqrt{G+H}\sigma_\mathrm{f}$ such that the uniaxial flow stress in x-direction equals the flow stress σ_f. It is computationally convenient to write the yield function as a homogeneous function of the first degree. Also introduced is the tensor **M** with the material parameters (De Borst and Feenstra, 1990):

$$\phi = \sqrt{\boldsymbol{\sigma}:\mathbf{M}:\boldsymbol{\sigma}} - \sigma_\mathrm{f} \quad (5.2)$$

The tensor **P** can be represented in matrix format:

$$[\mathbf{M}] = \frac{1}{G+H}\begin{bmatrix} G+H & -H & -G & 0 & 0 & 0 \\ -H & F+H & -F & 0 & 0 & 0 \\ -G & -F & F+G & 0 & 0 & 0 \\ 0 & 0 & 0 & 2N & 0 & 0 \\ 0 & 0 & 0 & 0 & 2M & 0 \\ 0 & 0 & 0 & 0 & 0 & 2L \end{bmatrix} \quad \text{with } \{\boldsymbol{\sigma}\} = \begin{Bmatrix} \sigma_x \\ \sigma_y \\ \sigma_z \\ \sigma_{xy} \\ \sigma_{xz} \\ \sigma_{yz} \end{Bmatrix} \quad (5.3)$$

For the set of parameters where $F = G = H = 1$ and $L = M = N = 3$ the Von Mises yield criterion is obtained.

This criterion can be easily converted to a plane stress model, *i.e.* where the thickness stress and the shear stresses out of the plane of the sheet are 0 ($\sigma_z = \sigma_{yz} = \sigma_{xz} = 0$). Hence Equation (5.1) reduces to:

$$\phi = \sqrt{(G+H)\sigma_x^2 + (H+F)\sigma_y^2 - 2H\sigma_x\sigma_y + 2N\sigma_{xy}^2} - \sqrt{G+H}\sigma_\mathrm{f} \quad (5.4)$$

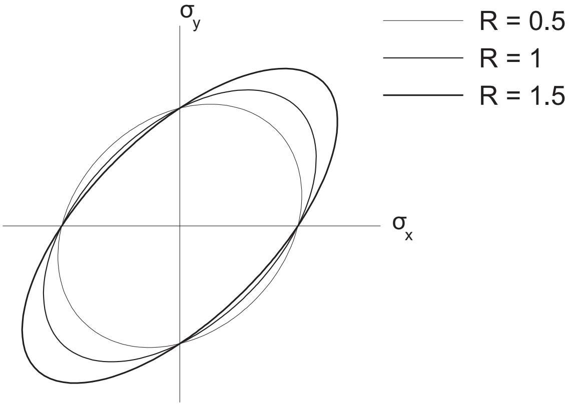

Figure 5.1: The shape of the yield locus for different values of R_0.

The R-values that are determined in tensile tests can be used to determine the parameters of the plane stress criterion:

$$F = \frac{2R_0}{R_{90}\left(1+R_0\right)} \tag{5.5}$$

$$G = \frac{2}{1+R_0} \tag{5.6}$$

$$H = 2-G \tag{5.7}$$

$$N = \frac{\left(2R_{45}+1\right)\left(R_{90}+R_0\right)}{R_{90}\left(1+R_{90}\right)} \tag{5.8}$$

Finally, Figure 5.1 shows the influence of different values for R_0 in plane stress space. With higher values for the R-value, the yield surface elongates unrealistically along the $\sigma_x = \sigma_y$ axis.

Vegter criterion The Vegter yield function (Vegter and van den Boogaard, 2006) describes a yield function based on interpolation between measured points on the yield surface. The yield function is described in the principal stress space and uses Bezier interpolation to connect the measured yield stresses in equi-biaxial, plane strain tension, uniaxial tensile and shear tests to define a yield locus, see also Figure 5.2(a). This leads to four stress points in the region where $\sigma_x > \sigma_y$. Stress situations where $\sigma_x < \sigma_y$ can be determined if the sample is rotated by 90°. Compressive stresses were not measured, but were covered by the assumption that the material initially behaves identically in tension and in compression, hence the yield locus is point symmetric around the origin.

In the experiments not only the yield stress was measured, but also the strain and its direction were determined. Drucker's postulate states that the plastic flow is perpendicular to the yield surface and this is applied to the measured strains to determine the local tangent of the yield surface. With the stress points and their tangents available, second order Bezier

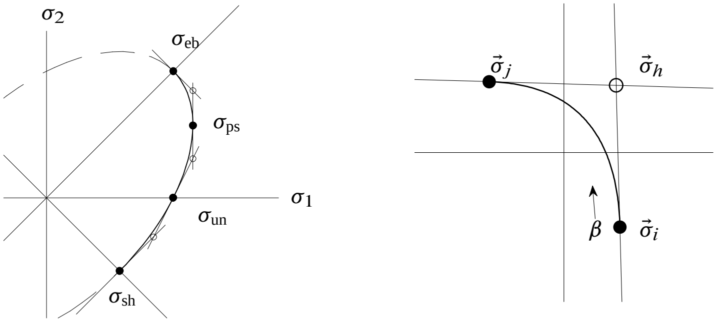

(a) The measured stresses and the hinge points.

(b) A Bezier curve.

Figure 5.2: The construction of the Vegter yield criterion.

curves can be constructed between the stress points, see Figure 5.2(b). A stress state in the 2 -dimensional stress space is represented by a vector:

$$\vec{\sigma} = \begin{Bmatrix} \sigma_1 \\ \sigma_2 \end{Bmatrix} \tag{5.9}$$

which is used in the definition of the stress state:

$$\vec{\sigma} = \frac{\sigma_{\mathrm{eq}}}{\sigma_{\mathrm{f}}} \left[\vec{\sigma}_i + 2\beta\left(\vec{\sigma}_h - \vec{\sigma}_i\right) + \beta^2\left(\vec{\sigma}_i + \vec{\sigma}_j - 2\vec{\sigma}_h\right)\right] \quad \beta \in [0,1] \tag{5.10}$$

The hinge point $\vec{\sigma}_h$ is defined by the intersection of the tangents of the 2 measured flow stresses; $\vec{\sigma}_i$ and $\vec{\sigma}_j$. The yield surface is a C^1 continuous yield function. The term between square brackets indicates the position on the yield surface via the scalar β and the ratio $\sigma_{\mathrm{eq}}/\sigma_{\mathrm{f}}$ determines the magnitude of the stresses. This definition is used in the traditional yield criterion setting, see Equation (2.1)

Anisotropy of the sheet is captured by using the flow stresses of the experiments at different angles with respect to the rolling direction. The flow stresses at intermediate angles are defined by a harmonic interpolation function.

For the implementation of this model, experiments in three directions (0°, 45° and 90°) are required to determine the 17 material parameters. A simplification was presented to decrease the number of material parameters and the number of tests, (Vegter *et al.*, 2009). This adds to the usability of the model.

5.1.2 Integrating a plane stress yield criterion in a 3D material model.

For sheet metal forming simulations, it is normally assumed that the blank is in a plane stress state. Simulations of sheet metal forming processes are sensitive to the definition of the yield criterion, and much effort has been put into the development of accurate yield descriptions. Usually, yield criteria for sheet forming are defined in 2D (Banabic *et al.*, 2004; Vegter and van den Boogaard, 2006), which allows a more simple definition than in three dimensions. However, hardening models are increasingly complex and take into account the full 3D stress state. Additionally, more advanced elements (*e.g.* solid shells), also require a full 3D stress state. Hence, a method is required to incorporate the plane stress yield criteria in a 3D material model. To this end, the stress in thickness direction and the shear stress in the plane of the sheet need to be incorporated in the definition of the equivalent stress. Based on the assumption that the yielding behaviour is independent of hydrostatic stress, a general description of a plane stress yield criterion in a 3D material model is presented.

The general definition of a yield criterion is given in Equation (2.1) and incorporates the definition of the equivalent stress. In the case of a plane stress material model the equivalent stress is given by:

$$\sigma_{\text{eq}}^{\text{ps}} = \sigma_{\text{eq}}^{\text{ps}}\left(\sigma_x, \sigma_y, \sigma_{xy}\right) \tag{5.11}$$

Obviously, $\sigma_{\text{eq}}^{\text{ps}}$ is not a function of σ_z, σ_{yz} and σ_{zx}. The goal is to eliminate these out-of-plane stresses from the stress vector in the 3D situation. Without changing the value of the equivalent stress, a hydrostatic stress with the magnitude of the stress in z-direction can be added such that the third component in $\boldsymbol{\sigma}^{3\text{D}}$ equals 0:

$$\boldsymbol{\sigma}^{3\text{D}} = \begin{Bmatrix} \sigma_x \\ \sigma_y \\ \sigma_z \\ \sigma_{yz} \\ \sigma_{zx} \\ \sigma_{xy} \end{Bmatrix} \Longrightarrow \boldsymbol{\sigma}^{3\text{D}} = \begin{Bmatrix} \sigma_x \\ \sigma_y \\ \sigma_z \\ \sigma_{yz} \\ \sigma_{zx} \\ \sigma_{xy} \end{Bmatrix} - \begin{Bmatrix} \sigma_z \\ \sigma_z \\ \sigma_z \\ 0 \\ 0 \\ 0 \end{Bmatrix} \tag{5.12}$$

The shear stresses in regular yield criteria are decoupled from the normal stresses and from the other shear stresses. This indicates that the contribution from σ_{yz} and σ_{xz} can be defined independently, based on a arbitrary 3D yield criterion. The general description of a plane stress yield criterion in a 3D stress state then reads:

$$\sigma_{\text{eq}}^{3\text{D}} = \sigma_{\text{eq}}^{3\text{D}}\left(\sigma_{\text{eq}}^{\text{ps}}\left(\boldsymbol{\sigma}^{\text{ps}}\right), \sigma_{xz}, \sigma_{yz}\right) \qquad \text{with} \qquad \boldsymbol{\sigma}^{\text{ps}} = \begin{Bmatrix} \sigma_x - \sigma_z \\ \sigma_y - \sigma_z \\ \sigma_{xy} \end{Bmatrix} \tag{5.13}$$

in which $\sigma_{\text{eq}}^{\text{ps}}$ is the plane stress definition of the yield criterion and $\sigma_{\text{eq}}^{3\text{D}}$ is a 3D yield criterion from which only the shear contributions are used.

For the use of Equation (5.13) in a material model, the derivatives of $\sigma_{\text{eq}}^{3\text{D}}$ with respect to the stresses are required. Because all stresses except σ_z are explicitly calculated in Equation (5.13), these derivatives are easily determined. The derivative with respect to σ_z needs to be determined in some other way, because this component is not explicitly included in the definition of $\sigma_{\text{eq}}^{3\text{D}}$. From the assumption that the yield criterion is independent of the hydrostatic stress, it follows that the derivative of the $\sigma_{\text{eq}}^{3\text{D}}$ is in the deviatoric plane. Hence,

$$\frac{\partial\phi}{\partial\sigma_x}^{3\text{D}} + \frac{\partial\phi}{\partial\sigma_y}^{3\text{D}} + \frac{\partial\phi}{\partial\sigma_z}^{3\text{D}} = 0 \qquad \Longleftrightarrow \qquad \frac{\partial\phi}{\partial\sigma_z}^{3\text{D}} = -\left(\frac{\partial\phi}{\partial\sigma_x}^{3\text{D}} + \frac{\partial\phi}{\partial\sigma_y}^{3\text{D}}\right) \tag{5.14}$$

The new yield criterion is generic with respect to the applied plane stress yield criterion and shows the same convergence in the return mapping algorithm as the plane stress yield criterion.

To show the concept of a plane stress yield criterion in a 3D yield function, the Von Mises criterion is used. The general description of this yield function for three dimensions description is:

$$\sigma_{\mathrm{vM}}^{3\mathrm{D}} = \sqrt{\sigma_x^2 + \sigma_y^2 + \sigma_z^2 - \sigma_x\sigma_y - \sigma_y\sigma_z - \sigma_x\sigma_z + 3\sigma_{xy}^2 + 3\sigma_{yz}^2 + 3\sigma_{zx}^2} \tag{5.15}$$

When a plane stress situation is described, the yield criterion reduces to:

$$\sigma_{\mathrm{vM}}^{\mathrm{ps}}\left(\boldsymbol{\sigma}^{\mathrm{ps}}\right) = \sqrt{\sigma_x^2 + \sigma_y^2 - \sigma_x\sigma_y + 3\sigma_{xy}^2} \tag{5.16}$$

The plane stress definition is implemented in the 3D yield function according Equation (5.13):

$$\sigma_{\mathrm{vM}}^{3\mathrm{D}}\left(\boldsymbol{\sigma}^{3\mathrm{D}}\right) = \sqrt{{\sigma_{\mathrm{vM}}^{\mathrm{ps}}}^2\left(\sigma_x - \sigma_z, \sigma_y - \sigma_z, \sigma_{xy}\right) + 3\sigma_{yz}^2 + 3\sigma_{zx}^2} \tag{5.17}$$

Now, the desired plane stress yield condition replaces $\sigma_{\mathrm{vM}}^{\mathrm{ps}}$, such that a full 3D yield criterion is obtained based on the chosen plane stress yield criterion.

5.1.3 Isotropic and kinematic hardening models.

The evolution of the flow stress during deformation can be modelled either phenomenologically, or based on the evolution of the micro-structure. This latter class of material models takes into account dislocation storage, and often uses multiple state variables to describe the history of deformation (van Liempt, 1994; Roters *et al.*, 2000; Nes and Marthinsen, 2002). Here, we limit ourselves to phenomenological material models, because of their ease of use and their efficiency in FE simulations. The general description of a yield function is presented in Equation (2.1).

An often used isotropic hardening law is the Swift law:

$$\sigma_{\mathrm{f}} = C\left(\varepsilon + \varepsilon_0\right)^n \tag{5.18}$$

It requires only 3 parameters and can easily be fitted to a uniaxial tensile test. The Bauschinger effect, observed in cyclic tests (Section 4.4), cannot be modelled with isotropic hardening models. To this end kinematic hardening models were developed that shift the yield surface in stress space, while the size of the yield surface remains constant. Upon a load reversal, the material yields earlier compared to the isotropic model, hereby describing the Bauschinger effect in a load reversal. The direction of the shift is either in the direction of the plastic flow (Prager assumption) or in the direction of the stress rate (Ziegler assumption). If a Von Mises yield criterion is used these directions are equal. The yield surface can only move in the deviatoric plane. In kinematic hardening models the history of the stress path is stored in the back stress and it is therefore necessary that the evolution equations of this group are rate-type equations. The Armstrong–Frederick kinematic hardening is often used to describe the Bauschinger effect:

$$\dot{\boldsymbol{\alpha}} = \dot{\lambda}\left(\mathbf{A}_{\mathrm{k}}\frac{\partial\phi}{\partial\boldsymbol{\sigma}} - A_{\mathrm{l}}\,\boldsymbol{\alpha}\right) \tag{5.19}$$

$\mathbf{A}_\mathrm{k}$ describes the hardening rate. The evolution of the back stress is dependent on the amount of pre-strain via the second term on the right hand side. The material parameter A_l controls the contribution of the pre-strain. It allows for a gradual increase in flow stress after the load reversal and mimics the the transient hardening effect after a load reversal. The direction of the evolution is determined by the direction of plastic flow $\partial\phi/\partial\boldsymbol{\sigma}$. This model can be improved by simply defining a set of these laws in one kinematic hardening law (Chaboche, 1991; Chun *et al.*, 2002):

$$\dot{\boldsymbol{\alpha}} = \sum_{i=1}^{n} \dot{\lambda} \left(\mathbf{A}_\mathrm{k}^i \frac{\partial\phi}{\partial\boldsymbol{\sigma}} - A_\mathrm{l}^i \, \boldsymbol{\alpha}^i \right) \tag{5.20}$$

It was demonstrated that this model gives accurate results for a loading history with 10 load reversals (Chaboche, 1991).

The kinematic hardening model presented here can describe the transient hardening effect in cyclic loading, but not the work hardening stagnation. To constrain the evolution of the back stress after a load reversal, and hereby mimic the work hardening stagnation, a bounding surface can be introduced into the model. It evolves in the direction of the plastic flow, but at a lower rate than the back stress. After a load reversal, the back stress is constrained by the bounding surface, but after some monotonic deformation, the bounding surface again develops in the current deformation direction. This allows the back stress to evolve further (Huétink, 1991; Yoshida and Uemori, 2002, 2003). These models are not used in this work, but may be valuable in simulations of processes dominated by load reversals.

5.1.4 Kinematic hardening in the plane stress formulation

In sheet metal forming simulations, the stress development in the thickness direction is normally ignored because the stress in this direction is approximately zero. In full 3-dimensional material models, the strain in the thickness direction is iteratively changed to find the plane stress situation. By implementing the plane stress boundary condition directly in the material model, the iterations on the plane stress conditions are avoided, resulting in a time efficient algorithm compared to the full 3D algorithm. Another reason for the use of plane stress material models is that yield criteria are developed specifically for plane stress situations, since this is less complicated then developing a yield criterion in 3D. A plane stress material model is derived from a 3D material model by simply eliminating the thickness components from the algorithm. In this section it is investigated whether such a conversion from the 3D material model to the plane stress material model is consistent[1]. Classical material models are based on (combinations of) isotropic and kinematic hardening laws. A 3D material model with only isotropic hardening can be consistently converted to a plane stress algorithm, by eliminating the z-direction and adapting the elasticity-matrix, as is illustrated in many textbooks (Chen, 1994; Zienkiewicz and Taylor, 2005). For kinematic hardening models, however, it is shown that the thickness direction cannot be simply eliminated. The back stress in the z-direction needs to be taken into account to give consistent results. Even for yield criteria that are only defined in plane stress, a compensation is

---

[1] This work was presented in van Riel and van den Boogaard (2007)

required. It is noted that the yield functions do not need to be adapted themselves, because the compensation acts on the return mapping algorithm itself.

Figure 5.3 illustrates the difference between the a plane stress and 3D material model. The direction of plastic flow in a uniaxial test in a 3D material model is oriented within the deviatoric plane. The plastic flow in a uniaxial tensile loading has components in the plane of the sheet (x and y), but also in the thickness (z) direction (Figure 5.3(a)). A plane stress material model employs the yield surface without a component in the thickness direction, as it is represented in Figure 5.3(b). The direction of plastic flow lies within the plane of plane stress and does not have a component in the z-direction. The major difference between a plane stress algorithm and a 3D material model is the missing z-component in the plane stress material model.

A 3D material model with isotropic hardening is consistently converted to a plane stress algorithm by eliminating the thickness components from the algorithm. The missing z-components do not affect the overall stress state or the convergence of the material model. This makes sense because isotropic hardening is independent of the direction of plastic flow. Kinematic hardening, however, is dependent on the direction of plastic flow. A comparison is presented in Figure 5.4 between a kinematic hardening model based on the plane stress algorithm and a 3D material model that is iteratively solved for the plane stress situation. Again, the uniaxial tensile test (in x-direction) is employed with the Von Mises yield criterion. Figure 5.4(b) shows the consequence of the different plastic flow directions. The yield surface in the 3D material model shifts in stress space parallel to the x-axis, hereby preserving the uniaxial tensile stress state. The back stress evolution in the 3D material model includes a component in the z-direction. But because the plane stress situation is required:

$$\sigma_z = \zeta_z + \alpha_z = 0 \qquad \Longrightarrow \qquad \zeta_z = -\alpha_z \tag{5.21}$$

In other words a hydrostatic stress is added to $\boldsymbol{\zeta}$ such that $\zeta_z = -\alpha_z$ and $\sigma_z = 0$. The stress state moves along the hydrostatic axis to the plane of the plane stress state. The position of the stress state on the yield surface remains at the uniaxial stress point, because only

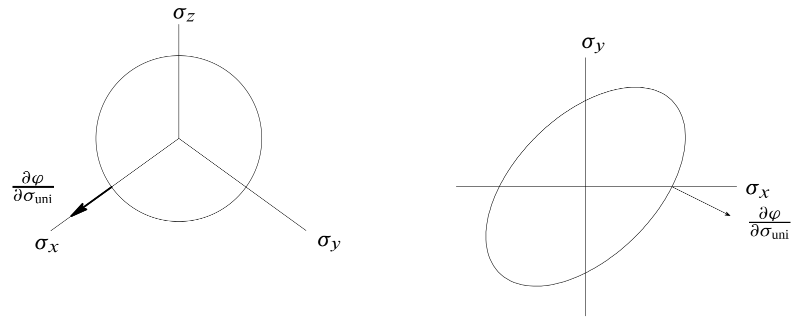

(a) The deviatoric plane in 3D stress space.

(b) The plane stress situation.

Figure 5.3: The Von Mises yield surface and the direction of plastic flow in a uniaxial tensile test in the x-direction.

a change in the hydrostatic stress is applied. For the evolution of the back stress in the plane stress algorithm, the representation in Figure 5.3(b) is applied. Because there are no out-of-plane components, there is also no evolution of stresses in the thickness direction ($\sigma_z = \zeta_z = \alpha_z = 0$). The direction of plastic flow points “down” in Figure 5.3(b), and thus the yield surface shifts in that direction. At the same time, the uniaxial stress state requires that $\sigma_y = 0$, leading to a shift of the stress state over the yield surface to the plane strain point in Figure 5.4(b). The larger contribution of hydrostatic stress in the 3D material model leads to a higher tensile stress compared to the plane stress algorithm.

To arrive at a situation where the plane stress and 3D algorithm are consistent, α_z and ζ_z have to be taken into account in the plane stress algorithm. By including the effective stress ζ_z in the definition of the equivalent stress, in the direction of plastic flow, a consistent conversion is obtained:

$$\sigma_{\text{eq}} = \sigma_{\text{eq}}\left(\zeta_x, \zeta_y, \zeta_z, \zeta_{xy}\right) \qquad \text{and} \qquad \frac{\partial\phi}{\partial\boldsymbol{\sigma}} = \frac{\partial\phi}{\partial\boldsymbol{\sigma}}\left(\zeta_x, \zeta_y, \zeta_z, \zeta_{xy}\right) \tag{5.22}$$

The value of ζ_z is easily determined because $\boldsymbol{\alpha}$ evolves according to the direction of plastic flow, which lies in the deviatoric plane. Hence, $\boldsymbol{\alpha}$ is also deviatoric and thus together with Equation (5.21) we obtain:

$$\alpha_z = -\left(\alpha_x + \alpha_y\right) \qquad \Longrightarrow \qquad \zeta_z = -\alpha_z = \left(\alpha_x + \alpha_y\right) \tag{5.23}$$

The rest of the material model remains the same, only Equations (5.22) and (5.23) need to be implemented. It is emphasised that ζ_z and α_z are only used to determine the consistent values in the x- and y-directions for $\boldsymbol{\zeta}$ and $\partial\varphi/\partial\boldsymbol{\sigma}$.

It is recognised that the yield criteria defined for sheet metal forming are often plane stress models that do not include the required z-component. These models show the same deviation in the stress evolution and therefore require the adaptation. Because the yield criterion is independent of hydrostatic pressure, the method from Section 5.1.2 can be applied. Equation (5.22) can be used in plane stress yield criteria by eliminating the ζ_z

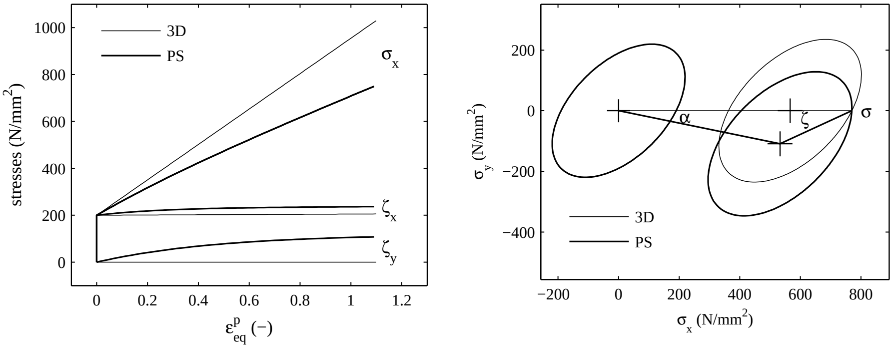

(a) Stresses as a function of the equivalent plastic strain.

(b) The shift of the yield surfaces for the two algorithms.

Figure 5.4: The resulting stresses in a uniaxial test and the positions in stress space.

component. Again, this is done by adding a hydrostatic stress to the normal components, such that the z-component equals 0:

$$\boldsymbol{\zeta} = \left\{ \begin{array}{c} \zeta_x - \zeta_z \\ \zeta_y - \zeta_z \\ \zeta_z - \zeta_z \\ \zeta_{xy} \end{array} \right\} \implies \boldsymbol{\zeta}^* = \left\{ \begin{array}{c} \zeta_x - \zeta_z \\ \zeta_y - \zeta_z \\ \zeta_{xy} \end{array} \right\} \implies \sigma_{\text{eq}} = \sigma_{\text{eq}}\left(\boldsymbol{\zeta}^*\right), \quad \frac{\partial \phi}{\partial \boldsymbol{\sigma}} = \frac{\partial \phi}{\partial \boldsymbol{\sigma}}\left(\boldsymbol{\zeta}^*\right) \tag{5.24}$$

This compensation allows for a consistent conversion from the 3D material model to the plane stress model, even with a plane stress yield function.

5.2 Generic return mapping algorithm

For the implementation of a material model in a Finite Element code, a stress update algorithm and the consistent stiffness are required. In this section a generic algorithm is presented that is used both for the stress update and to calculate the stiffness matrix. This model describes isotropic and kinematic hardening.

5.2.1 Stress update

This section describes the algorithm to determine the stress after a strain increment. The algorithm maps the stress back to the yield surface, explaining its name: *return mapping algorithm*. A set of three differential equations will be used to determine the evolution of three state variables:

$$\left\{\Delta \mathbf{V}\right\} = \left\{ \begin{array}{c} \Delta \boldsymbol{\sigma} \\ \Delta \boldsymbol{\alpha} \\ \Delta \lambda \end{array} \right\} \tag{5.25}$$

The equations are solved with the Euler-backward procedure. Hence, the equations are evaluated with the state variables at the end of the load step. The general update for the state variables in this procedure is evaluated as $\mathbf{V}_{n+1} = \mathbf{V}_n + \Delta \mathbf{V}$, where n denotes the number of the load step. The yield criterion is evaluated in terms of the effective stress $\boldsymbol{\zeta}$ and the equivalent plastic strain at the end of the load step:

$$\phi = \sigma_{\text{eq}}\left(\boldsymbol{\zeta}_{n+1}\right) - \sigma_{\text{f}}\left(\varepsilon_{\text{eq}\,n+1}\right) \tag{5.26}$$

Through discretisation of Equation (2.5), the plastic strain increment depends on the derivative of the yield surface at the end of the load step:

$$\Delta \boldsymbol{\varepsilon}^{\text{p}} = \Delta \lambda \left. \frac{\partial \phi}{\partial \boldsymbol{\sigma}} \right|_{n+1} \tag{5.27}$$

The stress increment is evaluated by Hooke's law:

$$\Delta \boldsymbol{\sigma} = \mathbf{E} : \Delta \boldsymbol{\varepsilon}^{\text{e}} \tag{5.28}$$

The externally applied strain is split in to an elastic part and a plastic part:

$$\Delta \boldsymbol{\varepsilon} = \Delta \boldsymbol{\varepsilon}^{\text{e}} + \Delta \boldsymbol{\varepsilon}^{\text{p}} \tag{5.29}$$

Equations (5.28) and (5.27) are combined with (5.29) to give the following evolution in terms of strain:

$$\Delta\boldsymbol{\varepsilon} = \mathbf{E}^{-1}\Delta\boldsymbol{\sigma} + \Delta\lambda\left.\frac{\partial\phi}{\partial\boldsymbol{\sigma}}\right|_{n+1} \tag{5.30}$$

Kinematic hardening, to describe cyclic behaviour, is included via the Armstrong–Frederick law from (5.19):

$$\Delta\boldsymbol{\alpha} = \left(\mathbf{A}_\mathrm{k}\left.\frac{\partial\phi}{\partial\boldsymbol{\sigma}}\right|_{n+1} - A_\mathrm{l}\boldsymbol{\alpha}_{n+1}\right)\Delta\lambda \tag{5.31}$$

To solve the above set of equations, they are cast in to a set of three residual functions:

$$\mathbf{R}_\sigma = \Delta\boldsymbol{\varepsilon} - \mathbf{E}^{-1}\Delta\boldsymbol{\sigma} - \Delta\lambda\left.\frac{\partial\phi}{\partial\boldsymbol{\sigma}}\right|_{n+1} \tag{5.32}$$

$$\mathbf{R}_\alpha = -\mathbf{A}_\mathrm{k}^{-1}\left(\mathbf{I} + A_\mathrm{l}\,\Delta\lambda\right)\Delta\boldsymbol{\alpha} - \mathbf{A}_\mathrm{k}^{-1}A_\mathrm{l}\,\Delta\lambda\,\boldsymbol{\alpha}_n + \left.\frac{\partial\phi}{\partial\boldsymbol{\sigma}}\right|_{n+1}\Delta\lambda \tag{5.33}$$

$$R_\phi = -\left(\sigma_\mathrm{eq} - \sigma_\mathrm{f}\right) \tag{5.34}$$

R_ϕ is adapted with a minus sign to obtain symmetry in the Jacobian. The 3 residual functions are combined to $\mathbf{R} = \left[\mathbf{R}_\sigma, \mathbf{R}_\alpha, R_\phi\right]^\mathrm{T}$. All the evolution equations are met when $\mathbf{R} = \mathbf{0}$, but the functions are nonlinear and require an iterative procedure to find $\mathbf{V}^{\mathrm{n+1}}$. A Taylor series expansion is used, which is evaluated as:

$$\mathbf{R}\left(\Delta\mathbf{V}^{i+1}\right) = \mathbf{0} = \mathbf{R}\left(\Delta\mathbf{V}^{i}\right) + \frac{\partial\mathbf{R}}{\partial\mathbf{V}^i} : \mathrm{d}\mathbf{V}^i \tag{5.35}$$

$$\Longrightarrow \mathrm{d}\mathbf{V}^i = -\left(\frac{\partial\mathbf{R}}{\partial\mathbf{V}^i}\right)^{-1} : \mathbf{R}\left(\Delta\mathbf{V}^i\right) \tag{5.36}$$

The derivative of the residual functions are used to construct the Jacobian of this set of equations. Note that that because $\boldsymbol{\sigma} = \boldsymbol{\zeta} - \boldsymbol{\alpha}$, the derivatives of the yield function can be interchanged easily:

$$\frac{\partial\phi}{\partial\boldsymbol{\sigma}} = \frac{\partial\phi}{\partial\boldsymbol{\zeta}} = -\frac{\partial\phi}{\partial\boldsymbol{\alpha}} \quad\text{and}\quad \frac{\partial^2\phi}{\partial\boldsymbol{\sigma}^2} = \frac{\partial^2\phi}{\partial\boldsymbol{\zeta}^2} = \frac{\partial^2\phi}{\partial\boldsymbol{\alpha}^2} = -\frac{\partial^2\phi}{\partial\boldsymbol{\sigma}\,\partial\boldsymbol{\alpha}} \tag{5.37}$$

These properties are used to determine the Jacobian of the set of the residual functions:

$$[\mathbf{J}] = \begin{bmatrix} \mathbf{E}^{-1} + \Delta\lambda\dfrac{\partial^2\phi}{\partial\boldsymbol{\sigma}^2}_{n+1} & \Delta\lambda\dfrac{\partial^2\phi}{\partial\boldsymbol{\sigma}\,\partial\boldsymbol{\alpha}}_{n+1} & \dfrac{\partial\phi}{\partial\boldsymbol{\sigma}}_{n+1} \\ -\Delta\lambda\dfrac{\partial^2\phi}{\partial\boldsymbol{\sigma}^2}_{n+1} & \mathbf{A}_\mathrm{k}^{-1}\left(1 + \Delta\lambda\,A_\mathrm{l}\right) - \Delta\lambda\dfrac{\partial^2\phi}{\partial\boldsymbol{\sigma}\,\partial\boldsymbol{\alpha}}_{n+1} & A_\mathrm{l}\,\mathbf{A}_\mathrm{k}^{-1}\boldsymbol{\alpha}_{n+1} - \dfrac{\partial\phi}{\partial\boldsymbol{\sigma}}_{n+1} \\ \dfrac{\partial\phi}{\partial\boldsymbol{\sigma}}^\mathrm{T}_{n+1} & \dfrac{\partial\phi}{\partial\boldsymbol{\alpha}}^\mathrm{T}_{n+1} & \dfrac{\partial\phi}{\partial\lambda}_{n+1} \end{bmatrix} \tag{5.38}$$

The obtained matrix is almost symmetric, apart from the contribution in J(2,3). The first term in this entry causes a non-symmetric matrix. Only when linear hardening is assumed

```
input: $\Delta\boldsymbol{\varepsilon}$

$\boldsymbol{\sigma}^{\mathrm{tr}} = \boldsymbol{\sigma}_n + \mathbf{E}\Delta\boldsymbol{\varepsilon}$
$\phi = -\left(\sigma_{\mathrm{eq}}(\boldsymbol{\sigma}^{\mathrm{tr}}) - \sigma_{\mathrm{f}}\right)$

if $\phi > 0$
    elastic step: $\boldsymbol{\sigma} = \boldsymbol{\sigma}^{\mathrm{tr}}$
                  $\Delta\lambda = 0$
                  $\Delta\varepsilon_{\mathrm{eq}}^{\mathrm{p}} = 0$
else
    plastic step
        $\Longrightarrow$ RMA:
        $R_\phi = \phi$
        do $|\mathbf{R}| > \delta_t$
            Determine $\sigma_{\mathrm{eq}}$, $\frac{\partial\phi}{\partial\boldsymbol{\sigma}}$, $\frac{\partial\phi}{\partial\boldsymbol{\alpha}}$, $\frac{\partial\phi^2}{\partial\boldsymbol{\sigma}^2}$, $\frac{\partial\phi^2}{\partial\boldsymbol{\sigma}^2}$ and $\frac{\partial\phi^2}{\partial\boldsymbol{\sigma}\partial\boldsymbol{\alpha}}$ with $\boldsymbol{\sigma}$
            Determine $\sigma_{\mathrm{f}}$, $\frac{\partial\phi}{\partial\sigma_{\mathrm{f}}}$, $\frac{\partial\sigma_{\mathrm{f}}}{\partial\varepsilon_{\mathrm{eq}}^{\mathrm{p}}}$, $\frac{\partial\varepsilon_{\mathrm{eq}}^{\mathrm{p}}}{\partial\lambda}$ with $\varepsilon_{\mathrm{eq}}^{\mathrm{p}}$
            calculate the residual vector: $\{\mathbf{R}\}$
            calculate the Jacobian $[\mathbf{J}]$
            Determine the increment $\{\delta\mathbf{V}\} = [\mathbf{J}]^{-1}\{\mathbf{R}\}$
            and from $\Delta\mathbf{V}^{i+1} = \Delta\mathbf{V}^{i} + \delta\mathbf{V}$
            update $\boldsymbol{\sigma}$, $\boldsymbol{\alpha}$, $\lambda$ and $\varepsilon_{\mathrm{eq}}^{\mathrm{p}}$
        end do
end if

update $\boldsymbol{\sigma}$, $\lambda$ and $\varepsilon_{\mathrm{eq}}^{\mathrm{p}}$
```

Figure 5.5: Iteration scheme for the return mapping algorithm.

($A_1 = 0$), the Jacobian is symmetric. This Newton–Raphson system converges quadratically in the neighbourhood of the solution.

The algorithm presented here is generic in the sense that it is not dependent on the chosen yield locus and isotropic hardening law. However, the applied kinematic hardening model is an explicit function within this RMA. Another type of kinematic hardening requires adaptation of Equations (5.34) and (5.38). To implement the yield locus definition, the first and second derivatives with respect to the stress are required. For the isotropic hardening law, only a function evaluation and the derivative with respect to the equivalent plastic strain is required. This considerably increases the flexibility of the algorithm.

Figure 5.5 shows schematically the loop that describes the RMA. The input consists of a new strain increment $\Delta\boldsymbol{\varepsilon}$. A trial stress ($\boldsymbol{\sigma}^{\mathrm{tr}}$) is determined by assuming that the total strain increment is elastic. This assumption is checked with the yield criterion. If the load increment is indeed elastic, the final stress equals the trial stress. If the material deforms plastically, the return mapping algorithm is entered and the residual functions are used to find the updated values for $\boldsymbol{\sigma}$, $\boldsymbol{\alpha}$ and $\varepsilon^{\mathrm{p}}_{\mathrm{eq}}$. When the norm of $\mathbf{R}$ is smaller than a prescribed tolerance δ_t, the solution is found.

5.2.2 Stiffness matrix

At the global level of the FE simulation, the material stiffness at the integration points is required. The local stiffnesses are then assembled to a complete stiffness of the structure. For the small strain theory that is used here, the stiffness needs to be determined in terms of:

$$\mathbf{K} = \left.\frac{\mathrm{d}\boldsymbol{\sigma}}{\mathrm{d}\boldsymbol{\varepsilon}}\right|_{n+1} \tag{5.39}$$

The derivative can be obtained via the RMA determined in the stress update procedure. Equation (5.36) is used to determine the stress, but it is expressed in terms of strains. A perturbation method is used to determine the stiffness:

$$\left[\quad \frac{\partial \mathbf{R}}{\partial \mathbf{V}^i} \quad \right] \left\{ \begin{matrix} \mathrm{d}\boldsymbol{\sigma} \\ \mathrm{d}\boldsymbol{\alpha} \\ \mathrm{d}\lambda \end{matrix} \right\} = \left\{ \begin{matrix} \mathrm{d}\boldsymbol{\varepsilon} \\ 0 \\ 0 \end{matrix} \right\} \tag{5.40}$$

From this set of equations the desired relation can be isolated. This can be done in terms of every individual matrix component, but it is more straightforward to isolate only the four submatrices of the complete Jacobian:

$$\left[\begin{array}{c|cc} \mathbf{K}_{11} & \mathbf{K}_{12} & \cdots \\ \hline \mathbf{K}_{21} & \mathbf{K}_{22} & \cdots \\ \vdots & \vdots & \ddots \end{array} \right] \left\{ \begin{matrix} \mathrm{d}\boldsymbol{\sigma} \\ \mathrm{d}\boldsymbol{\alpha} \\ \mathrm{d}\lambda \end{matrix} \right\} = \left\{ \begin{matrix} \mathrm{d}\boldsymbol{\varepsilon} \\ \mathbf{0} \\ \mathbf{0} \end{matrix} \right\} \tag{5.41}$$

The stiffness matrix is easily calculate from this:

$$\frac{\partial \boldsymbol{\sigma}}{\partial \boldsymbol{\varepsilon}} = \left(\mathbf{K}_{11} - \mathbf{K}_{12} \mathbf{K}_{22}^{-1} \mathbf{K}_{21} \right)^{-1} \tag{5.42}$$

Again, this relation is established independently of the chosen yield surface and the isotropic hardening law.

Both for the return mapping algorithm as for the consistent stiffness matrix, dedicated algorithms were developed. Importantly, the combination of the Von Mises yield locus and linear isotropic/kinematic hardening can be evaluated explicitly, even for an Euler backward algorithm. Besides, the Von Mises model offers advantages because of its favourable mathematical description. The concept presented here does not have that advantage, but does have the benefit of flexibility and generality. Additionally, this concept can be used for any material model that is evaluated in this manner.

5.2.3 Application to DC06

This subsection discusses the application of the generic return mapping algorithm to the experimental results of DC06. The monotonic, cyclic and orthogonal experiments were

Table 5.1: The R-values for DC06.

R_0	R_{45}	R_{90}
1.85	2.06	2.51

simulated using the generic return mapping algorithm. The Hill'48 material model was used, with the R-values as presented in Table 5.1. In the following, isotropic and combined isotropic/kinematic hardening models are used.

Figure 5.6 shows the results of the monotonic experiments for the plane strain tension tests (in RD and TD), and the simple shear experiment. The equivalent stress–strain curves were determined by the Hill'48 yield criterion and the R-values from Table 5.1. In the first 5 % of strain, the three hardening curves correspond. The plane strain tensile tests show good agreement for the entire length of the hardening curve. The shear test on the other hand shows a deviation that increases slightly with additional strain. Due to the rotation in the material, other slip planes are activated, leading to a different hardening behaviour. The concept of equivalent stress and strain appears to be invalid for higher strains.

The experiments were additionally used to determine the material parameters for the Swift law in an isotropic hardening model with the Hill'48 yield criterion. In the fitting procedure, an objective function is defined that describes the accumulated stress difference

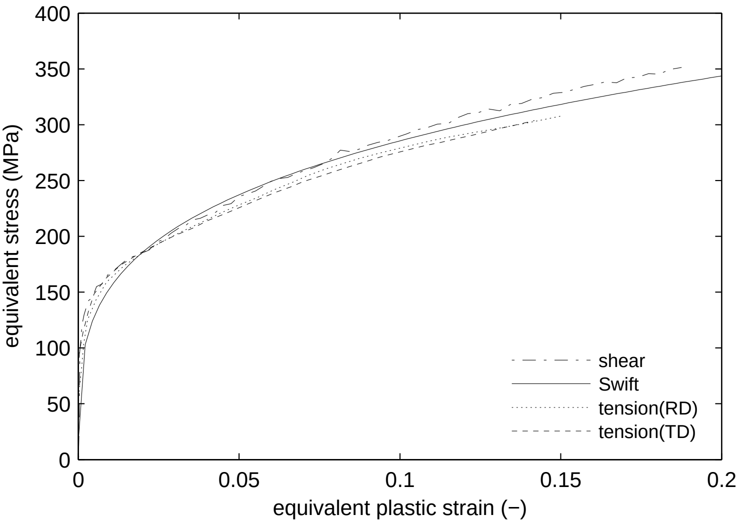

Figure 5.6: Results for the monotonic experiments and the Swift law in equivalent stress–strain space.

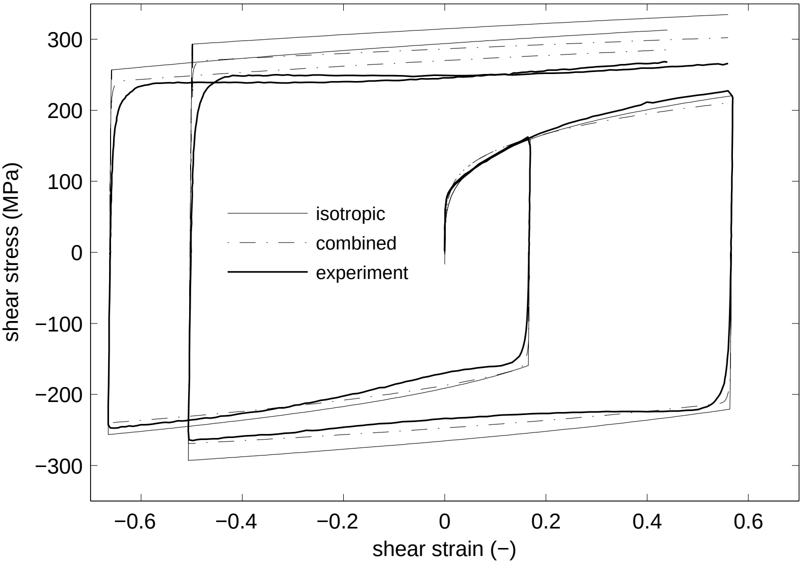

Figure 5.7: The prediction of the classical hardening models in the cyclic tests.

between the simulations of the experiments and the experimental results. The least squares method was used to determine the material parameters. To prevent the plane strain tension tests prevailing in the fitting procedure, more weight was attributed from the shear test to the objective function. The final result is shown in Figure 5.6 and the parameters can be found in Table A.3.

To describe the mechanical behaviour in cyclic loading, the kinematic hardening models were developed. The generic return mapping algorithm was used with Armstrong–Frederick kinematic hardening and isotropic hardening according to Swift. This is denoted as the “combined” model. The experiments from Figure 4.5 and the two plane strain tensile tests were used in the fitting procedure. The monotonic simple shear experiment is not included since the cyclic experiments already describe the initial monotonic hardening in simple shear. Figure 5.7 shows 2 cyclic experiments on DC06 and the results of the models with isotropic and combined hardening. In the pre-strain phase, the material models perform similarly, although both underestimate the stress at the end of the first stroke. After the first load reversal the models are initially not far off, but the deviation increases as deformation continues. Neither of these models were able to capture the work hardening stagnation, but the combined hardening model describes the experiments better. In particular, the experiment with a large pre-strain shows that an isotropic material model cannot describe cyclic loading, due to the large Bauschinger effect. The combined model shows a better performance, but the prediction after the second load reversal is still not satisfactory.

The performance of the isotropic and combined hardening model was additionally assessed with the experiments constituting an orthogonal strain path change, see Figure 4.13.

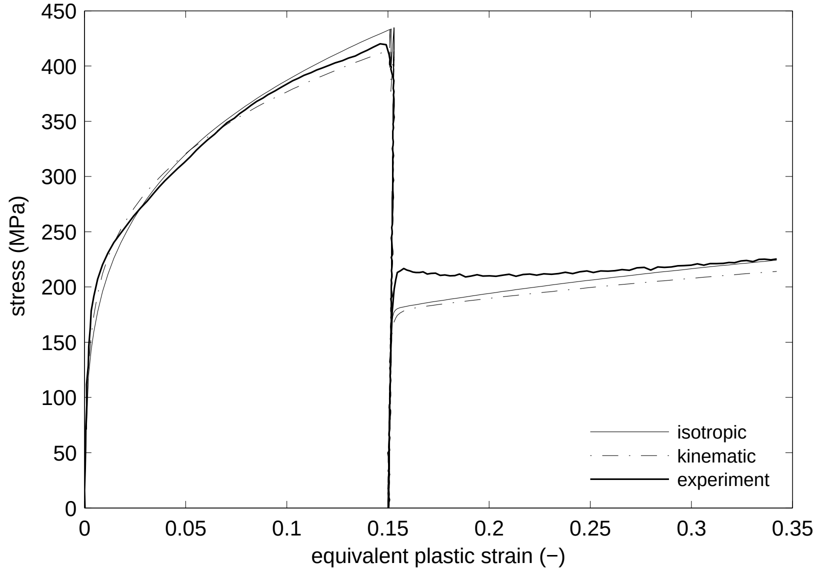

Figure 5.8: The prediction of the classical hardening models in the orthogonal test with unloading.

The results of the simulations are presented in Figure 5.8. The initial plane strain tension is accurately described, but the subsequent shear stress after the strain path change is not captured. The prediction of the combined hardening model of the shear stress is lower than the prediction of the isotropic hardening model. In the combined model, the hardening is divided over a contribution to the shift of the yield surface and a “growth” of the yield surface. If more hardening is attributed to the shift of the yield surface, size of the yield surface will remain smaller. Upon an orthogonal strain path change, the flow stress in the new direction will be lower than the flow stress predicted by the isotropic model. Hence, a combined model gives by definition a poor description of the mechanical behaviour in an orthogonal strain path change. After some more shear deformation, the simulation results coincide again with the experiments, but the characteristics of the mechanical behaviour cannot be captured with these models.

From the experiments investigated here, it is concluded that the monotonic hardening behaviour is well described by both the isotropic and the combined hardening model. The prediction of cyclic behaviour with the kinematic description is better than the isotropic model, but it is still not satisfactory. The simulation of the orthogonal experiment shows that neither model can describe the characteristic overshoot after the strain path change.

5.3 The Teodosiu & Hu model

To describe the strain path dependent mechanical behaviour in sheet metal (see Chapter 4), Teodosiu and co-workers (Teodosiu and Hu, 1995; Teodosiu, 2005; Uenishi and Teodosiu, 2004; Uenishi *et al.*, 2005) developed an extensive material model. The philosophy behind this model is that the specific strain path dependent mechanical behaviour is caused by the patterning of the dislocation structure. Via this approach the model is able to describe the Bauschinger effect; the transient hardening and the work hardening stagnation after a load reversal. And in particular, the characteristic overshoot in stress after an orthogonal strain path change can be described.

Firstly, the structure of the Teodosiu & Hu model is presented. Phenomenological models are used to describe the evolution of the different aspects of the micro-structure. In the next subsection, the implementation of the evolution equations in the framework of Section 5.2 is discussed. Finally, results of the fitting procedure on DC06 are presented.

5.3.1 Description of the model

The main component in this model is the 4th order tensor **S** that describes the influence of the micro-structure on the mechanical behaviour. It describes the build up and breakdown of LEDS and its polarity, microbands and the cellular structure. Still, in its essence, this material model is a combined isotropic/kinematic hardening model where the parameters that were determined in Section 5.2 become functions of the strain history. The dislocation structure contributes to the strain path dependent behaviour via the back stress evolution. If an orthogonal load path is applied, the back stress will increase rapidly to mimic the overshoot, and in a load reversal the evolution of the back stress is such that the Bauschinger effect, the transient hardening and the work hardening stagnation is described. Depending on the loading direction, the different components in **S** contribute to the total strength of **S**.

The evolution of the strength of the dislocation structure **S** is a function of the polarity of the LEDS. It is denoted with the second order tensor **P** and describes, depending on the loading direction, the pile-ups of dislocations on the LEDS. **P** controls the Bauschinger effect in a load reversal. For a well-annealed material, all the initial values of **S** and **P** are equal to **0**.

At a macro level, kinematic and isotropic hardening are described. The kinematic hardening evolution is completely dependent on the strength of the dislocation sheets. The isotropic hardening is dependent on the strength of the dislocation sheets, but the cellular structure, indicated by R, also contributes to the isotropic hardening. R is completely separated from the evolution of the other internal state variables.

A disadvantage of the model is the high number of material parameters (13) that are required to describe the evolution of the internal state variables. To determine the material parameters, monotonic, cyclic and orthogonal experiments are required. For materials that show limited strain path sensitive behaviour, some of the internal state variables can be assumed equal to 0. This leads to a reduction in the number of material parameters that need to be determined (Haddadi *et al.*, 2006). Strain rate sensitivity was added to the isotropic hardening model (Uenishi and Teodosiu, 2004), but the evolution of the kinematic hardening remains rate independent.

Yield stress and yield function

In the Teodosiu & Hu model, the classical yield function is employed, Equation (2.1). The flow stress is written as:

$$\sigma_{\mathrm{f}} = \tau_0 + R + m \, \|\mathbf{S}\| \tag{5.43}$$

Where τ_0 is the initial yield stress, R describes the isotropic hardening due to the cellular dislocation structure and the last term describes the isotropic hardening due to the strength of the dislocation sheets. The influence of S is distributed across the isotropic and kinematic hardening via the material parameter m.

Kinematic hardening is employed via the effective stress in the calculation of the equivalent stress, as in Equation (2.6). The evolution of the back stress is modelled by an Armstrong–Frederick-like saturation law:

$$\dot{\boldsymbol{\alpha}} = C_\alpha \left(\alpha_{\mathrm{s}} \mathbf{N} - \boldsymbol{\alpha} \right) \dot{\lambda} \tag{5.44}$$

where C_α is a material parameter that defines the saturation rate. The saturation value of the back stress is defined by α_{s}, which is not a material parameter, but an internal variable. It is defined in the next section. The back stress develops in the direction of the normalised gradient of the yield function:

$$\mathbf{N} = \frac{\frac{\partial \phi}{\partial \boldsymbol{\sigma}}}{\left\| \frac{\partial \phi}{\partial \boldsymbol{\sigma}} \right\|} \tag{5.45}$$

Strength of the dislocation structure

The strength of the dislocation structure is described using the internal state variables; the tensor **S** and the scalar R. The pile-ups of the dislocations at either sides of the LEDS is described by the polarity **P**, which is a state variable. Upon a deformation reversal, the dislocations are released from their position and are able to migrate to the cell interiors. The evolution equation reads:

$$\dot{\mathbf{P}} = C_{\mathrm{p}} \left(\mathbf{N} - \mathbf{P} \right) \dot{\lambda} \tag{5.46}$$

The polarity converges to the current loading direction **N**, with the saturation rate C_{p}. For a well-annealed material, the initial values of **S**, **P** and R are zero.

The tensor **S** is divided into two parts; a part that contains the strength in the present direction of deformation and a part that contains the strength of the latent structure, S_{D} and the tensor $\mathbf{S}_{\mathrm{L}}$, respectively. S_{D} is a scalar value because it represents solely the strength in the current loading direction:

$$S_{\mathrm{D}} = \mathbf{N} : \mathbf{S} : \mathbf{N} \tag{5.47}$$

The latent strength of the dislocation structure is determined by subtracting the directional part from **S**:

$$\mathbf{S} = \mathbf{S}_{\mathrm{D}} + \mathbf{S}_{\mathrm{L}} \quad \Longrightarrow \quad \mathbf{S}_{\mathrm{L}} = \mathbf{S} - S_{\mathrm{D}} \mathbf{N} \otimes \mathbf{N} \tag{5.48}$$

If the decomposition into two orthogonal components is based on a normalised tensor, this allows the use of an additional equation:

$$\|\mathbf{S}\|^2 = S_{\mathrm{D}}^2 + \|\mathbf{S}_{\mathrm{L}}\|^2 \tag{5.49}$$

In the following, the evolution of the state variables in the Teodosiu & Hu model is presented. Here, the directional and the latent parts of the dislocation structure are considered as individual state variables. The evolution equation for $\mathbf{S}_\mathrm{L}$ reads:

$$\dot{\mathbf{S}}_\mathrm{L} = -C_\mathrm{l}\left(\frac{\|\mathbf{S}_\mathrm{L}\|}{S_\mathrm{s}}\right)^{n_\mathrm{l}} \mathbf{S}_\mathrm{L}\dot{\lambda} \tag{5.50}$$

The term between brackets incorporates the influence of the amount of pre-strain. C_l describes the saturation rate of $\mathbf{S}_\mathrm{L}$. Initially, $\mathbf{S}_\mathrm{L} = \mathbf{0}$ and according to the evolution equation it cannot increase. Indeed, during monotonic loading, $\mathbf{S}_\mathrm{L}$ remains zero. After a strain path change however, a new decomposition is made between the directional S_D and the latent $\mathbf{S}_\mathrm{L}$ part, based on the new loading direction $\mathbf{N}$.

The evolution of the strength of the dislocation sheets is calculated by the individual evolution of the directional and latent parts of the tensor $\mathbf{S}$. In Section 5.3.2 this will be discussed more thoroughly. The evolution equation for the strength in the current loading direction is described using:

$$\dot{S}_\mathrm{D} = C_\mathrm{d}\left(h_\mathrm{P}\left(S_\mathrm{s} - S_\mathrm{D}\right) - h_\alpha S_\mathrm{D}\right)\dot{\lambda} \tag{5.51}$$

Where the parameters C_d and S_s denote the saturation rate and the saturation value, respectively. To complement Equation (5.51), the contribution of the kinematic hardening is introduced via:

$$h_\alpha = \frac{1}{2}\left(1 - \frac{\boldsymbol{\alpha} : \mathbf{N}}{\alpha_\mathrm{s}}\right) \tag{5.52}$$

The range of h_α is $(0, 1)$, depending on the loading scenario. For monotonic loading, $(\boldsymbol{\alpha} : \mathbf{N})/\alpha_\mathrm{s}$ will converge to 1, hence $h_\alpha = 0$. This will speed up the evolution of S_D in Equation (5.51). For orthogonal loading $h_\alpha \rightarrow \frac{1}{2}$ and for reverse loading $h_\alpha \rightarrow 1$. For reverse and orthogonal loading, the development of S_D is decreased. The reverse loading results in the largest stagnation. The saturation value for the back stress α_s in Equation (5.52) is a function of the dislocation structure:

$$\alpha_\mathrm{s} = \alpha_0 + (1 - m)\sqrt{S_\mathrm{D}^2 + r\,\|\mathbf{S}_\mathrm{L}\|^2} \tag{5.53}$$

In this equation, α_0 is a material parameter that denotes the initial saturation value for the back stress. The material parameter m defines the division of the contribution of $\|\mathbf{S}\|$ to the isotropic hardening Equation (5.43), or to the kinematic hardening Equation (5.53). In the last equation, the definition of $\|\mathbf{S}\|$ is adapted by the parameter r to describe the stress–strain relation in an orthogonal strain path change.

In the load step directly after an orthogonal strain path change, the decomposition of $\mathbf{S}$ into S_D and $\mathbf{S}_\mathrm{L}$ changes. The decomposition is made based on the current loading direction via Equation (5.47). Notice that $\mathbf{S}$ itself does not change. If $r > 1$, the contribution of the latent dislocation structure exceeds the contribution from S_D before the strain path change. This results in a sudden increase in α_s, and hence in a rapid build-up of kinematic stress in the new loading direction. This effect mimics the overshoot observed in the experiments. Next, $\mathbf{S}_\mathrm{L}$ decreases via Equation (5.50) and the stress curve will coincide again with the regular hardening curve.

The value of h_{P} is determined by the following function:

$$h_{\mathrm{P}} = \begin{cases} 1 - \dfrac{C_{\mathrm{p}}}{C_{\mathrm{d}} - C_{\mathrm{p}}} \left\| \dfrac{S_{\mathrm{D}}}{S_{\mathrm{s}}} - \mathbf{P} : \mathbf{N} \right\| & \text{if} \quad \mathbf{P} : \mathbf{N} \geq 0 \\ (1 + \mathbf{P} : \mathbf{N})^{n_{\mathrm{p}}} \left[1 - \dfrac{C_{\mathrm{p}}}{C_{\mathrm{d}} - C_{\mathrm{p}}} \dfrac{S_{\mathrm{D}}}{S_{\mathrm{s}}} \right] & \text{if} \quad \mathbf{P} : \mathbf{N} < 0 \end{cases} \tag{5.54}$$

This function is continuous in $\mathbf{P} : \mathbf{N}$ and is used to mimic the mechanical behaviour after a load reversal. With increasing monotonic loading, $\mathbf{P} : \mathbf{N} \to 1$, $S_{\mathrm{D}} \to S_{\mathrm{s}}$ and h_{P} converges to 1. This leads to the maximum contribution of $(S_{\mathrm{s}} - S_{\mathrm{D}})$ to $\dot{S}_{\mathrm{D}}$ in Equation (5.51). Upon a load reversal, $\mathbf{P} : \mathbf{N} \to -1$. The contribution of the polarity to S_{D} will stop because $h_{\mathrm{P}} \to 0$. Additionally, because $h_{\alpha} = 1$ in a load reversal, S_{D} will decrease.

The isotropic hardening due to the cellular structure is described with the variable R. It is not dependent on the strain rate direction, only on the equivalent plastic strain rate:

$$\dot{R} = C_{\mathrm{r}} \left(R_{\mathrm{s}} - R \right) \dot{\lambda} \tag{5.55}$$

The isotropic hardening converges to the saturation value R_{s} by the saturation rate C_{r}. This equation is equal to a Voce relation. It is noticed that this hardening law can easily be substituted by any other hardening model that is a function of $\varepsilon_{\mathrm{eq}}$.

The Teodosiu & Hu model requires the following 13 material parameters: S_{s}, C_{d}, C_{l},C_{α}, α_0, C_r, R_{s}, C_{p}, n_{p}, n_{l}, r, τ_0 and m.

5.3.2 Implementation

This section describes how the Teodosiu & Hu model can be implemented in the framework of the generic return mapping algorithm. In total, 7 residual functions are used to update all the state variables in the model: $\boldsymbol{\sigma}$, $\boldsymbol{\alpha}$, S_{D}, $\mathbf{S}_{\mathrm{L}}$, $\mathbf{P}$, R and λ. The model initially proposed by Teodosiu and Hu (1995) is not conclusive on the evolution of the strength of the dislocation structure $\mathbf{S}$, a proper decomposition of $\mathbf{S}$ in $\mathbf{S}_{\mathrm{L}}$ and S_{D} was ambiguous. In this section a method is proposed that leads to an algorithm that realistically describes the evolution of $\mathbf{S}_{\mathrm{L}}$ and S_{D}.

The decomposition of S

The approach followed to determine the generic return mapping is followed here to derive a stress update for the Teodosiu & Hu model. The Euler backward method is applied and a Newton–Raphson procedure is used to determine the state variables at the end of a load increment. An essential feature of the discretisation of the model is that the strength of the dislocation structure $\mathbf{S}^n$ is decomposed into $\mathbf{S}^n_{\mathrm{L}}$ and S^n_{D} at the *start* of a load increment. The Euler backward method prescribes that the update of the state variables is done, based on the direction of plastic flow at the *end* of the increment:

$$\begin{aligned} S^n_{\mathrm{D}} &= \mathbf{N}^{n+1} : \mathbf{S}^n : \mathbf{N}^{n+1} \\ \mathbf{S}^n_{\mathrm{L}} &= \mathbf{S}^n - S^n_{\mathrm{D}} \mathbf{N}^{n+1} \otimes \mathbf{N}^{n+1} \end{aligned}$$

Within the stress update, S_{D}^{n} and $\mathbf{S}_{\mathrm{L}}^{n}$ are considered as initial values, but they are still variable, since they depend on $\mathbf{N}^{n+1}$ which on its turn is dependent on the stress state at the end of the increment. After the decomposition, S_{D}^{n} and $\mathbf{S}_{\mathrm{L}}^{n}$ are increased with their respective increments:

$$\begin{aligned} S_{\mathrm{D}}^{n+1} &= \mathbf{N}^{n+1} : \mathbf{S}^{n} : \mathbf{N}^{n+1} + \Delta S_{\mathrm{D}} \\ \mathbf{S}_{\mathrm{L}}^{n+1} &= \mathbf{S}^{n} - S_{\mathrm{D}}^{n}\mathbf{N}^{n+1} \otimes \mathbf{N}^{n+1} + \Delta \mathbf{S}_{\mathrm{L}} \end{aligned}$$

The strength of the complete dislocation structure is then evaluated as:

$$\mathbf{S}^{n+1} = S_{\mathrm{D}}^{n+1}\mathbf{N}^{n+1} \otimes \mathbf{N}^{n+1} + \mathbf{S}_{\mathrm{L}}^{n+1} \tag{5.56}$$

It is noticed that Wang *et al.* (2008) have rewritten the incremental equations in a proper rate form. The method introduced here does not differ effectively from their work.

The return mapping algorithm

In the former section it was explained that during the load increment, the direction of plastic flow remains constant. The incremental form of the Equation (5.50) then reads:

$$\Delta \mathbf{S}_{\mathrm{L}} = -C_{\mathrm{l}} \left(\frac{\|\mathbf{S}_{\mathrm{L}}^{n+1}\|}{S_{\mathrm{s}}} \right)^{n_{\mathrm{l}}} \mathbf{S}_{\mathrm{L}}^{n+1} \Delta\lambda \tag{5.57}$$

It can be seen in this equation that every component of $\Delta \mathbf{S}_{\mathrm{L}}$ is proportional to the components of $\mathbf{S}_{\mathrm{L}}^{n+1}$. Hence, the incremental increase of $\mathbf{S}_{\mathrm{L}}$ can be written as:

$$\Delta \mathbf{S}_{\mathrm{L}} = \epsilon \, \mathbf{S}_{\mathrm{L}}^{n} \tag{5.58}$$

Thus, in the return mapping algorithm, only ϵ needs to be determined which is more efficient than iterating for every single component. Substitution in to Equation (5.57) yields:

$$\epsilon = -C_{\mathrm{l}}\Delta\lambda \left(\frac{\|(1+\epsilon)\,\mathbf{S}_{\mathrm{L}}^{0}\|}{S_{\mathrm{s}}} \right)^{n_{\mathrm{l}}} (1+\epsilon) \tag{5.59}$$

The residual functions for the stress, the back stress and the plastic multiplier are equal to the residual functions in the generic return mapping algorithm. The complete set of equations that need to be solved in the Teodosiu & Hu model are presented in Equations (5.61) to (5.67). To determine the state variables at the end of every load increment, the same procedure as in Section 5.2 is applied. The set of state variables that are determined are:

$$\{\mathbf{V}\} = \begin{Bmatrix} \Delta\boldsymbol{\sigma} \\ \Delta\boldsymbol{\alpha} \\ \Delta S_{\mathrm{D}} \\ \Delta\epsilon \\ \Delta\mathbf{P} \\ \Delta R \\ \Delta\lambda \end{Bmatrix} \tag{5.60}$$

The stress, back stress and the plastic multiplier are described by similar equations as the classical hardening laws. For S_{D}, $\mathbf{S}_{\mathrm{l}}$, $\mathbf{P}$ and R the evolution equations (5.51), (5.59), (5.46) and (5.55), respectively.

The following equations show the residual functions. The subscripts denoting the i-th iteration and the subscripts denoting the load steps are omitted where possible, to enhance readability:

$$\mathbf{R}_{\varepsilon} = \Delta\boldsymbol{\varepsilon} - \mathbf{E}^{-1}\Delta\boldsymbol{\sigma} - \Delta\lambda \left.\frac{\partial\phi}{\partial\boldsymbol{\sigma}}\right|_{n+1} \tag{5.61}$$

$$\mathbf{R}_{\alpha} = \Delta\boldsymbol{\alpha}\,(1 + \Delta\lambda\, C_{\alpha}) - C_{\alpha}\,(\alpha_{\mathrm{s}}\mathbf{N} - \boldsymbol{\alpha}_n)\,\Delta\lambda \tag{5.62}$$

$$\mathbf{R}_{S_{\mathrm{D}}} = \Delta S_{\mathrm{D}} - C_{\mathrm{d}}\left(h_{\mathrm{P}}\left(S_{\mathrm{S}} - S_{\mathrm{D}}^{n} - \Delta S_{\mathrm{D}}\right) - h_{\alpha}\left(S_{\mathrm{D}}^{n} + \Delta S_{\mathrm{D}}\right)\right)\Delta\lambda \tag{5.63}$$

$$\mathbf{R}_{S_{\mathrm{L}}} = \epsilon + C_{\mathrm{l}}\left(\frac{\sqrt{1+\epsilon}\,\left\|\mathbf{S}_{\mathrm{L}}^{0}\right\|}{S_{\mathrm{S}}}\right)^{n_{\mathrm{l}}}(1+\epsilon)\,\Delta\lambda \tag{5.64}$$

$$\mathbf{R}_{\mathrm{P}} = \Delta\mathbf{P}\left(1 + C_{\mathrm{p}}\,\Delta\lambda\right) - C_{\mathrm{p}}\,(\mathbf{N} - \mathbf{P}_n)\,\Delta\lambda \tag{5.65}$$

$$\mathbf{R}_{\mathrm{R}} = \Delta R\,(1 + C_{\mathrm{r}}\,\Delta\lambda) - C_{\mathrm{r}}\,(R_{\mathrm{s}} - R_n)\,\Delta\lambda \tag{5.66}$$

$$\mathbf{R}_{\phi} = -\left(\sigma_{\mathrm{eq}} - \left(\tau_0 + R_{n+1} + m\left\|\mathbf{S}^{n+1}\right\|\right)\right) \tag{5.67}$$

This set of residual functions gives, with the correct Jacobian, quadratic convergence in the stress update.

5.3.3 Application to DC06

In this section the parameters of the Teodosiu & Hu model are fitted to the DC06. The Hill'48 yield criterion is used in the optimisation procedure. Monotonic, cyclic and orthogonal experiments were used in the MATLAB routine `lsqcurvefit` to determine the material parameters. The routine constitutes a least squares optimisation method, in which all the experiments are used simultaneously. The model is fitted to the following 9 experiments: plane strain tension test in transverse direction; three cyclic tests in simple shear with different pre-strains (Figure 4.5); an orthogonal test with unloading (Figure 4.13) and four orthogonal experiments without unloading (tests 1-4 in Figure 4.19).

The objective function in this procedure is the difference between the measured stress–strain curves and the simulated stress–strain curves. The MATLAB routine minimises the squares of the differences. The experimental and simulated curves are divided over 325 data points. Because of the coupling of all the equations in the model, the material parameters need to be determined concurrently. To assure a good description of the typical strain path dependent behaviour by the material model, some parts of the stress curves are granted additional weight in the objective function. The stresses in the reverse stroke in the cyclic experiments are multiplied by a factor 100; the shear stress directly after the strain path change in the the orthogonal test with unloading is multiplied by a factor 150 and the shear

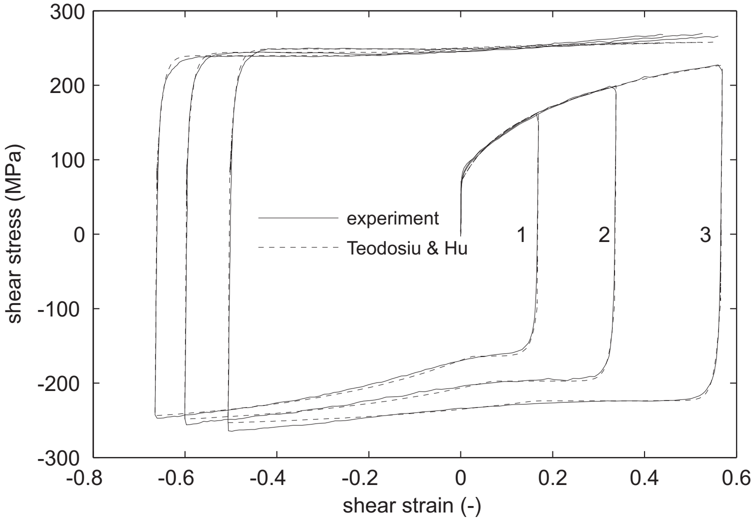

Figure 5.9: The description of the cyclic experiments by the Teodosiu & Hu model.

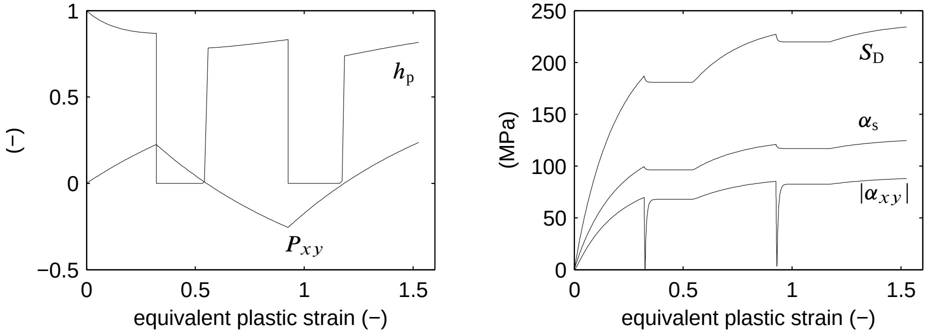

(a) The evolution of h_p and P_{xy}.

(b) The evolution of α_{xy}, α_s and S_D.

Figure 5.10: Evolution of state variables in cyclic test 2.

stresses directly after the strain path change in the orthogonal tests without unloading are multiplied by a factor 75.

The results of the fitting procedure of the material parameters on the Teodosiu & Hu model are depicted in Figure 5.9 and Figure 5.11. The cyclic experiments in Figure 5.9 show that the Teodosiu & Hu model describes the behaviour in this loading scenario well. The Bauschinger effect, the transient hardening and the work hardening stagnation are captured by this material model. The quality of the fit is independent of the amount of pre-strain in the experiments. A small discrepancy is observed at the end of the second and third strokes. The fitting results show a lower stress than the measured stress. For this situation, the isotropic hardening law can be extended with a term that is linear with respect to the equivalent strain.

According to the results depicted in Figure 5.9, the approach followed in the Teodosiu & Hu model seems to work well. The evolution of the internal variables that represent the micro-structure is depicted in Figure 5.10. It can be seen that the polarity component in the shear direction (P_{xy}) increases in the first stroke of simple shear (Figure 5.10(a)). The value for h_p starts at 1, but decreases because S_D and $\mathbf{P}$ have a different evolution rate, leading to $h_\mathrm{p} < 1$ in Equation (5.54). The values for α_{xy}, α_s and S_D increase accordingly (Figure 5.10(b)). Directly after the reversal, P_{xy} decreases and $h_\mathrm{p} \to 0$. This causes a stagnation in the evolution of S_D, and consequently in α_s. In turn, the back stress α_{xy} does not evolve any further and hence the stress response in Figure 5.9 mimics the work hardening stagnation. The same procedure is followed after the second load reversal.

Figure 5.11 shows the results in the experiment with an orthogonal loading strain path change with elastic unloading. Overall, the model describes the experiments accurately, except right after the strain path change. The increase in shear stress in the fitting procedure is not as steep as in the experiment and does not reach the maximum observed in the experiment. However, the evolution of the internal state variables show that the orthogonal strain path change is detected by the model. Just before the strain path change $\mathbf{S}_\mathrm{L} = \mathbf{0}$ and $S_\mathrm{D} \approx 125\,\mathrm{MPa}$. At the strain path change, the orientations of S_D and $\mathbf{S}_\mathrm{L}$ are interchanged. The directional strength decreases to 0 (Figure 5.11(b)) and $\mathbf{S}_\mathrm{L}$ increases strongly (Figure 5.11(c)). The increasing value for $\mathbf{S}_\mathrm{L}$ leads to a sharp increase in α_s via Equation (5.53). This results in a fast development of the back stress in the shear direction (α_{xy}) and a sudden increase in the shear stress (σ_{xy}) in Figure 5.11(a). At the same time, h_α shows a peak which in turn hampers the evolution of S_D after the strain path change. The evolution of S_D is slower than the decrease of $\mathbf{S}_\mathrm{L}$, and hence α_s decreases. This effect is passed on to α_{xy} and is reflected in the decrease in σ_{xy} in Figure 5.11(a).

After the strain path change, the Teodosiu & Hu model also predicts a peak in the tensile stress, Figure 5.11(a). The maximum value that is reached is 75 MPa. During the tensile deformation, α_y evolves, but it does not evolve to 0 upon elastic unloading. Hence, as the stress state moves through the elastic region and becomes plastic at the yield surface, the stress state will translate over the yield surface towards the simple shear point. However, the simple shear point does not lie at the axis $\sigma_y = 0$ because $\alpha_y \neq 0$. As deformation continues, α_y vanishes and $\sigma_y \to 0$. Only then the simple shear point of the yield surface is on the axis $\sigma_y = 0$.

The results of the continuous orthogonal strain path change and the fit by the Teodosiu & Hu model are presented in Figure 5.12. In this experiment the stress–strain curve is described well. In particular, the overshoot is captured accurately. The noise observed in the tensile stress after the strain path change is caused by the noise in the measured strain in the experiments. Although the strain input is smoothed, the remaining noise causes the stress state to enter the elastic region. This does not influence the state variables that describe the hardening of the material. As in the cyclic experiments, the stress is under predicted at higher strains. Because the stress state translates over the yield surface, α_{xy} increases rapidly, but also α_y vanishes during the translation over the yield surface. This explains why the model does not show the peak in tensile stress after the strain path change,

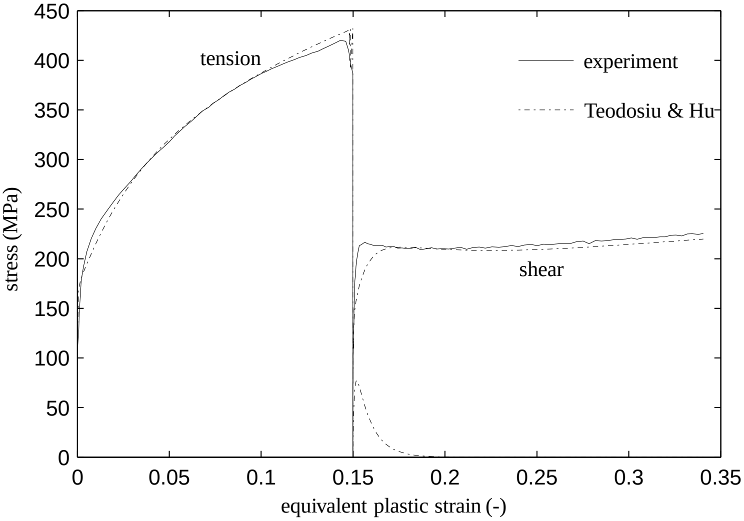

(a) The stress–strain curve for the Teodosiu & Hu model and the experiment.

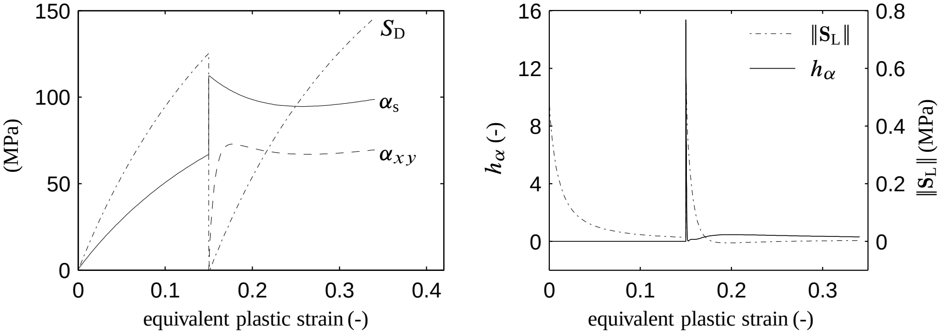

(b) The back stress, the saturation value and the directional strength.

(c) The internal variable h_α and the evolution of the norm of $\mathbf{S}_L$.

Figure 5.11: The stress prediction of the Teodosiu & Hu model in the orthogonal test with intermediate elastic unloading.

which is observed in the simulation of the test with elastic unloading.

In Figure 5.11 it is observed that the overshoot is not described accurately. The typical cross-hardening is not fully captured, but the experiments with strain path reversals (Figure 5.9) and the orthogonal experiments with a continuous strain path (Figure 5.12) are described well. To improve the description of the experiment with an orthogonal strain path change with intermediate unloading, another fit procedure was performed, in which the results of that test make a larger contribution to the objective function. The results of this fitting procedure are depicted in Figure 5.13. Indeed, the description of the orthogonal experiment is improved, the cross-hardening is better described, but the fit is still not “on

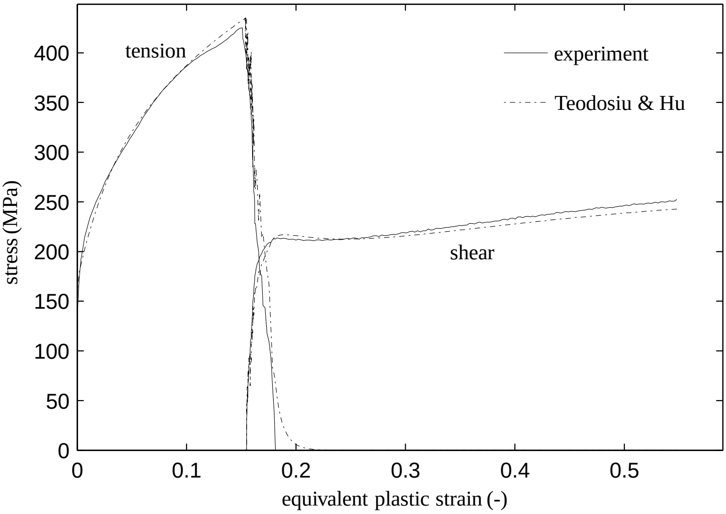

Figure 5.12: The stress–strain curves for the experiment with a continuous orthogonal strain path change and the prediction of the Teodosiu & Hu model.

top” of the experimental results. In Table 5.2 the the parameters for the current fit show a smaller contribution of the kinematic hardening (m = 0.9 instead of m = 0.47) to the model. This explains why the peak in the tensile direction after the strain path change is smaller than observed in Figure 5.11(a). Figure 5.13(b) shows the results of this fit to the experiments with cyclic loading. Here, the description of the experimental results is relatively poor. Hence, the accuracy of the description of the experiments with orthogonal strain path changes comes at the cost of loss of accuracy in the description of the cyclic experiments.

5.4 The Levkovitch model

In this model the different hardening phenomena are modelled with three different hardening models. Kinematic and isotropic hardening are employed to describe the monotonic and cyclic loading behaviour of material. These two models are confirmed in the literature and are much used in material modelling. The overshoot that is observed in an orthogonal loading scenario is modelled with distortional hardening (Levkovitch and Svendsen, 2007). The change of the yield surface is described such that it does not affect the stress–strain relation in monotonic and cyclic loading. Only in the latent part of the loading direction does the shape of the yield surface change. The motivation for this approach is found in the work of Peeters *et al.* (2002), in which orthogonal strain path changes are correlated with a change in yield surface. Experiments were performed on mild steel with strain path changes from plane strain tension to simple shear. X-ray diffraction was used to describe the crystallographic texture. Additionally, the formation of CBB’s was discussed and the influence

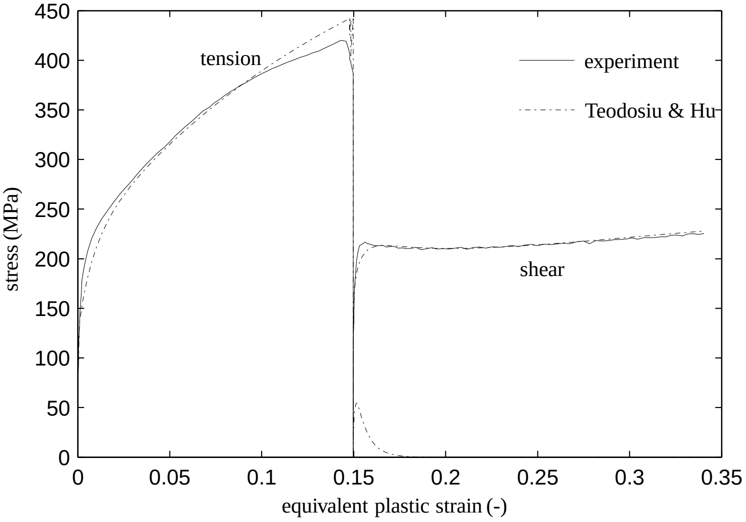

(a) The orthogonal experiment with intermediate elastic unloading.

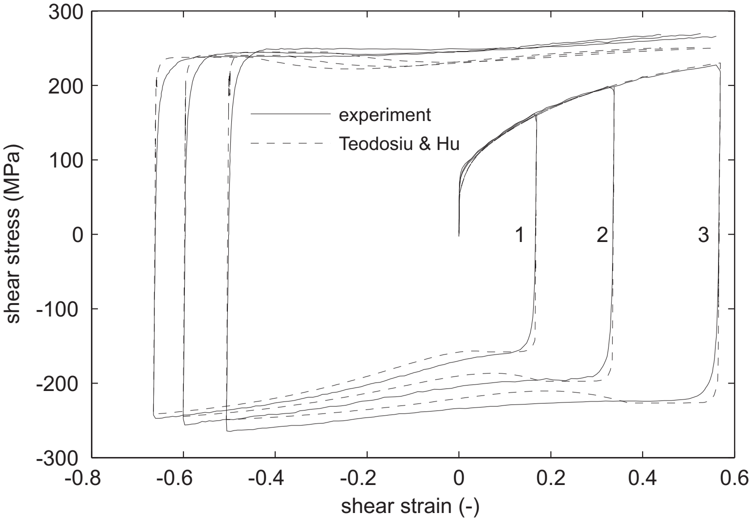

(b) The cyclic experiments.

Figure 5.13: Results of the Teodosiu & Hu model with a better fit of the orthogonal strain path change.

of these on the elastic–plastic transition. This allowed the determination of the shape of the yield surface at the end of the pre-strain phase. The resulting yield surfaces showed a “growth” of the yield surface in the latent direction. The observed distortion is used in the

Table 5.2: The Teodosiu & Hu material parameters for DC06.

(a) Fit with the emphasis on the behaviour during cyclic loading.

parameter	value
τ_0 (MPa)	125.0
α_0 (MPa)	0.5
S_{s} (MPa)	238.8
R_{s} (-)	65.0
C_{p} (-)	1.2
C_{l} (-)	50.0
C_{d} (-)	5.42
C_{α} (-)	164.7
C_{r} (-)	44.4
n_{p} (-)	350.0
n_{l} (-)	0.85
m (-)	0.47
r (-)	2.85

(b) Fit with the emphasis on the behaviour in orthogonal strain path changes.

parameter	value
τ_0 (MPa)	90.0
α_0 (MPa)	0.93
S_{s} (MPa)	294.2
R_{s} (-)	62.5
C_{p} (-)	5.06
C_{l} (-)	38.13
C_{d} (-)	6.80
C_{α} (-)	250.0
C_{r} (-)	145.7
n_{p} (-)	66.36
n_{l} (-)	0.77
m (-)	0.90
r (-)	14.305

Levkovitch model to describe the cross-hardening effect. The segmented construction of this material model allows the use of different isotropic and kinematic hardening models for the description of the behaviour under cyclic and monotonic loading. In this work, the Swift law is employed for the isotropic hardening and the Armstrong–Frederick law is used for the kinematic model.

In the original work, the Hill'48 yield criterion was adapted for the distortional hardening:

$$\phi = \sqrt{\boldsymbol{\zeta} : (\mathbf{M} + \mathbf{H}) : \boldsymbol{\zeta}} - \sigma_{\mathrm{f}} \tag{5.68}$$

The tensor $\mathbf{M}$ describes the initial material parameters of the Hill'48 criterion. $\mathbf{H}$ is a fourth order tensor, analogous to $\mathbf{M}$, describing the distortion of the yield surface. If $\mathbf{H} = \mathbf{0}$ the initial yield surface is described. A similar procedure as in Section 5.1.2 can be used to replace the Hill'48 yield criterion with an alternative description. This is done by substituting the first term in the root with the square of an alternative material model:

$$\phi = \sqrt{\left(\sigma_{\mathrm{eq}}\left(\boldsymbol{\zeta}\right)\right)^2 + \boldsymbol{\zeta} : \mathbf{H} : \boldsymbol{\zeta}} - \sigma_{\mathrm{f}} \tag{5.69}$$

The Teodosiu & Hu model and the Levkovitch model use a similar equation for the dislocation structure and distortion, respectively. The Levkovitch model also applies a division between the directional and the latent distortion, depending on the current loading direction $\mathbf{N}$:

$$H_{\mathrm{D}} = \mathbf{N} : \mathbf{H} : \mathbf{N} \tag{5.70}$$

$$\mathbf{H}_{\mathrm{L}} = \mathbf{H} - H_{\mathrm{D}}\mathbf{N} \otimes \mathbf{N} \tag{5.71}$$

The evolution of the distortion is described in terms of a direction and a latent part:

$$\dot{\mathbf{H}} = C_\mathrm{d}\left(H_\mathrm{d}^\mathrm{s} - H_\mathrm{D}\right)\mathbf{N}\otimes\mathbf{N}\,\dot{\lambda} + C_\mathrm{l}\left(H_\mathrm{l}^\mathrm{s}\left(\mathbf{I}-\mathbf{N}\otimes\mathbf{N}\right) - \mathbf{H}_\mathrm{L}\right)\dot{\lambda} \tag{5.72}$$

The first term on the right hand side of this equation describes the directional distortion and the second term the latent distortion. The directional distortion is determined with the parameters C_d and H_d^s that describe the evolution rate and the saturation value, respectively. C_l and H_l^s control the evolution of the latent distortion. $\mathbf{I}$ describes the fourth order unit tensor.

To adapt the mechanical behaviour under non-proportional loading *only*, the parameter $H_\mathrm{d}^\mathrm{s} = 0$. During monotonic loading the latent distortion will evolve to H_l^s and the directional distortion will remain 0. Hence, in monotonic or cyclic loading, the isotropic and kinematic hardening laws dictate the stress–strain relation. Only when another strain path is applied will the distortion affect the mechanical behaviour. This is the result of the change in $\mathbf{N}$, that changes the division of the distortion in the latent and the directional parts. Hence, in an orthogonal strain path change the previously latent distortion becomes directional and the stress state translates to a “distorted” part of the yield surface. Depending on the distortion, the flow stress is changed to describe the cross-hardening effect. After the strain path change, $\mathbf{N}$ is again constant, and $H_\mathrm{D} \to 0$. This results in a lower flow stress and as such mimics the softening after the overshoot.

The overshoot observed in the orthogonal test is described with an increase in the elastic domain with the Levkovitch model. This is in contrast with the Teodosiu & Hu model that predicts a low flow stress and a high hardening rate in an orthogonal strain path change.

5.4.1 Implementation

In this work, a combination of isotropic, kinematic and distortional models is used. In particular, the framework as presented in Section 5.2 is desirable. To this end, Equation (5.72) needs to be rewritten in a residual format. This equation reads upon discretisation as follows:

$$\mathbf{R}_\mathrm{H} = \Delta\mathbf{H} - C_\mathrm{d}\left(H_\mathrm{d}^\mathrm{s} - H_\mathrm{D}\right)\mathbf{N}\otimes\mathbf{N}\Delta\lambda - C_\mathrm{l}\left(H_\mathrm{l}^\mathrm{s}\left(\mathbf{I}-\mathbf{N}\otimes\mathbf{N}\right) - \mathbf{H}_\mathrm{L}\right)\Delta\lambda \tag{5.73}$$

This evolution results in a system of 81 equations if no use is made of symmetry. To speed up the calculation, the tensor is rewritten in the format of the $\mathbf{M}$ tensor in the Hill’48 yield criterion. Hence, the shear contributions are determined by one component in $\mathbf{H}$ and the yield surface distortion is independent of the hydrostatic stress. Then $\mathbf{H}$ reads, in matrix format:

$$[\mathbf{H}] = \begin{bmatrix} T_2+T_3 & -T_3 & -T_2 & 0 & 0 & 0 \\ -T_3 & T_1+T_3 & -T_1 & 0 & 0 & 0 \\ -T_2 & -T_1 & T_1+T_2 & 0 & 0 & 0 \\ 0 & 0 & 0 & T_4 & 0 & 0 \\ 0 & 0 & 0 & 0 & T_5 & 0 \\ 0 & 0 & 0 & 0 & 0 & T_6 \end{bmatrix} \tag{5.74}$$

This symmetric matrix is fully determined by the parameters $T_1 ... T_6$. The set of residual functions for a combined isotropic/kinematic hardening model with distortional hardening is presented here:

$$\begin{aligned}
\mathbf{R}_\sigma &= \Delta\boldsymbol{\varepsilon} - \mathbf{E}^{-1}\Delta\boldsymbol{\sigma} - \Delta\lambda\frac{\partial\phi}{\partial\boldsymbol{\sigma}} \\
\mathbf{R}_\alpha &= C_\alpha\alpha_\mathrm{s}\mathbf{N}\Delta\lambda - C_\alpha\boldsymbol{\alpha}_n\Delta\lambda - (1 + \Delta\lambda C_\alpha)\,\Delta\boldsymbol{\alpha} \\
\mathbf{R}_H &= \Delta\mathbf{H} - C_\mathrm{d}\left[H_\mathrm{d}^\mathrm{s} - H_\mathrm{D}\right]\mathbf{N}\otimes\mathbf{N}\Delta\lambda - \\
& C_\mathrm{l}\left[H_\mathrm{l}^\mathrm{s}\,(\mathbf{I} - \mathbf{N}\otimes\mathbf{N}) - \mathbf{H}_\mathrm{L}\right]\Delta\lambda \\
\mathbf{R}_\phi &= \sqrt{\sigma_\mathrm{eq}^2 - \boldsymbol{\zeta}\mathbf{H}\boldsymbol{\zeta}} - \sigma_\mathrm{f}
\end{aligned} \tag{5.75}$$

Since only the components of **T** need to be determined, only the components on the diagonal of $\mathbf{R}_H$ need to be used in the return mapping algorithm. The full matrix can then be constructed from the values of **T**.

The state variables that are determined with this update are:

$$\{\mathbf{V}\} = \begin{Bmatrix} \Delta\boldsymbol{\sigma} \\ \Delta\boldsymbol{\alpha} \\ \Delta\mathbf{T} \\ \Delta\lambda \end{Bmatrix} \tag{5.76}$$

5.4.2 Application to DC06

In this section the application of the Levkovitch model to DC06 is discussed. The material model is fitted to the experiments with monotonic, cyclic and orthogonal strain paths. The distortional model is developed such that it does not influence the stress–strain relation in a monotonic or cyclic strain path. Hence, firstly the material parameters for the isotropic/kinematic hardening are determined. With these parameters fixed, the parameters of the distortional hardening are fitted to the orthogonal experiments. It is noticed that with the current description of the kinematic hardening, it is not possible to describe all the phenomena that occur in a cyclic strain path change. For this kinematic hardening model, a good description of the stress level at the end of the third stroke in the experiment with cyclic loading can be achieved. This is at the expense of a relatively poor fit of the initial part of the stress–strain curve. A good fit to the initial part of the stress–strain curve can be also be obtained, but then the results for higher strain levels are poor. For both fits, the distortional model has to be adapted for an accurate description of the hardening in the experiment with an orthogonal strain path change. The fitting procedure is performed with the internal least squares optimisation from MATLAB: `lsqcurvefit`.

To have a proper fit of the initial part of the hardening curve, the contribution of the monotonic experiments to the objective function is increased. The result of this optimisation is depicted in Figure 5.14. Indeed, the initial part of the hardening curve is represented well, but the remainder of the stress–strain curve is not as well represented. The Bauschinger effect is predicted well, but transient hardening is not described by this set of parameters. The stress–strain curve deviates approximately by 75 MPa directly after the strain path change, but at the end of the second stroke, the experiment and the fit do coincide acceptably. The difference after the second reversal is not as poor as after the first reversal, but the hardening rate is too high, resulting in a too high stress level at the end of the third stroke.

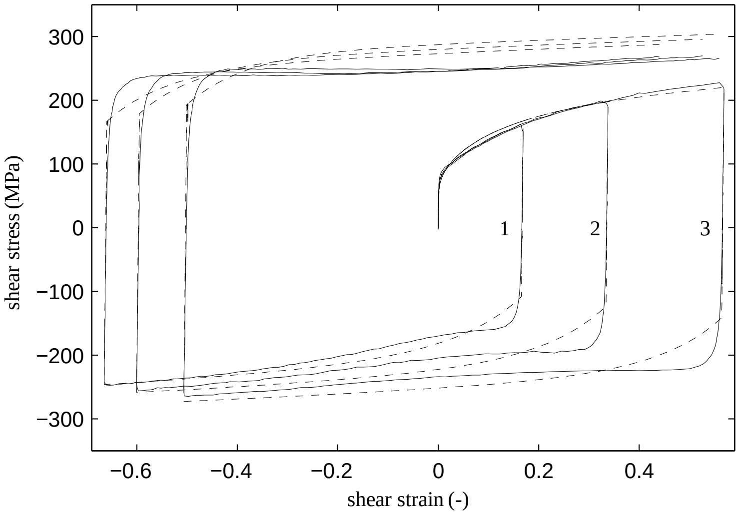

Figure 5.14: The experimental cyclic results (solid lines) with the fit of the Levkovitch model (dashed lines).

Table 5.3: Levkovitch material parameters for DC06.

(a) Fit with the emphasis on the initial part of the hardening curve.

parameter	value
σ_0 (MPa)	70.0
C (MPa)	349.0
ε_0 (-)	$5.0 \cdot 10^{-5}$
n (-)	0.2969
C_α (-)	15.0
α_s (-)	40.0
C_d (-)	15.0
H_d^s (-)	0.0
C_l (-)	11.0
H_l^s (-)	0.65

(b) Fit with the emphasis on the cyclic loading.

parameter	value
σ_0 (MPa)	0.0
C (MPa)	413.7
ε_0 (-)	$3.42 \cdot 10^{-5}$
n (-)	0.1961
C_α (-)	53.12
α_s (-)	15.00
C_d (-)	5.39
H_d^s (-)	0.0
C_l (-)	3.95
H_l^s (-)	0.77

With the fit for the isotropic and kinematic hardening models, the parameters for the distortional hardening model are determined. The material parameters are denoted in Table 5.3(a). The results for the experiments with and without intermediate elastic unloading are depicted in Figure 5.15. The results of this set of material parameters shows a good

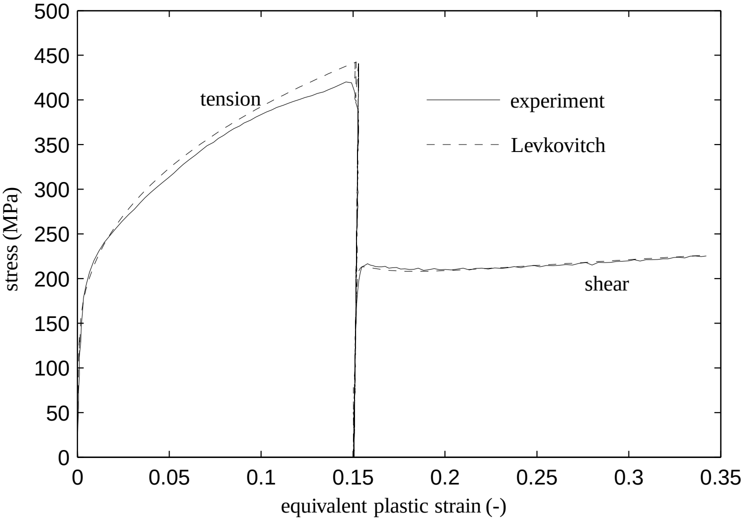

(a) The stress–strain curve for the experiment with elastic unloading.

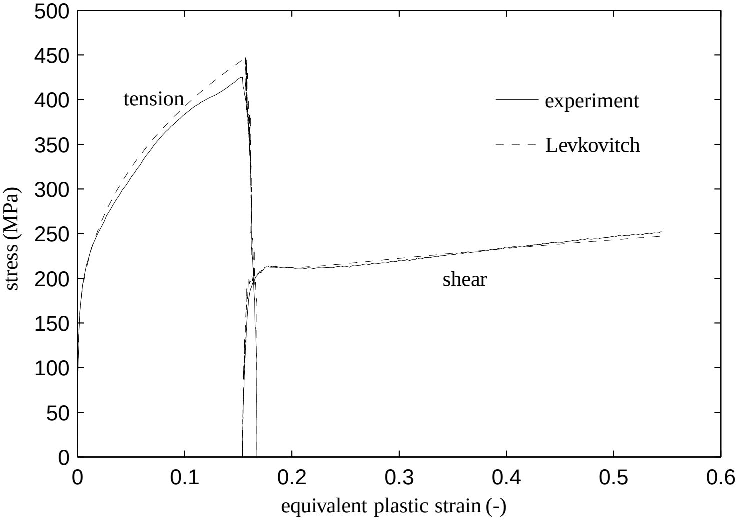

(b) The stress–strain curve for the experiment without elastic unloading.

Figure 5.15: The Levkovitch model in the experiments with an orthogonal strain path change.

description of the orthogonal experiments. The peak in the shear stress after the strain path is captured for both the strain path with and without intermediate elastic unloading. Also the work softening that is measured in the experiment is captured by the model. After that the regular hardening curve is followed accurately.

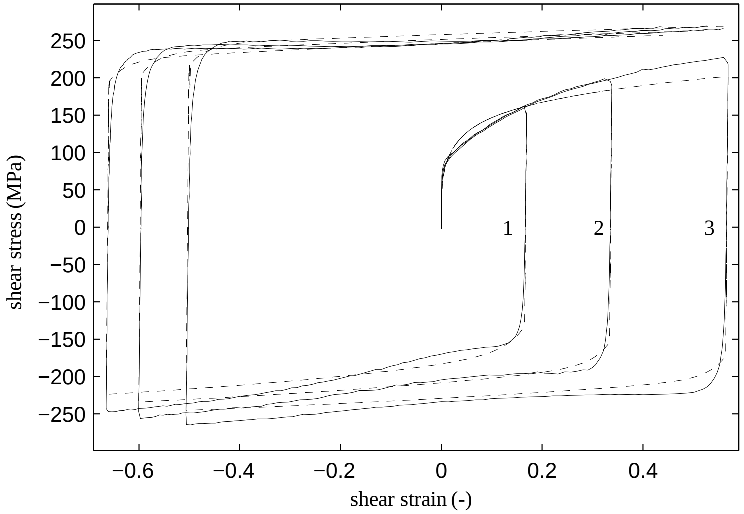

(a) The description by the Levkovitch model (dashed lines) of the experiments (solid lines) with cyclic loading.

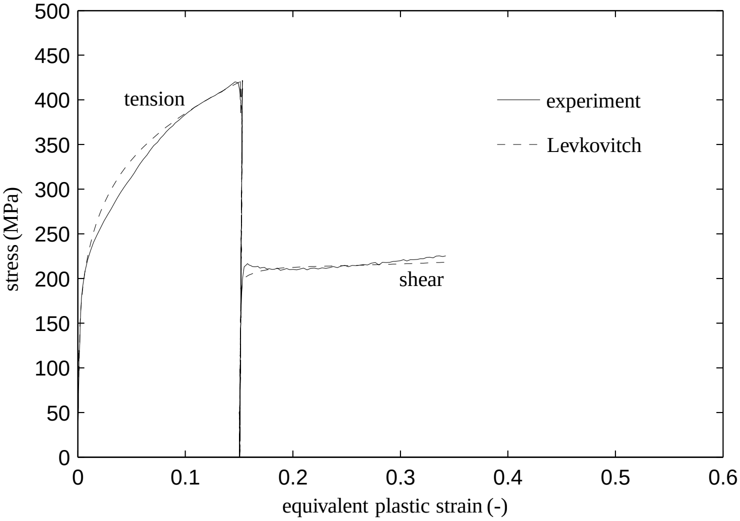

(b) The orthogonal experiment with elastic unloading.

Figure 5.16: The result of the parameter fit of the Levkovitch model with increased weight in the objective function for the Bauschinger effect.

The performed fit provides a good agreement for the initial hardening and the mechanical behaviour in an orthogonal strain path change. The fit of the cyclic experiment however is poor. For that reason an extra fitting procedure was performed to improve the description in cyclic loading. The results of this fit for the experiment with cyclic loading and with an orthogonal strain path change are depicted in Figure 5.16. The material parameters are denoted in Table 5.3. Indeed, Figure 5.16(a) shows an improved prediction of the cyclic behaviour. Especially, the stresses after the load reversals are in better agreement with the experiments. At the end of the third stroke, the measured stress coincides with the prediction of the model. In the first stroke however, the hardening rate is initially too high, and subsequently too low. At the end of the first stroke in test 3, the difference in stress level is approximately 30 MPa. Figure 5.16(b) shows the fit of the distortional hardening model to the experiment with an orthogonal strain path change with intermediate elastic unloading. The characteristic peak after the strain path change cannot be captured with this set of parameters for the isotropic/kinematic hardening. This is due to the high evolution rate of the kinematic hardening. As the strain path changes, the increase of kinematic hardening is larger than the decrease in stress due to the distortional hardening. More distortion indicates a higher initial yield stress and a better initial description of the peak, but due to the rapid kinematic evolution, the stress would increase even further, hereby creating a large discrepancy between the model and the experiment. The result observed represents a balance between a good description of the stress peak and a good description of the softening after the peak.

To describe the monotonic hardening, cyclic behaviour and cross-hardening, the Levkovitch model needs to be adapted. With the current combination of isotropic, kinematic and distortional hardening models, only the cross-hardening or only the cyclic behaviour is described accurately.

5.5 Strain path change indicator

The material models presented in this chapter show different methods to describe the mechanical behaviour of sheet material. The increased accuracy that is acquired via the strain path sensitive models is obtained at the expense of two difficulties. Firstly the material models are more extensive compared to the regular material models. The Teodosiu & Hu model for example, requires 10 times more processing time in a simulation of cup deep drawing. Although a good convergence within the Teodosiu & Hu model is observed, the number of calculations remains higher compared to conventional models. Furthermore, more material parameters are required to fit the models. They cannot be determined from simple monotonic and cyclic tests; orthogonal experiments are required to allow for the complete determination of the material behaviour. It is therefore not a definite choice to use a strain path sensitive material model in simulations. In this section a strain path change indicator is developed that keeps track of the strain path. It indicates whether a strain path sensitive model is essential for a good prediction of the process, or whether a regular material model is sufficient. This makes simulations more efficient, because now the time-consuming material models are only used when necessary.

To trace the strain path in a simulation, some requirements need to be met. The indicator must be easy to evaluate during a simulation, otherwise it would make more sense to use a full strain path dependent material model. Furthermore, it is desirable that the indicator is a state variable that is updated during the simulation. The indicator is implemented at the material model level, which means that strains are used to calculate the strain path sensitivity.

Schmitt *et al.* (1985) proposed a strain path change indicator based on two sequential strain paths. The cosine function is used to indicate the angle between the two strain paths:

$$\beta = \frac{\boldsymbol{\varepsilon}_1 : \boldsymbol{\varepsilon}_2}{\|\boldsymbol{\varepsilon}_1\| \, \|\boldsymbol{\varepsilon}_2\|} \tag{5.77}$$

For monotonic loading $\beta = 1$, for reverse loading $\beta = -1$ and for an orthogonal strain path change $\beta = 0$. This indicator works well for the traditional experiments in which a strain path change is applied by cutting a smaller sample from a larger sample. To describe the strain path changes in a full simulation, the strain increments are used to determine the strain path change:

$$\beta = \frac{\Delta\boldsymbol{\varepsilon}_1 : \Delta\boldsymbol{\varepsilon}_2}{\|\Delta\boldsymbol{\varepsilon}_1\| \, \|\Delta\boldsymbol{\varepsilon}_2\|} \tag{5.78}$$

This formulation makes the indicator step size dependent. In particular in the stage of the simulation where a strain path change occurs, smaller load steps are required to keep the simulation converging. And with a smaller step size, $\beta \rightarrow 1$, because the difference in orientation between two sequential strain increments becomes negligible.

Here, a strain path change indicator is proposed based on the definition of Equation (5.78). Instead of comparing two sequential strain increments; the strain history is compared with the current strain increment. The evolution of the history of the strain path **G** is described by:

$$\dot{\mathbf{G}} = \dot{\boldsymbol{\varepsilon}} - c\dot{\varepsilon}^{\mathrm{p}}_{\mathrm{eq}}\mathbf{G} \tag{5.79}$$

The parameter c determines how much the history of $\boldsymbol{\varepsilon}$ contributes to the evolution of **G**. The strain path change indicator then reads:

$$\xi = \frac{\mathbf{G} : \dot{\boldsymbol{\varepsilon}}}{\|\mathbf{G}\| \, \|\dot{\boldsymbol{\varepsilon}}\|} \tag{5.80}$$

Figure 5.17 shows the results of a strain path that describes reverse loading and orthogonal loading. The indicator clearly captures the reverse ($\xi = -1$) and orthogonal ($\xi = 0$) loading. After continued deformation in the new direction, a difference is observed in how the indicator returns to $\xi = 1$. The reverse loading shows a sudden jump back to $\xi = 1$. This is due to the evolution of the strain history. With every step, the current strain increment is added, with a certain weight, to the strain history. Although this decreases the values of the strain history, the direction of the strain is still oriented with respect to the first strain path. It requires only 1 increment to change the direction from the first to the second direction, which leads to an abrupt change in the sign of the strain path indicator. In the orthogonal strain path change, the *direction* of the strain path history is changed gradually to the current strain path. This shows in the response of the indicator: it gradually returns to $\xi = 1$. The value of c defines the rate at which the indicator returns back to $\xi = 1$. Hence, a sharp strain path will always be noticed; a gradual strain path change can only be detected if the history of the strain path is so large that it still describes the first strain path.

The influence of the step size is depicted in Figure 5.18. Simulations with a large step size ($\Delta\varepsilon_{\mathrm{eq}} = 2 \cdot 10^{-2}$) and with a small step size ($\Delta\varepsilon_{\mathrm{eq}} = 2 \cdot 10^{-4}$) were performed.

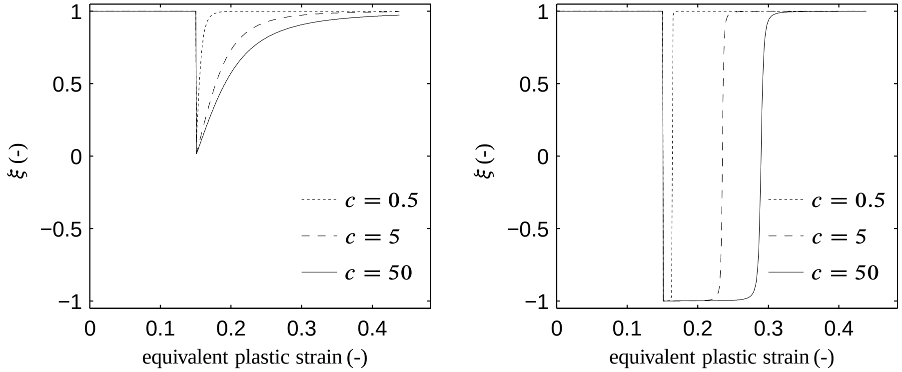

(a) An orthogonal strain path change.

(b) A strain path with load reversal.

Figure 5.17: The influence of c on the strain path change indicator. The strain increment in these tests are $\Delta\varepsilon_{\mathrm{eq}} = 2 \cdot 10^{-4}$.

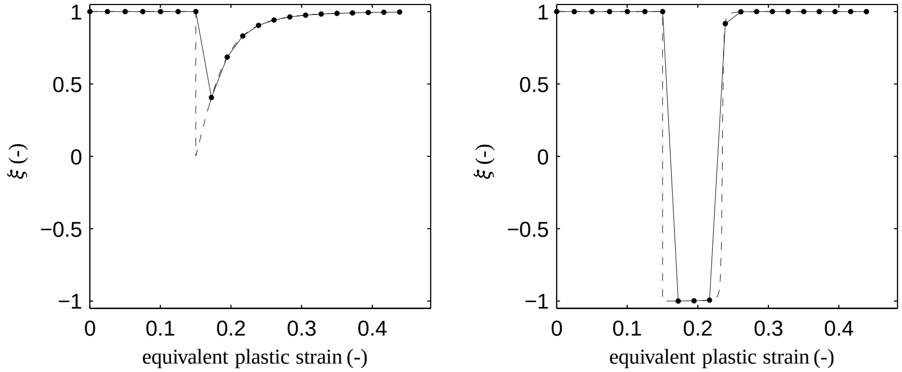

(a) An orthogonal strain path change.

(b) A strain path with load reversal.

Figure 5.18: The influence of different step sizes on ξ with $c = 5$. Dashed lines: $\Delta\varepsilon_{\mathrm{eq}} = 2 \cdot 10^{-4}$ and solid lines: $\Delta\varepsilon_{\mathrm{eq}} = 2 \cdot 10^{-2}$

The figure shows that the strain path change indicator values for the experiment with the large increments correspond with the indicator values calculated for the simulation with the small increments. The curve themselves are different, due to the large intervals in the simulation with the large increments.

Figure 5.19 shows the strain path change indicator (with $c = 10$) for the experiments on DC06 with orthogonal strain path changes (Section 4.5). The indicator shows the same trend for all the experiments, but the minima of the functions differ depending on the sharpness of the strain path. The sharpest strain path change (test 6) has a minimum of $\xi = 0.31$,

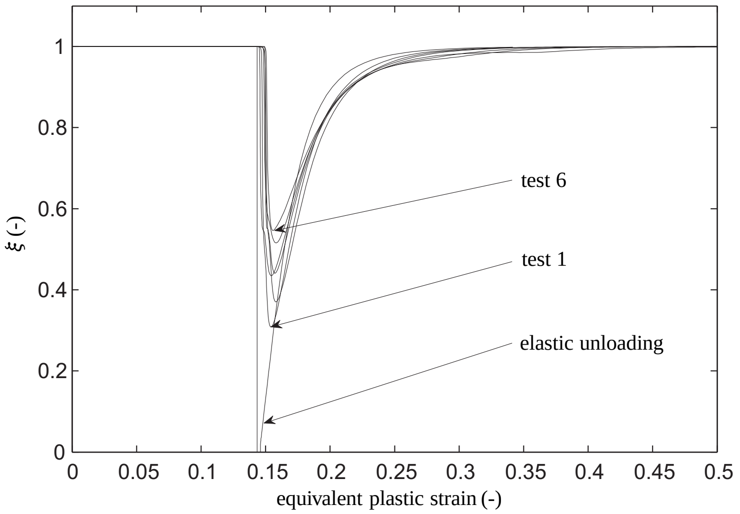

Figure 5.19: The strain path change indicator applied to the experiments on DC06 with orthogonal strain path changes, $c = 10$.

whereas test 1 with a very gradual strain path change shows a value of $\xi = 0.55$. The orthogonal test with elastic unloading is characterised by a value of $\xi = 0$, which represents a true orthogonal strain path change. From this it is concluded that a distinct difference in the indicator appears when orthogonal strain paths are applied with different “sharpnesses” in the transition. The indicator makes clear distinctions and hence can be applied in full simulations. If the values remain in the region of $\xi = 1$, it can be assumed that a material model with isotropic hardening is accurate enough for the simulation investigated. When $-1 < \xi < 0.4$, the material will undergo an orthogonal or reverse strain path change. In these situations the material may show strain path sensitive behaviour, and an advanced material model should be used. For strain path changes where $\xi \approx -1$, only kinematic hardening is required.

The strain path change indicator presented here can quantify a strain path change. In the above, DC06 was used to define the boundaries for the strain path change indicator, which is based on an experimental study. However, if the mechanical behaviour is unknown, *i.e.* the response to cyclic and orthogonal loading has not been determined, the strain path change indicator can still be employed. It indicates whether a strain path change occurs, and hence whether experiments with cyclic or orthogonal strain path changes should be performed. In other cases this parameter will confirm that the material model used is accurate enough in terms of strain path dependency.

5.6 Discussion

In this chapter different models are presented that can, to some extent, predict the strain path sensitive behaviour. The most elaborate model, the Teodosiu & Hu model, gives the best description in cyclic strain path changes. In particular, the transient hardening and the consequent work hardening stagnation can be described accurately, independent of the amount of pre-strain. In the same fit, the orthogonal experiments with a continuous strain path are also well described. An orthogonal strain path change with intermediate elastic unloading, however, cannot be described exactly with this model. In the experiment, it seems that the shear stress increases elastically to the peak. The Teodosiu & Hu model predicts a high hardening rate after the strain path change which is not sufficiently high to capture the cross-hardening effect. By allowing a less accurate fit of the cyclic experiments, the fit with an orthogonal strain path change is improved. In the Levkovitch model, either a good fit of the orthogonal strain path change or of the cyclic experiment is obtained, similar to the fitting procedure of the Teodosiu & Hu model. The Levkovitch model describes the experiments with the orthogonal strain path change better than the Teodosiu & Hu model. In the Levkovitch model, distortional hardening increases the elastic domain in the latent direction. Upon an orthogonal strain path change, the stress in the new direction reaches a higher flow stress, hereby describing the cross-hardening effect. This gives an accurate description of the experimental results. The fit with a good description of the experiment with an orthogonal strain path change gives a poor description of the mechanical behaviour of the experiments with load reversals. A better estimate of the cyclic behaviour was obtained, but the description of the cross-hardening effect was less satisfactory. The cyclic behaviour of the Levkovitch model is dependent on the chosen kinematic hardening law, but it is clear that the Armstrong–Frederick relation is by far not as accurate as the Teodosiu & Hu model. Additionally, the kinematic hardening model in the Levkovitch model reduces the performance in the orthogonal strain path changes. A better model for cyclic hardening within the Levkovitch model is recommended. Both the classical isotropic and combined isotropic/kinematic models cannot describe the overshoot observed in the orthogonal strain path change. The combined model gives a better prediction in the cyclic tests than the isotropic model, but this is still not as accurate as the Teodosiu & Hu prediction.

For use in large scale deep drawing simulations, the models clearly show that accuracy comes at the expense of more computation time. The Teodosiu & Hu model is extensive, with a large system of equations that need to be solved. The Levkovitch model is more economic, but its predictions are not as good. Isotropic and kinematic models require little computation time, and besides, they require a small set of parameters that can be determined easily. The Teodosiu & Hu model and the Levkovitch models require, as well as the monotonic experiments, tests with orthogonal strain paths to fit their parameters. Additionally, the parameter fit becomes more laborious. The engineer has to choose which material model is suitable for the process simulated. This choice can be checked after the simulation with the presented strain path change indicator. Still, for effective use of the indicator some knowledge about the mechanical behaviour is required. Hence, the monotonic experiments have to be extended with cyclic and orthogonal experiments. However, the mechanical behaviour is then restricted to the observations on the presence of strain path change effects.

In the following chapter, the material models discussed here are evaluated in full deep drawing simulations. The outcome of the simulations are compared with actual measurements on the process. This will give an indication of the added value of the strain path dependent material models.

6. Validation

This chapter discusses the validation of the presented material models by comparing model predictions with biaxial experiments and a deep drawing experiment. Biaxial experiments with continuous tensile deformation and cyclic shear, see Section 4.4, provide strain path dependent experiments that can be used to validate the material models. In the initial monotonic part of the experiments, the yield criterion determines, via the direction of plastic flow, the ratio between tensile and shear stresses. The Hill'48 and Vegter yield criterion are assessed via these deformation modes. The complete experiment, including load reversal in shear, under tensile deformation, requires an accurate prediction by the hardening laws. The Teodosiu & Hu model, the Levkovitch model with isotropic/kinematic hardening and the classical isotropic/kinematic hardening model are validated using experiments on DC06, AA5182 and H340LAD.

To demonstrate the applicability of the material models in a real product, the so-called "cross-die" product is used. This semi-academical deep drawing product is used to investigate different aspects of deep drawing. In this research, it is used to show the application of the strain path change indicator and the different predictions of the material models.

6.1 Biaxial experiments

The combined tension–simple shear experiments were presented in Section 4.4. A constant plane strain deformation is applied and meanwhile cyclic simple shear is imposed on the sample. The applied strain path change varies depending on the amount of plane strain deformation. The tensile deformation is a continuous process, but the shear deformation is reversed. In practice the strain path change cannot be applied strictly, because of limited stiffness in the test equipment. In the absence of simple shear, the tensile deformation constantly increases. This smoothes the strain path change to some extent. Figure 6.1 presents the stress development during an experiment, according to an isotropic hardening model. Figure 6.1(a) shows the evolution of the stresses measured in an actual experiment on H340LAD (test 1 in Figure 4.11(c)). The stress path in such a test is explained in Figure 6.1(b) with a prediction of the stress evolution by an isotropic hardening model. Starting at zero stress, the stress increases elastically in both shear and tension to t_1. At the initial yield surface (ϕ_0), the stress state enters the plastic regime and work hardening appears. The plastic regime also induces a *stress* path change, due to the different stress ratios for elastic and plastic deformation. As the stress state reaches t_2, the simple shear deformation is reversed. Meanwhile, the tensile deformation continues. The stress state "crosses" the elastic regime, while the tensile stress still increases. This requires only a

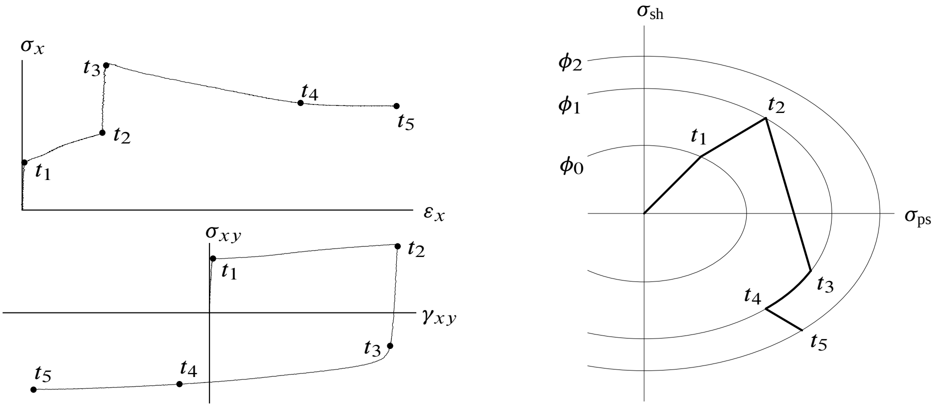

(a) The stress–strain evolutions of H340LAD.

(b) The description of the stress path based on the strain path and an isotropic hardening model.

Figure 6.1: The experiment with cyclic shear under tension on H340LAD explained with an isotropic hardening model. $t_{1..5}$ denote the characteristic points in the stress–strain curve.

small strain and it is represented in the stress–strain curve by a sharp increase and decrease in tensile and shear stress, respectively. At the opposite side of the yield surface ϕ_1, at t_3, the direction of plastic flow dictates the stress state. This causes a shift across the yield surface towards t_4. In the model, this would only require a small amount of strain, but in practice, the used strain is relatively large. As monotonic hardening is resumed, with a constant direction plastic flow, the stress should increase again. Indeed, the measured shear stress shows this trend, but the tensile stress remains more or less constant. Eventually, the stress state reaches ϕ_2 at t_5.

The predictive performance of the material model during the load change is dominated by the hardening model. The calculated stresses for the Teodosiu & Hu model, the Levkovitch model and the classical isotropic/kinematic hardening model are compared with the stresses for this experiment in Section 6.1.1. The material parameters used can be found in Appendix A. The strains that are measured in the experiments are used as input for simulations of a single element test in DIEKA. The experimental noise on the strain data was removed by smoothing. Especially when the stress is in the elastic regime, the stress calculation magnifies the effect of noise. This is also considered in the next sections.

The Hill'48 and the Vegter yield criterion are assessed with the first stroke of the experiments (t_0 - t_2) in Section 6.1.2. In the model, the ratio between the tensile and shear stresses depends on the position of the stress state on the yield surface, which in turn is determined by the direction of plastic flow. Hence, a yield surface that describes the material accurately, predicts the correct ratio between the tensile and shear stresses. It is noted that in the fitting procedure of the material models, both the plane strain tension test and the simple shear experiment are used. Good results were obtained, and hence, the ratio between the stress is only dependent on the yield surface used.

6.1.1 Hardening laws

In this section the performance of the Levkovitch, the Teodosiu & Hu, and the combined isotropic/kinematic material models are assessed by means of simulations of the experiments with tension–cyclic shear. In all material models, the Vegter yield criterion is used.

DC06 In Figure 6.2 the results of the simulations with DC06 are presented. The experiment is presented in Figure 4.9, test 1. The initial shear deformation is well described by all material models, see Figure 6.2(b). The Teodosiu & Hu model has the best performance here. After the load reversal, the Teodosiu & Hu model predicts an initial yielding that is close to the experimental results, but after the transient effect a work hardening stagnation is predicted. This is not observed in the experiments. Both the Levkovitch and the combined isotropic/kinematic models show earlier yielding, with the combined isotropic/kinematic model being almost on top of the experimental results. The tensile stress curve is best represented by the Teodosiu & Hu model. It follows the initial stress curves and shows a decreasing stress after the strain path change. Although the stress level is not completely matching the experiments, the model gives similar results. Both the Levkovitch and the combined isotropic/kinematic hardening model cannot predict the phenomena in the tensile direction. The tensile stress after the load reversal is too high for both models. They do not detect the strain path change, and predict an increasing trend in the tensile stress. Additionally, the distortional model gives a stronger deviation in the initial tensile curve.

Figure 6.2(c) shows the results of the simulations in stress space. Again, the prestraining of the material is similarly described by all models. After the load reversal, the stress state moves through the elastic region and enters the plastic regime again. The slope of the stress paths through the elastic region from the simulations deviate from the slope measured in the experiment. This is due to the small strain increments that cannot be measured accurately during the actual measurement. And because all the material models use the same model to describe elastic behaviour, the slopes of the simulations correspond. The combined isotropic/kinematic model keeps track of the stress curve until the strain path change. After that it starts deviating from the experiments. The Levkovitch model overpredicts the tensile stress before the strain path change and is far from the experimental values. As the stress state reaches the plastic regime again, the models predict a different behaviour. The combined isotropic/kinematic model describes a sharp transition from the elastic to the plastic regime, which is indicated by the sudden change of the stress path. The Teodosiu & Hu model also predicts a kink in the stress path as the stress state becomes plastic again. Right after that the material deviates from the yield surface shape and shows a path that gradually turns to shear. After that the stress path loops back, hereby translating to the origin of the axes. It seems that the work softening, that is normally observed after an orthogonal strain path change is causing softening in both stress components. Although the stress–strain curves described by Teodosiu & Hu in Figure 6.2(a) and 6.2(b) show a good correspondence, the results in stress space are less accurate. The Levkovitch model describes the trends of the experiment in Figure 6.2(c) well, but in absolute values this model is far from the experimental results. Clearly, if the stress curve described by the Levkovitch model would be shifted 80 MPa to the left, the results of this material model would be good.

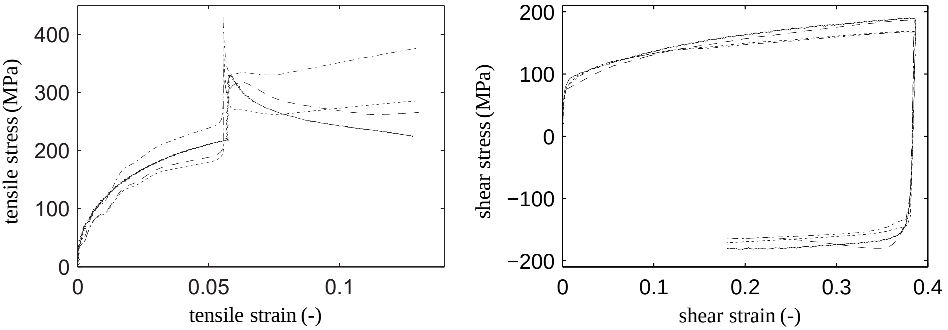

(a) Tensile stress–strain curves.

(b) Stress–strain curves.

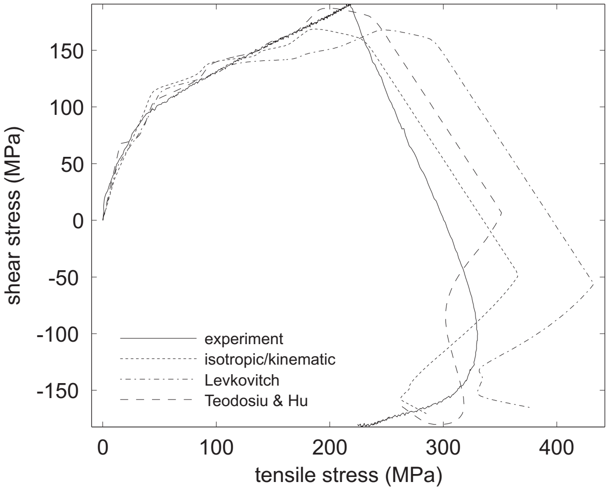

(c) The curves in stress space.

Figure 6.2: Simulation results of the biaxial experiment on DC06 with the Vegter yield criterion. The legend in figure (c) holds also for figures (a) and (b).

AA5182 In the experiments performed on AA5182 in Chapter 4, it was observed that the mechanical behaviour of AA5182 is not strongly dependent on strain path changes. Also the experiments with intermediate elastic unloading in the orthogonal strain path change show that the stress in the new loading direction gradually converges to a saturation rate. Here, test 2 from Figure 4.10 is simulated. The shear curves in Figure 6.3(b) show a similar trend. None of the material models can capture the transient hardening in shear after the strain path change. Eventually, the models catch up with the shear curve. In the tensile direction, the models predict peaks in the curves that are higher than the experimental values. After that, a decrease in tensile stress is predicted with the strain path dependent material models showing the largest decrease. It is noticed that the classical isotropic/kinematic

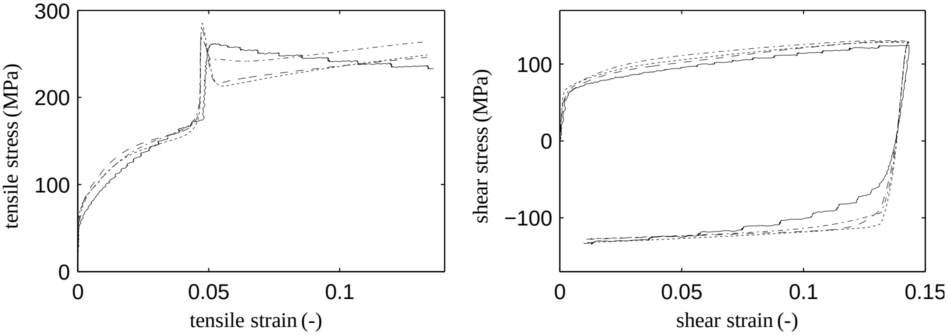

(a) Stress–strain curves in the tensile direction.

(b) Stress–strain curves in simple shear.

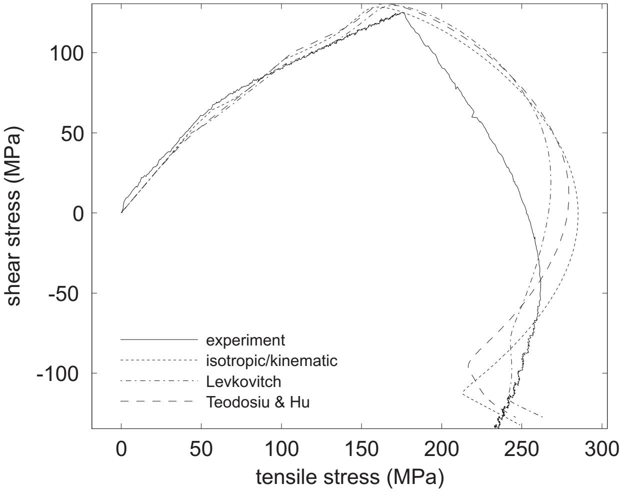

(c) The curves in stress space.

Figure 6.3: Simulation results of the biaxial experiment on AA5182. The legend in figure (c) holds also for figures (a) and (b).

hardening model describes the stress level exceptionally well. The decreasing trend in the tensile curve after that is not captured by the models.

Figure 6.3(c) shows the results in stress space. In contrast with the predictions for DC06, the material models all predict approximately similar behaviour. In the experiment, after the strain path change, the stress state seems to migrate through the elastic regime, which can be concluded from the constant slope that is described. Then, the stress state deviates from this slope and slowly turns to shear. It seems, that in this experiment, the material is migrating closely along the yield surface. In the simulations, the stress state does not migrate through the elastic regime, but translates over it, hereby describing a fluent arc from tension–positive shear to tension–negative shear. Probably, the strain increments that are used for the deformation path show a deviation and cause the stress path in the simulations to follow the yield surface instead of crossing the elastic regime. The combined isotropic/kinematic hardening model describes a kink in the stress path at the moment that monotonic hardening is resumed. The strain path dependent material models by Levkovitch and Teodosiu & Hu describe similar behaviour to the combined isotropic/kinematic model at the moment monotonic hardening is resumed. Only here, the transition to the monotonic hardening is described slightly more smoothly with the strain path dependent models. It is expected that stress curves from the strain path dependent models will not deviate strongly from the curve described by the combined isotropic/kinematic hardening model, because the models were fitted to experiments that show limited strain path sensitivity.

H340LAD In Figure 6.4(b) it is observed that the combined isotropic/kinematic model performs badly in the initial shear curve. As the shear component is activated, its stress level remains at a constant level. After the load reversal, a small dip is observed after which the shear curve again remains almost perfectly constant. The tensile curve also remains at a level that is far below the measured stress curve. This model with the current set of parameters cannot represent the material accurately. The Levkovitch hardening model gives a better prediction of the experiment. The tensile curve is accurately described, and even the initiation of the monotonic loading in the new direction is captured. The shear curve shows a small overshoot after the load reversal, but the general trend is captured with the Levkovitch model. It is noticed that in the shear stress–strain curve all the models show a small overshoot after the load reversal. This indicates that the deformation description is not accurate enough. The Teodosiu & Hu model is also capable of capturing the characteristics of this experiment. The shear curve is captured relatively well, but the tensile component only captures the trend of the stress development. Figure 6.4(c) shows the results in stress space. The experiment shows that the stress, measured in the experiment, translates through the elastic domain, which is indicated by the linear slope after the strain path change. The simulations however, show that the stress state migrates across the yield surface. The combined isotropic/kinematic model and the Levkovitch model have a similar trend when translating over the yield surface. The Levkovitch model however, shows a larger shape of the yield surface, which is attributed to the dominant contribution of the isotropic hardening model in the Levkovitch model. The simulation with the Teodosiu & Hu model describes a part of the load reversal where the stress state is in the elastic regime. As the monotonic hardening is again resumed, all the models describe a confused stress path. This is attributed to the noise on the deformation input, because all models describe this behaviour.

6.1.2 Yield criteria

The initial monotonic deformation of the experiment is a combination of tensile and shear deformation. The first derivative of the yield criterion determines the direction of the plastic flow. This fixes the stress state in the model. The prediction of the ratio between shear and tensile stress indicates the accuracy of the yield criterion. For all the simulation, the classical isotropic/kinematic hardening models were used.

Figure 6.5 shows the results of the simulations of the three experiments. In all the

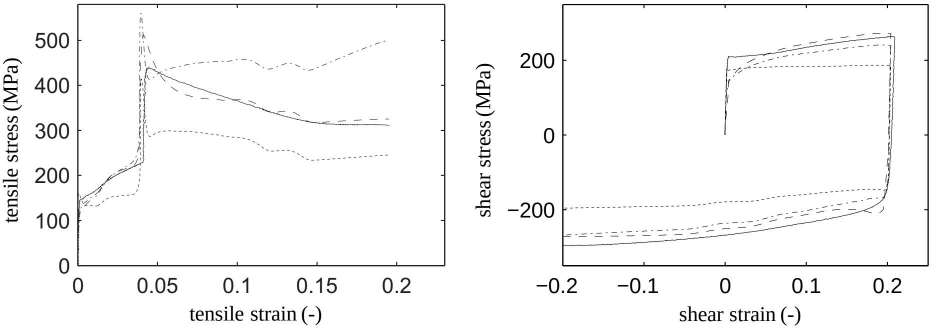

(a) Tensile stress–strain curves.

(b) Shear stress–strain curves.

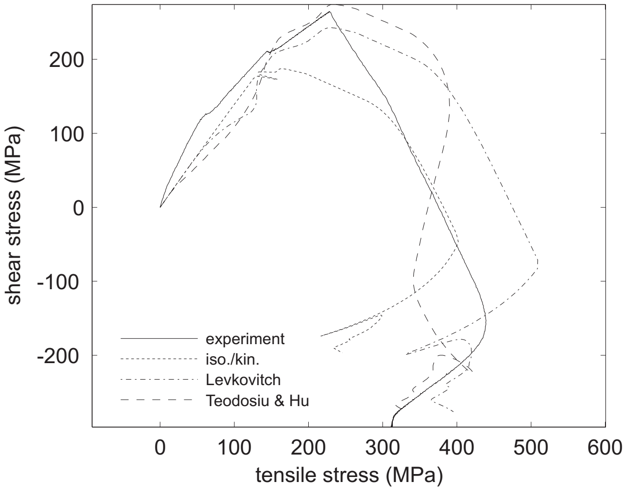

(c) The curves in stress space.

Figure 6.4: Simulation results of the biaxial experiment on H340LAD with the Vegter yield criterion. The legend in figure (c) holds also for figures (a) and (b).

simulations it is observed that the stress–strain curves are not smooth functions. This is due to the use of the strain measurement in the experiment. Due to smoothing of the strain input, the “sharp” edges of the strain signal are eliminated, but the effect of noise is smeared out over the entire strain path. This leads to a slightly wavy strain path, which is reflected in the stresses that show changing trends. In general, none of the simulations correspond exactly with the experiments. The flow curves predicted for AA5182 are not far off, but still the flow stresses are 15–20 MPa too high in the shear curves. The tensile curves correspond well; the Vegter curve in particular seems to capture the behaviour well. The simulation with DC06 shows a good prediction for the shear curve, but the tensile curve was not captured by any of the models. H340LAD was not captured accurately for either

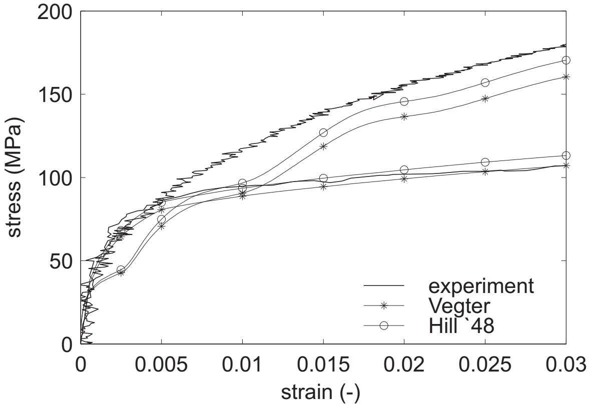

(a) DC06.

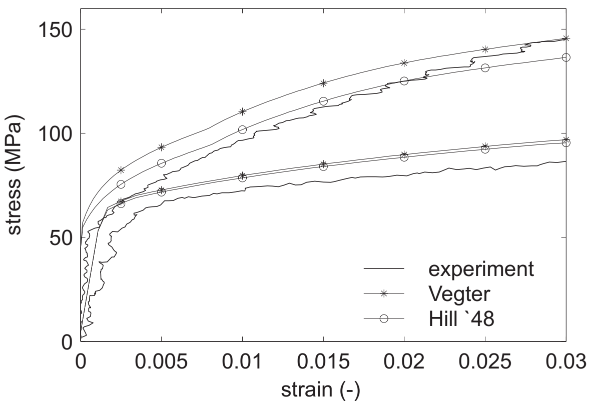

(b) AA5182.

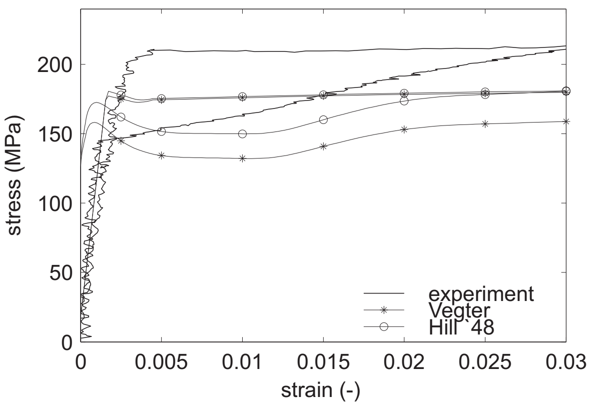

(c) H340LAD.

Figure 6.5: The initial part of the hardening curves for the validation experiment. The solid lines represent tensile stresses and the dashed line represent the shear stresses.

stress components. This material also shows a delayed hardening after it has reached the yield limit. Both yield criteria underestimate the tensile and shear stresses. For the tensile direction, the Hill'48 and Vegter criteria predict the tensile stress at the same level, but the values are almost 50 MPa of from the experimental curve. For the shear curve the same holds, except that the Vegter description shows a larger mismatch with the experiments.

Both the Hill'48 and Vegter criteria cannot accurately capture the stress ratio in tension and shear in the experiments. The Vegter criterion however is an advanced criterion, that uses four experiments to fit the model. It would be reasonable to expect that the Vegter yield criterion would be able to describe the experiments to some extent. For none of the materials is this achieved. Furthermore, the results of the simulations with the two yield criteria describe stress paths that coincide to some extent. The simulations on the experiment with H340LAD shows a 25 MPa difference in the estimated shear stresses. The maximum difference between the stress prediction and the measured stress is, in the case of H340LAD, approximately 40 MPa. Hence, the difference between the predictions of the simulations and the actual measurement is larger than the difference between the individual predictions of the simulations. This leads to the conclusion that using the strain measurement in a simulation to compare the performance of yield criteria is not a good validation tool. If the measurement of strain could be performed more accurately, this validation procedure could be used for validation of yield criteria.

6.1.3 Discussion

In this section simulations were performed with the deformation measured in a true biaxial experiment applied on a single element. It is observed in all the simulations, independent of the material model, or the material used in the experiment, that the results of the simulations show a non-smooth stress path. This is attributed to the measured strain that is used as an input for the simulations. Smoothing of the strains was used to optimise the simulation results, but the result is not satisfactory. The results of the simulations can be improved, if the strain measurement in the experiments is improved. In Chapter 3 it was found that the accuracy of the strain measurement of the TWENTE BIAXIAL TESTER is approximately $5\cdot10^{-4}$. This value allows for measurements in the elastic region, but is clearly not accurate enough to use as input for FE-simulations. Hence, the conclusions that are drawn from the simulations have to be considered carefully.

When considering the yield criteria, the Hill'48 and the Vegter models perform equally well. It was observed that these models predict stress–strain curves that almost correspond, but the experiment is not always well represented. This can imply that the used method is not accurate, but can also indicate that the used concept of a yield criterion is not necessarily adequate for this particular deformation.

The materials used to validate the material models vary in their strain path dependency. The mechanical behaviour of DC06 strongly depends on the strain path, whereas AA5182 shows limited sensitivity. The latter is described well by all the material models, because the simulations differ only in the description of the strain path effects. The mechanical behaviour of the DC06 is only captured with the Teodosiu & Hu model with moderate accuracy. It captures the phenomenon, but cannot describe the stresses quantitatively. The distortional model describes the H340LAD better than the two other models. It captures the trends in the stress development. The isotropic/kinematic material model does suffice in the case of AA5182, but materials that are more sensitive to strain path changes, cannot be accurately described with this model. Also a qualitative description fails.

6.2 Cross die

To asses the material models presented in Chapter 5, simulations were performed on a true deep drawing process. The selected product is the “cross die”, a product made with a cross shaped die. The final product is depicted in Figure 6.6. This product was initially developed as a tool to judge the formability of sheet metal (Atzema *et al.*, 2004). It represents true forming processes better then square or circular cups, because different deformation modes are activated in the deep drawing of the product. The aim is to draw a product to a height of 60 mm with the largest possible blank dimension, without any signs of necking. The used blank must be square and the maximum blank size is denoted with the Cross Die value. DC06 is used here for the assessment of the material models, because it shows the strongest strain path sensitive behaviour. The experiments performed in Chapter 4 are performed with the same batch of material as used for the cross die. The deep drawing experiments were performed at Corus PAC.

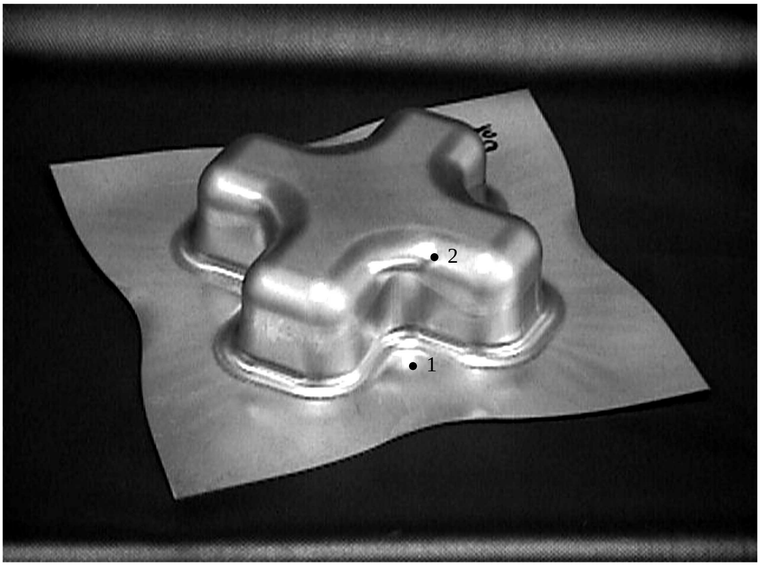

Figure 6.6: The cross die product.

The blank holder force (BHF) used for the cross die experiments was determined with a fixed ratio:

$$BHF = 3/4 R_{\mathrm{m}} t \tag{6.1}$$

Where R_m indicates the maximum stress and t the thickness of the blank. The maximum stress is indicated with R_m and the thickness with t. Hence, the blankholder force increases with increasing thickness and higher strength. According to Equation (6.1), with $t = 0.7$ mm thick, and $R_\mathrm{m} = 300$ MPa the target blankholder force was determined to 157.5 kN. Experiments were performed and showed that a blank with sides of 295 mm ruptures completely. The experiment with sides of 290 mm still showed some mild necking, and was hence rejected. A blank with sides of 285 mm, the full drawing depth (60 mm) was reached without necking. This blank size was used in the simulation of the process.

A hydraulic support was used to apply the blankholder force. While developing the test equipment it was found that the tools deformed elastically during the deep drawing. To this end, 8 force sensors were used in a square setup to measure the blankholder force during the forming. Ideally, the 8 force sensors would carry an even load, but mostly a non-homogeneous distribution of force was measured. The blankholder force in the experiment was found to be 17.4–22.2 kN per load cell and the total blankholder force was 156 kN. For experiments where the spread in the 8 force signals is larger, the symmetry of the deformation could be deteriorated. This would require a complete simulation of the cross die, rather than only a quarter simulation. Additionally, the different segments of the blankholder require individual force control, depending on the measurement. Here, it is assumed that the forces are sufficiently balanced.

Firstly, the process was studied by means of a simulation with an isotropic hardening model. The characteristics of the process and the calculation are discussed. After that, simulations are presented with the Teodosiu & Hu model, the Levkovitch model and the combined isotropic/kinematic hardening model. Conclusions are drawn based on their performance.

6.2.1 The deep drawing process of the cross die

This section discusses the characteristics of the deep drawing process of the cross die. The deep drawing process of this product is analysed by means of a FE simulation. In this simulation, only a quarter of the product is used, due to symmetry of the product and the material. The blank is meshed with 3072 linear discrete shear triangular elements (Batoz and Lardeur, 1989) that have an average length of 4 mm. Five integration points across the thickness were used. The isotropic Swift law was used, combined with the Vegter yield function. The parameters for this material model can be found in Appendix A.

The influence of friction in deep drawing processes is not always determined. From measurements it is known that the friction coefficient $\mu \approx 0.13$. However, due to the lubrication this value is not fixed, and does not necessarily give an accurate result in the simulations. According to the manufacturers of the lubricant, the friction coefficient is 0.13 for normally lubricated sheet. In the presented experiment, less lubrication is applied to enhance the reproducibility. To obtain some feeling for the dependence on friction, simulations were performed with different friction coefficients ($\mu = 0.12, 0.13, 0.14, 0.15, 0.16$) to fit the force–displacement curve. The results are depicted in Figure 6.7. From these results it is concluded that the Vegter model combined with the Swift hardening law is a conservative material model. Independent of the used friction, all the simulations predict force–displacement curves that are lower than the experimental curve. This already appears at the onset of the deformation, at 10 mm punch displacement. Furthermore, in the experiment, the force reaches a constant level at a punch depth of 45 mm, but the simulations predict a maximum force at 50 mm for $\mu = 0.12$. A higher friction results in a shift of the maximum to a higher depth. According to Figure 6.7, the friction should be at least 0.16. A friction coefficient $\mu = 0.14$ is chosen because it is still close to the specification of the lubrication manufacturer, and because the simulation show that a high friction coefficient is required. This friction coefficient is used for the remainder of the simulations, despite the relatively poor description of the punch force. The following will show whether a full strain path dependent material model will improve the performance.

To assess the strain path changes that occur in the deep drawing of the cross die, the strain path change indicator presented in Section 5.5 was used. The memory constant for the indicator was set to $c = 10.0$. The comparison with the experiments with strain path changes showed that a value for the strain path change indicator $\xi < 0.4$ indicates that the traced strain path will show mechanical behaviour that cannot be predicted with a regular isotropic/kinematic hardening model. In Figure 6.8 the value of ξ in the mid-plane of the sheet is shown. In this picture it can be seen that two regions in every 1/8 of the product experience strain path changes. These two regions are more clearly indicated in Figure 6.6. Region (1) appears at the draw-in. As the material is pulled towards the die cavity and flows into it, the strain path changes. This is easily understood when the flow of the material is considered. As the material is clamped between the die and the blankholder, but still far away from the die cavity, it is pulled towards the die cavity. In this process, the material experiences a tensile strain in the direction of the centre of the die cavity and a compressive strain perpendicular to that. As the punch goes deeper, this material enters the die cavity. However, at the joint between the two arms of the cross, the material is drawn into the cavity on both sides, while the tensile strain remains. Hence in the transverse direction, the

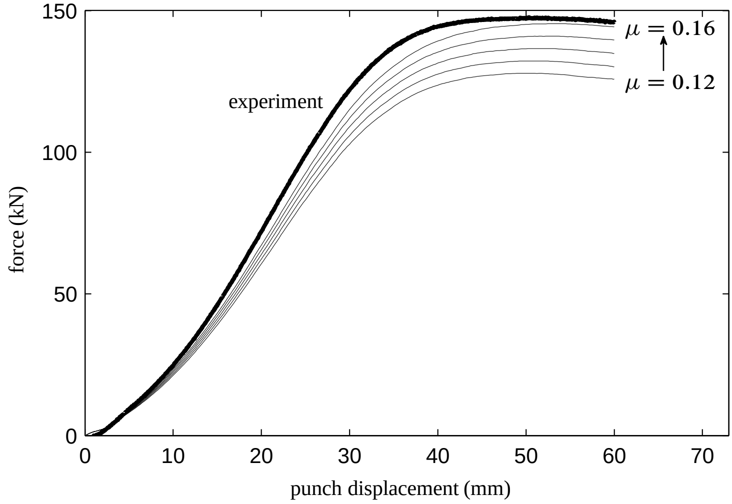

Figure 6.7: Different friction coefficients in the simulation of the cross die.

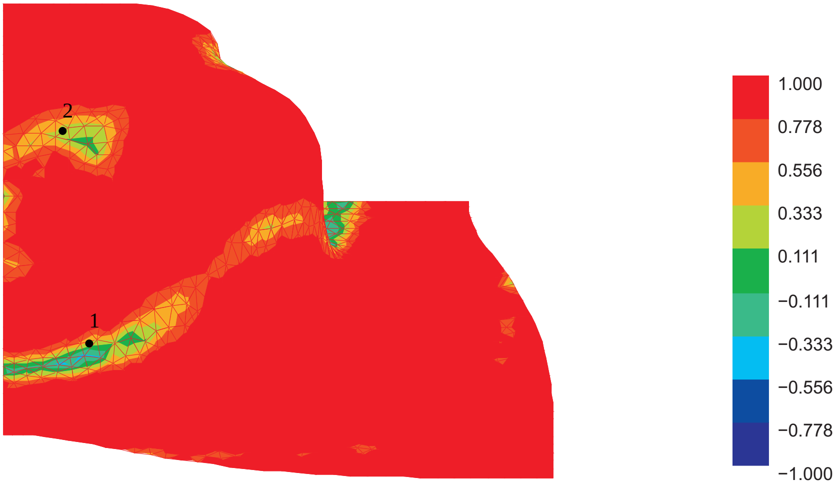

Figure 6.8: The strain path change indicator in the cross die at 55 mm punch displacement.

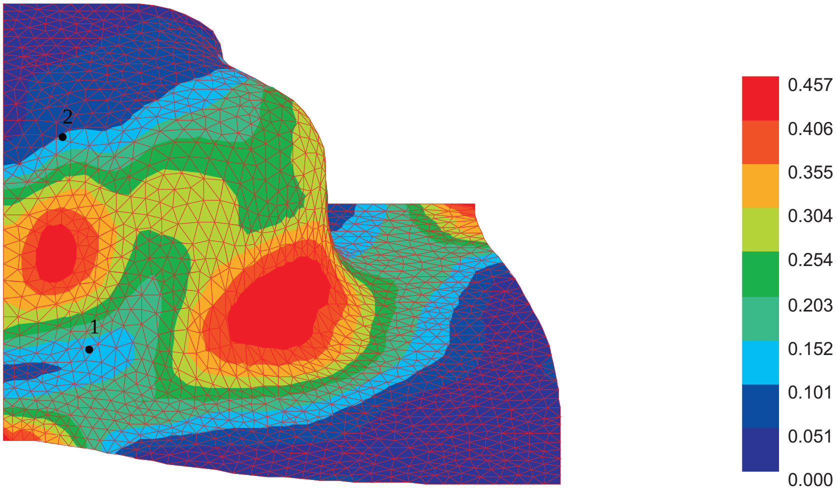

Figure 6.9: The equivalent plastic strain in the cross die at 55 mm punch displacement.

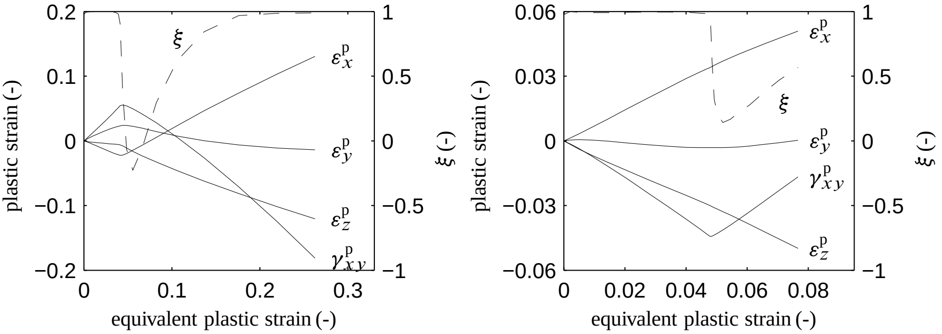

(a) Region (1).

(b) Region (2).

Figure 6.10: The evolution of the plastic strain and the strain path change indicator.

material experiences reversed loading. In Figure 6.9 the distribution of equivalent plastic strain is displayed. It shows that in region (1) where the strain path change occurs, the equivalent plastic strain can reach a value of approximately 50 %. Figure 6.10(a) shows the evolution of the individual strain components for a point in region (1) that has only a limited amount of equivalent plastic strain. The strain path change occurs at $\varepsilon^p_{eq} = 5\,\%$, where all the development of all the in-plane components are reversed, leading to negative value for the strain path change indicator. The value of the strain path indicator shows a minimum at $\xi = -0.2$, which can classified as an orthogonal strain path change.

The strain path change that is indicated at region (2) is not as obvious as the strain path change in region (1). With increasing punch displacement, the material is pulled away from under the die towards the flange. However, this effect is relatively small and the strains that appear are also low. Figure 6.9 shows that the equivalent plastic strain is approximately 10 %. Hence, it may be that the strain path change effects may not appear, because only little strain is accumulated. This is elaborated in Figure 6.10, where the strain components and the strain path change indicator are displayed. The strain history parameters in region (2) (Figure 6.10(b)) show a monotonic development until a strain of 5 % is reached. At that level, only the shear component shows a true change. This causes the excitation of the strain path change indicator to a value of $\xi \approx 0.2$. According to the definition of a strain path change for DC06 in Chapter 5, a strain path dependent material model is required to describe the mechanical behaviour in region (2).

From the investigation of the results of the strain path change indicator it seems that a full strain path dependent material model is required. This is most convincingly indicated by the strain path change indicator in region (1).

6.2.2 Simulations

In this section three simulations are discussed. The process parameters are equal in all the simulations, but three different material models are used: Teodosiu & Hu, Levkovitch and the isotropic/kinematic hardening model. The maximum punch displacement is 60 mm

Table 6.1: The calculation times for the cross die. The simulations with marked (*) material models were terminated.

model	CPU time (h)	stress update (s)	no. of steps	no. of iter.
isotropic	1.4	1.3	600	1
isotropic/kinematic	1.4	1.3	600	1
Levkovitch*	9.5	34	600	3
Teodosiu & Hu*	60.0	37	1688	4

and we aimed for a step size of 0.1 mm displacement per load step. Both the maximum unbalance and the displacement criterion were used to determine convergence in the load step. The relative unbalance force criterion was set to $5 \cdot 10^{-4}$ and the displacement ratio criterion was $2 \cdot 10^{-3}$. The unbalance in the forces is set rather strictly, because it was observed that this stabilises the calculation and reduces the noise in the force–displacement curve.

The combined isotropic/kinematic hardening model performs better than the Levkovitch and the Teodosiu & Hu models when the robustness of the material models is considered. It was observed that the Teodosiu & Hu model is very sensitive to the process parameters. From the nodal unbalance distribution it was observed that region (1) causes problems for the overall convergence of the process. Hence, for the first 20 mm the punch displacement is processed smoothly without step size reduction, because the material is not drawn into the die and no strain path changes occur. After that, the material entering the die cavity experiences a strain path change. To accurately describe the mechanical behaviour in this process, small load steps are required. Additionally, the complex system of equations that are required for the stress update in the Teodosiu & Hu model require small load steps to prevent divergence within the material model. The average step size decreases to a minimum of approximately 0.015 mm with this model. Experiments with different process settings showed that the Teodosiu & Hu model in particular is not robust. The Levkovitch model also requires smaller steps as the material in region (1) enters the die cavity. The stress update of this material model is more robust under strain path changes and larger load steps are used, compared to the simulation with the Teodosiu & Hu model. Still, step size reduction is required for this material model, which reduces the average load step to approximately 0.05 mm.

In Figure 6.11 the resulting force–displacement curves are presented. The robustness of the classical material models is reflected well in this graph. The isotropic and combined isotropic/kinematic hardening models all finish the simulation until the end of the punch displacement. Neither simulations shows any sign of necking. The simulation with the Levkovitch hardening model reaches a punch displacement of 42 mm after which the simulation terminates due to a singular matrix. The Teodosiu & Hu model here reaches a maximum displacement of approximately 42.5 mm, after which the step size becomes too small and the simulation was terminated.

From Figure 6.11 it is recognised that the material model has a significant influence on the force-displacement curve. The results of the simulations with strain path dependent material models (Teodosiu & Hu and Levkovitch) are relatively close together. Furthermore, these models predict that the required force is drastically higher than the prediction of simulations with isotropic and combined isotropic/kinematic hardening models. The prominent difference between the strain path dependent models and the combined isotropic/kinematic hardening models is the description of the mechanical behaviour in an orthogonal strain path change. The Teodosiu & Hu and Levkovitch models predict a sharp increase in stress whilst the combined isotropic/kinematic material model predicts a lower stress compared to the proportional strain path, see Figure 5.8. In Section 6.2.1, the strain path change indicator predicted that strain path effects are present in this process, and hence a full strain path dependent material model is required. This is in agreement with the observations in Figure 6.11. Still, all the material models predict a force–displacement curve that is lower than the actual measurement.

Figure 6.12 shows the distribution of the equivalent plastic strain at 40 mm punch displacement for the 3 different hardening models. This figure indicates that the material models affects the distribution of strain. It shows that the simulation with the combined isotropic/kinematic hardening predicts a strain distribution that is more localised than the 2 strain path dependent material models. The simulation with the Teodosiu & Hu model and the combined isotropic/kinematic hardening model show a similar distribution of equivalent plastic strain. Only between the arms, along the line of symmetry of the simulation, a local area with more equivalent plastic strain is predicted by the combined isotropic/kinematic material model. This is also predicted by the simulation with the distortional hardening model. In contrast with the other two models, the distortional material

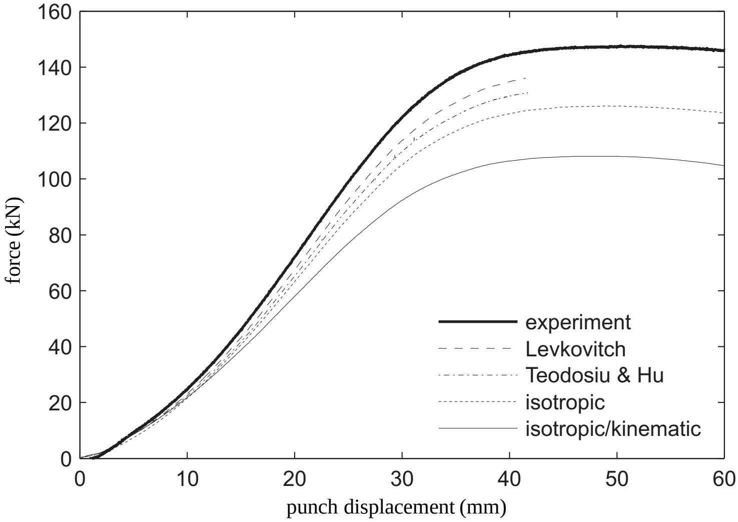

Figure 6.11: Force–displacements curves from the experiment and simulations.

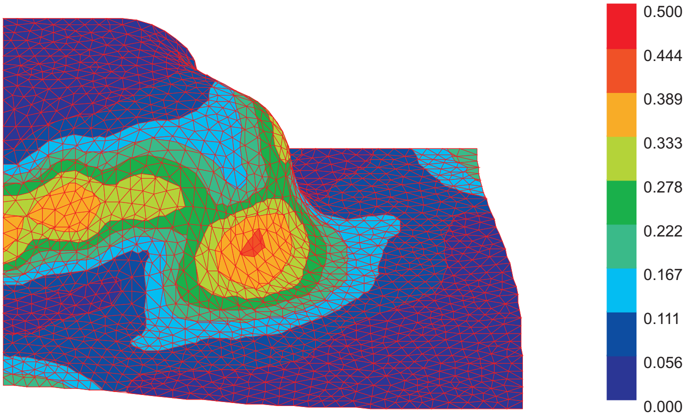

(a) The combined isotropic/kinematic hardening model.

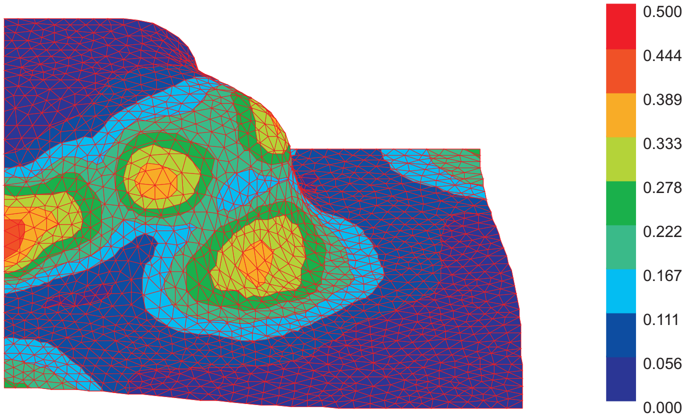

(b) The Levkovitch hardening model.

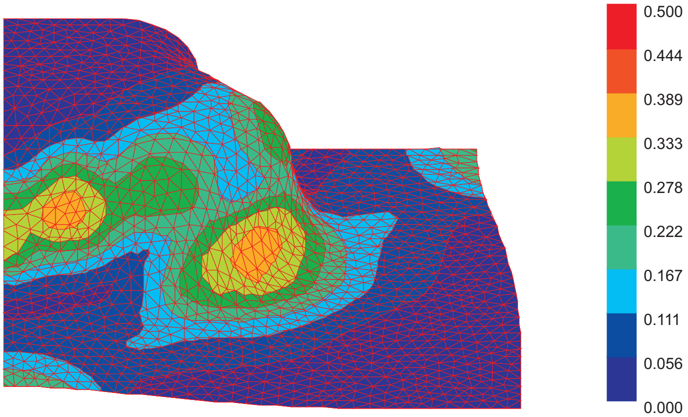

(c) The Teodosiu & Hu hardening model.

Figure 6.12: The distribution of equivalent plastic strain at 40.0 mm punch displacement.

model also predicts more strain on the two corners on the arms of the cross. The simulations with the distortional and Teodosiu & Hu models both have a more uniform spread of the equivalent plastic strain, whereas the combined isotropic/kinematic model predicts more localised strain. This can be explained by the material flow into the die cavity. Material that experiences an orthogonal strain path change when entering the die cavity shows a higher stress in the new loading direction. As a result, the surrounding material is forced to absorb more deformation since the stress level is not as high there.

The required CPU times in these simulations show a great difference, see Table 6.1. It is noticed that these times were recorded for the experiments in Figure 6.11, until the simulation was finished or terminated. Clearly, the 2 simplest models are fast in the processing of the cross die simulation. Both the Levkovitch and the Teodosiu & Hu models require more calculation time for the complete simulation. The Levkovitch model requires this time for the stress update, and for two extra iterations per load step. The Teodosiu & Hu model requires only a little more time for the stress update than the Levkovitch model. The large computation time for the simulation with the Teodosiu & Hu material model stems from the large number of load steps that is required. The Teodosiu & Hu model requires a smaller step size to preserve global convergence of the simulation.

The large difference in processing time between the simulation with the Teodosiu & Hu and Levkovitch model may originate in the way in which the stress evolves during orthogonal hardening. In the Levkovitch model, upon a strain path change, the stress translates across the yield surface to the new stress state. In this process, the yield surface changes slightly due to distortional hardening and the hardening changes the size of the yield surface mildly. Hence, to predict the overshoot in an orthogonal strain path change, there are no large local gradients that can spoil the convergence. For the Teodosiu & Hu model, upon an orthogonal strain path change, a large hardening rate is required to describe the overshoot in the new loading direction. Large load steps will accordingly cause divergence at a global level. Hence, if indeed a larger gradient is present in the orthogonal strain path changes, the Teodosiu & Hu model will require smaller load steps to describe the deformation process.

6.3 Conclusion

In this chapter 2 experiments are used to validate the material models; the experiments with tension under cyclic shear, and the deep drawing of the cross die. The tension under cyclic shear experiment was difficult to evaluate because the input for the validation is an actual strain measurement, that causes considerable noise at the output. For the material that is most sensitive to strain path changes, it was found that the Teodosiu & Hu model represents the trends in the stress evolution best. The Levkovitch and the combined isotropic/kinematic hardening models actually predict opposing stress evolutions.

The deep drawing of the cross die is a representative of a true forming process. The strain path change indicator was used to judge the sensitivity of this process to strain path effects in the material. It was found that this process indeed shows strain path changes that need to be taken into account. The material models are compared on the basis of their predictions of the force–displacement curve. The Levkovitch model gives the best prediction, but the difference with the prediction of the simulation with the Teodosiu & Hu model is small. The simulations with the isotropic and combined isotropic/kinematic hardening models differ considerably from the experimental results. However, the robustness of the strain path dependent models is not satisfactory. Both strain path sensitive models could not finish the simulation completely. This may be due to the settings of the overall simulation, but this does not motivate the use of these models. The required processing times are exceptionally large for the Teodosiu & Hu model, as it is approximately 60 times larger than the simulation with a classical hardening model. The processing time for the Levkovitch model is 6 times as large as the calculation with the classical hardening model. Based on the calculation time and the accuracy in the prediction of the force–displacement curve, the Levkovitch model provides the best solution for simulations of processes with strain path changes.

7. Conclusion

In this thesis the mechanical behaviour of sheet metal subjected to non-proportional strain paths was studied. The research was divided into three different parts; the TWENTE BIAXIAL TESTER and the validation of its results; the experiments to determine the mechanical behaviour of the material; and the material models and their validation. In this chapter, conclusions from the research are drawn and recommendations are given for further research.

Twente biaxial tester

The unique biaxial test equipment is crucial in this research, because the investigation on the mechanical behaviour of sheet metal is carried out solely with this equipment. The functionality of the test equipment was assessed on two points; the accuracy of the measurement and the control of the deformation in the sample.

To judge the accuracy of the stress–strain measurements, two issues were considered: the accuracy of the determination of the stress and strain, and the homogeneity of the deformation area. The strains were calculated with a least squares fit, based on the displacement of dots in the deformation area. It was found that the accuracy of the measured strain was better than 0.05 %. To assess the homogeneity of the strain across the deformation area, digital image correlation software was used to measure the complete strain field in the deformation area. Used in the simple shear test, it showed a homogeneous distribution of strain across the deformation area of the sample. The complete simple shear domain ($\gamma \approx 50\,\%$) of the TWENTE BIAXIAL TESTER can be used to acquire a homogeneous deformation of the sample. In plane strain tension, the tensile strain becomes inhomogeneous after approximately 15% strain. At higher strains, the sample slips away from between the clamps, as a result of the accumulated thickness reduction of the sample. The observed slip depends on the local thickness of the material and the position of the bolts that secure the sample. Eventually this leads to an inhomogeneous deformation. The measured displacements in the plane strain tensile test and the simple shear test were used as boundary conditions for FE simulations. It was demonstrated that the true stress can be calculated by using the measured force and the initial geometry. Compensation factors for boundary effects are not necessary.

The deformation of the sample was applied by prescribing displacements to the actuators. Because of the relative flexibility of the test rig, the actuator position does not accurately control the position of the clamps holding the sample. Especially in experiments with continuous strain path changes, the measured strain path deviates significantly from the intended strain path. In this research, force-feedback was successfully applied to control the strain path.

Material Behaviour

In this work four different materials are examined. All the materials showed to some extent strain path sensitive behaviour. AA5182 and DP600 both show the Bauschinger effect and transient hardening after a load reversal. Additionally, work hardening stagnation appeared after the load reversal. In the experiments with orthogonal strain path changes, neither materials showed the cross-hardening effect.

H340LAD was moderately sensitive to strain path changes. The experiments with load reversals demonstrated that the work hardening stagnation actually turns to softening of the material. A small overshoot was observed in the experiment with the orthogonal strain path change.

DC06 was most sensitive to strain path changes. Especially in the experiment with an orthogonal strain path change, the overshoot in stress in the new loading direction was significant. After the peak, the stress dropped again and converged back to the monotonic hardening curve. The experiments with continuous orthogonal strain path changes showed that, if the strain path change is sufficiently “sharp”, the same overshoot in stress is observed as in the experiment with intermediate unloading. A more gradual transition of the deformation direction shows a gradual approach towards the monotonic hardening curve. In the paper by Wang *et al.* (2008), it was argued that the mechanical behaviour in an orthogonal strain path change is not affected by intermediate elastic unloading, which indeed is proven by the experimental results presented in the current research.

Models

A generic return mapping algorithm in matrix-vector format was described and implemented in the FE-software DIEKA. This model allows for flexibility in using different hardening laws and different yield loci. The model is prepared for the full 3D representation and the plane stress situation.

The Teodosiu & Hu model describes a complex algorithm with 7 evolution equations for the stress update. The material model requires 13 material parameters that need to be determined from experiments with monotonic, cyclic and orthogonal strain paths. The description of the Bauschinger effect, the transient hardening and the work hardening stagnation in a load reversal are accurately described by this model. Continuous orthogonal strain path changes are also predicted well. However, a fit to the experiment with an orthogonal strain path change with intermediate unloading could not be found. The model describes the overshoot in terms of a high hardening rate, whereas in the experiment it seems that the overshoot is the result of a higher flow stress in the new direction. The model proposed by Levkovitch is a more phenomenological material model and combines isotropic, kinematic and distortional hardening models to describe different strain path effects. Distortional hardening is used to describe the effect of an orthogonal strain path change and kinematic hardening describes the mechanical behaviour in reversed loading. These two models are decoupled, which makes the fitting procedure relatively easy. The orthogonal strain path change is captured well, but the simple kinematic hardening model cannot describe the work hardening stagnation and transient hardening effect which are observed in a test with reversed loading. More accurate predictions of the cyclic behaviour should be obtained when using a more advanced kinematic description like Huétink *et al.* (1995); Yoshida and Uemori (2003).

The validation of the material models was done with DC06 on a semi-academical deep drawing process. The presented strain path change indicator showed that, based on a simulation with isotropic hardening, the effects of strain path changes have to be incorporated in the simulation. Indeed, the simulations with the full strain path dependent models give more accurate predictions. The material models were assessed based on their prediction of the force–displacement curve. The Levkovitch model gives a slightly better prediction of the force–displacement curve than the Teodosiu & Hu model, but both are close to the experimental results. The isotropic and combined isotropic/kinematic hardening model under-estimate the required punch force. For accurate modelling of true forming processes, the full strain path dependent models give more accurate results. However, the required calculation times for the strain path dependent models are a large disadvantage. The Levkovitch model requires approximately 6 times more CPU time, whereas the Teodosiu & Hu model requires approximately 60 times more computing time. Because of the simplicity of the model, the flexibility in the different models, and the faster evaluation, it is recommended to continue the development of material models based on the Levkovitch model.

A. Material parameters

In this appendix the parameters for the different materials and material models are presented. The fitting procedure as described in Chapter 5 is used to determine the parameters. The R-values are obtained from Corus.

Table A.1: The R-values for DC06.

parameter	DC06	AA5182	H340LAD	DP600
R_0	1.85	0.6661	0.9093	0.9490
R_{45}	2.06	0.7114	1.0287	0.8404
R_{90}	2.51	0.6011	1.1898	1.1658

Table A.2: The Vegter parameters for DC06.

	0°	45°	90°
f_{sh}	0.572	0.542	0.500
f_{un}	1.000	0.995	0.993
f_{ps}	1.243	1.248	1.246
R-value	1.85	2.06	2.51
f_{bi}	1.153		
f_{bi}	1.153		
α	0.5	0.5	0.5
ρ_{bi}	0.77		

Table A.3: Material parameters for the Swift model.

parameter	DC06	AA5182	H340LAD	DP600
σ_0 (MPa)	70.0	0.0	134.73	131.9
C (MPa)	510.1	562.5	582.8	820.5
ε_0 (-)	$1.0 \cdot 10^{-7}$	0.010874	0.0260	$1.07 \cdot 10^{-4}$
n (-)	0.3826	0.3250	0.2903	0.2087

Table A.4: Material parameters for the combined Swift Armstrong–Frederick model.

parameter	DC06	AA5182	H340LAD	DP600
σ_0 (MPa)	95.0	0.0	0.0	0.0
C (MPa)	300.0	451.8	492.7	732.8
ε_0 (-)	$1.0 \cdot 10^{-9}$	$2.72 \cdot 10^{-3}$	0.322	$6.8 \cdot 10^{-6}$
n (-)	0.340	0.2270	0.2284	0.0995
H_l (-)	12.25	$4 \cdot 10^{4}$	11.4	100
H_k (-)	766.0	0.1	1240	499

Table A.5: Levkovitch material parameters.

parameter	DC06	AA5182	H340LAD	DP600
σ_0 (MPa)	70.0	0.0	0.0	0.0
C (MPa)	349.0	370.0	700.0	592.07
ε_0 (-)	$5.0 \cdot 10^{-5}$	$3.3 \cdot 10^{-5}$	$5.0 \cdot 10^{-9}$	$1.3 \cdot 10^{-6}$
n (-)	0.2969	0.1821	0.1323	0.135
C_α (-)	15.0	57.23	36.53	13.20
α_s (-)	40.0	23.48	82.52	14.99
C_D (-)	15.0	4.30	4.00	4.79
H_D^s (-)	0.0	0.0	0.0	0.0
C_L (-)	11.0	0.54	1.06	1.80
H_L^s (-)	0.65	0.82	0.70	0.85

Table A.6: The Teodosiu material parameters.

parameter	DC06	AA5182	H340LAD	DP600
τ_0 (MPa)	125.0	90.0	150.0	296.0
α_0 (MPa)	0.5	50.0	110.0	80.0
S_s (MPa)	238.8	101.1	213.6	250.0
R_s (-)	65.0	100.0	49.1	114.27
C_p (-)	1.2	24.7	10.0	7.19
C_l (-)	50.0	10.5	50.0	40.4
C_s (-)	5.42	3.30	13.42	10.07
C_α (-)	164.7	235.3	192.5	68.9
C_r (-)	44.4	16.5	140.0	94.8
n_p (-)	350.0	16.6	35.0	2.0
n_l (-)	0.85	1.25	0.50	0.75
m (-)	0.47	0.36	0.55	0.55
r (-)	2.85	2.00	3.0	2.99

Bibliography

An, Y. G., H. Vegter and L. Elliot (2004), A novel and simple method for the measurement of plane strain work hardening, *Journal of Materials Processing Technology*, vol. 155-156, pp. 1616–1622.

Ananthan, V. S., T. Leffers and N. Hansen (1991), Characteristics of second generation microbands in cold-rolled copper, *Scripta Metallurgica et Materialia*, vol. 25, pp. 137–142.

Atzema, E. H., C. H. L. J. ten Horn and H. Vegter (2004), Influence of tooling layout on sheet forming process analysis, in: P. Neittaanmäki, T. Rossi, S. Korotov, E. Oñate, J. Périaux and D. Knörzer (eds.), *European Congress on Computational Methods in Applied Sciences and Engineering*, pp. 1–14, Finland.

Banabic, D., T. Kuwabara, T. Balan and D. S. Comsa (2004), An anisotropic yield criterion for sheet metals, *Journal of Materials Processing Technology*, vol. 157-158, pp. 462–465.

Batoz, J. L. and P. Lardeur (1989), A discrete shear triangular nine d.o.f. element for the analysis of thick to very thin plates, *International Journal for Numerical Methods in Engineering*, vol. 28, pp. 533–560.

Belytschko, T., W. K. Liu and B. Moran (2006), *Nonlinear finite elements for continua and structures*, Wiley, Chichester.

Chaboche (1991), On some modifications of kinematic hardening to improve the description of ratchetting effects., *International Journal of Plasticity*, vol. 7, pp. 661–678.

Chen, W.-F. (1994), *Constitutive Equations for Engineering Materials, Volume 2: Plasticity and Modeling*, Elsevier.

Christodoulou, N., O. T. Woo and S. R. MacEwen (1986), Effect of stress reversals on the work hardening behaviour of polycrystalline copper, *Acta Materialia*, vol. 34, pp. 1553–1562.

Chun, B. K., H. Y. Kim and J. K. Lee (2002), Modelling the Bauschinger effect for sheet metals, part I: theory, *International Journal of Plasticity*, vol. 18, pp. 571–595.

De Borst, R. and P. H. Feenstra (1990), Studies in anisotropic plasticity with reference to the hill criterion, *International Journal for Numerical Methods in Engineering*, vol. 29, pp. 315–336.

De Montleau, P. (2004), Programming of the teodosiu's hardening model, progress report.

Fernandes, J. V., J. J. Gracio, J. H. Schmitt and E. F. Rauch (1993), Development and persistence of microbands in copper deformed under complex strain paths, *Scripta Metallurgica et Materialia*, vol. 28, pp. 1335–1340.

Gardey, B., S. Bouvier, V. Richard and B. Bacroix (2005), Texture and dislocation structures observation in a dual-phase steel under strain-path changes at large deformation, *Materials Science and Engineering A*, vol. 400-401, pp. 136–141.

Goerdeler, M. and G. Gottstein (2001), A microstructural work hardening model based on three internal state variables, *Materials Science and Engineering A*, vol. 309-110, pp. 377–381.

Haddadi, H., S. Bouvier, M. Banu, C. Maier and C. Teodosiu (2006), Towards an accurate description of the anisotropic behaviour of sheet metals under large plastic deformations: Modelling, numerical analysis and identification., *International Journal of Plasticity*, vol. 22, pp. 2226–2271.

Hasegawa, T. and T. Yakou (1975), Deformation behaviour and dislocation structures upon stress reversal in polycrystalline aluminium, *Materials Science and Engineering*, vol. 20, pp. 267–276.

Huétink, J. (1991), Extension of anisotropic hardening elastic-plastic theory to finite strains based on visco-elastic finite strain theory, in: D. Besdo and E. Stein (eds.), *Finite Inelastic Deformations – Theory and Applications*, pp. 197–205, Springer-Verlag, Berlin, Germany.

Huétink, J., A. H. Streppel and P. T. Vreede (1995), Development and experimental verification of constitutive equations for anisotropic sheet metal, in: D. R. J. Owen, E. Oñate and E. Hinton (eds.), *Computational plasticity – Fundamentals and applications*, pp. 2271–2282, Pineridge press, Swansea, U.K.

Johnson, P. E., J. H. Schmitt, S. A. Vincent and J. W. Morris Jr. (1990), The effect of prestrain temperatures on dislocation cell formation and subsequent tensile behavior in low carbon steel sheets., *Scripta Metallurgica et Materialia*, vol. 24, pp. 1447–1452.

Kuhlmann-Wilsdorf, D. (1989), Theory of plastic deformation:–properties of low energy dislocation structures, *Materials Science and Engineering A*, vol. 113, pp. 1–41.

Kuroda, M. and V. Tvergaard (1999), Use of abrupt strain path change for determining subsequent yield surface: Illustrations of basic idea, *Acta Materialia*, vol. 47, pp. 3879–3890.

Kuwabara, T., A. V. Bael and E. Iizuka (2002), Measurement and analysis of yield locus and work hardening characteristics of steel sheets wtih different r-values, *Acta Materialia*, vol. 50, pp. 3717–3729.

Levkovitch, V. and B. Svendsen (2007), Accurate hardening modeling as basis for the realistic simulation of sheet forming processes with complex strain path changes, in: E. Oñate, D. R. J. Owen and B. Suárez (eds.), *Computational Plasticity IX. Fundamentals and Applications*, pp. 608–611, CIMNE, Barcelona, Spain.

Lewandowska, M. (2003), Dependence of the deformation microstructure of aluminium alloys on the strain path, *Materials Chemistry and Physics*, vol. 81, pp. 555–557.

McCabe, R. J., A. Misra and T. E. Mitchell (2004), Experimentally determined content of a geometrically necessary dislocation boundary in copper, *Acta Materialia*, vol. 52, pp. 705–714.

Mughrabi, H. (1983), Dislocation wall and cell structures and long-range internal stresses in deformed crystals., *Acta Materialia*, vol. 31, pp. 1367–1379.

Nes, E. and K. Marthinsen (2002), Modeling the evolution in microstructure and properties during plastic deformation of f.c.c.-metals and alloys – an approach towards a unified model, *Materials Science and Engineering A*, vol. 322, pp. 176–193.

Nesterova, E., B. Bacroix and C. Teodosiu (2001), Experimental observation of microstructure evolution under strain-path changes in low-carbon IF-steel, *Materials Science and Engineering A*, vol. 309-210, pp. 495–499.

Peeters, B., B. Bacroix, C. Teodosiu, P. van Houtte and E. Aernoudt (2001a), Work-hardening/softening of b.c.c polycrystals during changing strain paths: II. tem observations of dislocation sheets in an IF steel during two-stage strain paths and their representation in terms of dislocation densities, *Acta Materialia*, vol. 49, pp. 1621–1632.

Peeters, B., S. Kalidindi, C. Teodosiu, P. van Houtte and E. Aernoudt (2002), Modelling microstructure-based anisotropy in bcc polycrystals during changing strain paths, *Solid State Phenomena*, vol. 87, pp. 163–168.

Peeters, B., M. Seefeldt, C. Teodosiu, S. R. Kalidindi, P. van Houtte and E. Aernoudt (2001b), Work-hardening/softening of b.c.c polycrystals during changing strain paths: I. an integrated model based on substructure and texture evolution, and its prediction of the stress–strain behaviour of an IF stell during two-stage strain paths, *Acta Materialia*, vol. 49, pp. 1607–1619.

Pijlman, H. H. (2001), *Sheet material characterisation by multi-axial experiments*, Ph.D. thesis, University of Twente.

Rauch, E. F. (1997), The stresses and work hardening rates of mild steel with different dislocation patterns, *Materials Science and Engineering A*, vol. 234-236, pp. 653–656.

Rauch, E. F. and J. H. Schmitt (1989), Dislocation substructures in mild steel deformed in simple shear, *Materials Science and Engineering A*, vol. 113, pp. 441–448.

Rauch, E. F. and S. Thuillier (1993), Rheological behaviour of mild steel under monotonic loading conditions and cross-loading., *Materials Science and Engineering A*, vol. 164, pp. 255–259.

Roters, F., D. Raabe and G. Gottstein (2000), Work hardening in heterogeneous alloys—a microstructural approach based on three internal state variables, *Acta Materialia*, vol. 48, pp. 4181–4189.

Schmitt, J. H., E. Aernoudt and B. Baudelet (1985), Yield loci for polycrystalline metals without texture, *Materials Science and Engineering*, vol. 75, pp. 13–20.

Sevillano, J. G., P. van Houtte and E. Aernoudt (1981), Large strains work hardening and textures, *Progress in Materials Science*, vol. 25, pp. 69–412.

Simo, J. C. and T. J. R. Hughes (2000), *Computational inelasticity, Interdisciplinary applied mathematics*, Springer, New York.

Tarigopula, V., O. S. Hopperstad, M. Langseth and A. H. Clausen (2008), Elastic-plastic behaviour of dual-phase, high-strength steel under strain-path changes, *European Journal of Mechanics A/Solids*, vol. 27, p. 764782.

Teodosiu, C. (2005), Some basic aspects of the constituve modelling in sheet metal forming, in: *ESAFORM 2005 Conference, cluj-Napoca, Romania*, pp. 239–244.

Teodosiu, C. and Z. Hu (1995), Evolution of the intergranular microstructure at moderate and large strains: Modelling and computational significance, in: S.-F. Shen and P. R. Dawson (eds.), *Simulation of Materials Processing: Theory, Methods and Applications*, pp. 173–182, Balkema, Rotterdam.

Thuillier, S. and E. F. Rauch (1994), Development of microbands in mild steel during cross loading, *Acta Metallurgica et Materialia*, vol. 42, pp. 1973–1983.

Uenishi, A. and C. Teodosiu (2004), Constitutive modelling of the high strain rate behaviour of interstitial-free steel, *International Journal of Plasticity*, vol. 20, pp. 915–936.

Uenishi, A., C. Teodosiu and E. V. Nesterova (2005), Dislocation-based intragranular hardening model taking into account strain path and strain rate changes for steels, in: *ESAFORM 2005 Conference, Cluj-Napoca, Romania*, pp. 213–216.

van Liempt, P. (1994), Workhardening and substructural geometry of metals, *Journal of Materials Processing Technology*, vol. 45, pp. 459–464.

van Riel, M. and A. van den Boogaard (2007), Stress–strain responses for continuous orthogonal strain path changes with increasing sharpness, *Scripta Materialia*, vol. 57, pp. 381–384.

van Riel, M. and A. H. van den Boogaard (2007), Consistent plane stress–3d conversion of hardening models and yield criteria, in: E. Oñate, D. R. J. Owen and B. Suárez (eds.), *Computational Plasticity IX. Fundamentals and Applications*, pp. 624–627, CIMNE, Barcelona, Spain.

Vegter, H., C. H. J. L. ten Horn and M. Abspoel (2009), The corus–vegter lite material model: simplifying advanced material modelling, in: *12th ESAFORM conference*, to be published.

Vegter, H. and A. H. van den Boogaard (2006), A plane stress yield function for anisotropic material by interpolation of biaxial stress states., *International Journal of Plasticity*, vol. 22, pp. 557–580.

Viatkina, E. (2005), *Micromechanical modelling of strain path dependency in FCC metals*, Ph.D. thesis, Eindhoven university of Technology.

Wang, J., V. Levkovitch, F. Reusch, B. Svendsen, J. Huétink and M. van Riel (2008), On the modeling of hardening in metals during non-proportional loading, *International Journal of Plasticity*, vol. 24, pp. 1039–1070.

Yoshida, F. and T. Uemori (2002), A model of large-strain cyclic plasticity describing the Bauschinger effect and workhardening stagnation, *International Journal of Plasticity*, vol. 18, pp. 661–686.

Yoshida, F. and T. Uemori (2003), A model of large-strain cyclic plasticity and its application to springback simulation, *International Journal of Mechanical Sciences*, vol. 45, pp. 1687–1702.

Zienkiewicz, O. C. and R. L. Taylor (2005), *The Finite Element Method. For solid and structural mechanics*, Butterworth–Heinemann, 6 edn.